Bulletin of Materials Science

Volume 21 Number 1 February 1998

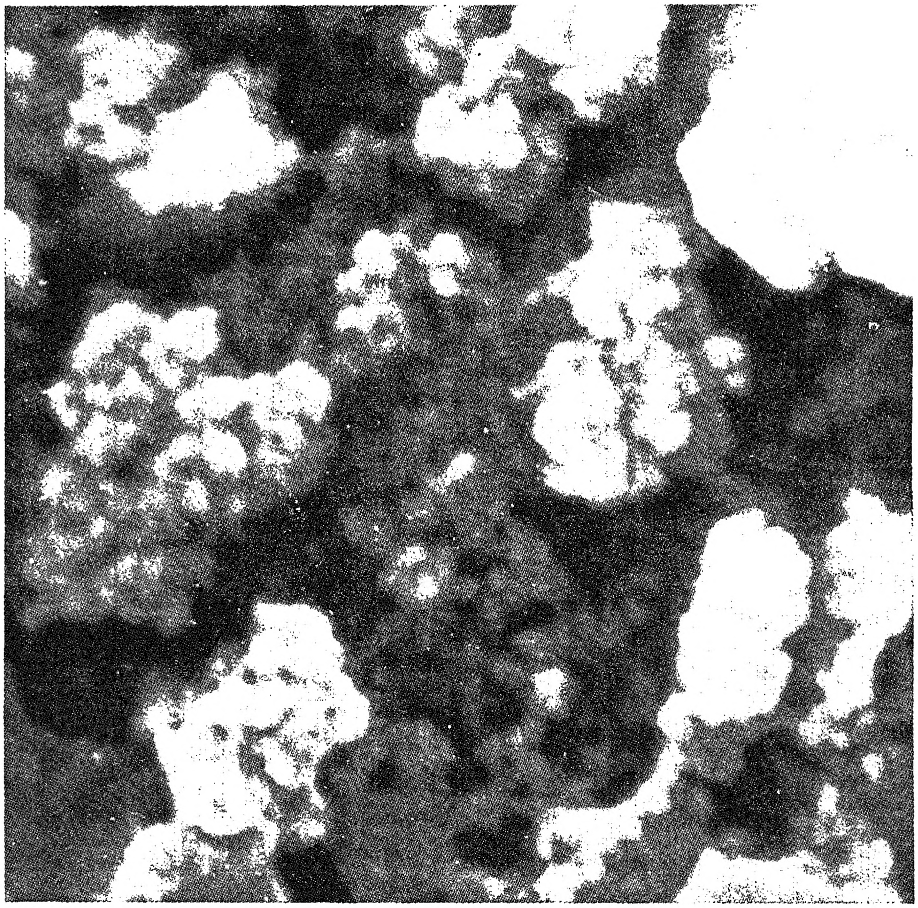

Published by
INDIAN ACADEMY OF SCIENCES
in collaboration with
MATERIALS RESEARCH SOCIETY OF INDIA and
INDIAN NATIONAL SCIENCE ACADEMY

International Advisory Editorial Board

Bulletin of Materials Science

Vol. 21, No. 1, February 1998

CONTENTS

SEM photograph of powders of ZrO_2 showing agglomeration of particles. For details, see p. 84.

d in
– CURRENT CONTENTS

torial

's may notice that there is a change in the format issue of **Bulletin of Materials Science**. Sometime 1997, the Editor of Publications of the journals ademy suggested that we consider adoption of a nt dimension of the journal and format of the The suggested format is easily adaptable for fully terized processing of the journal. The contributors e easily persuaded to send their manuscripts on es. The suggestions were considered in detail at ting of the Editorial Committee which was held November 1997 at IICT, Hyderabad. Upon the mendations of the Editorial Committee, the **Bulletin terials Science** will hereafter be printed in a two n format and would continue to retain the present of the cover page. The journal itself will however ghtly bigger. This will also enable an increase in inted matter for the same number of pages. I am ne changes will be welcomed by readers of the **in of Materials Science**.

el it opportune to remind the readers about pub- n options available with the journal. BMS publishes **Communications**. This will enable publishing your research results of importance within two of communication. These papers are given very refereeing. BMS publishes **Review Articles**—both and contributed. These reviews have to be on subjects. **Book Reviews** are also published. Auth encouraged to send copies of their published bo reviewing. We are striving hard to reduce th between the receipt of paper and its final public a minimum. The delays are often attributable to r revisions which some papers require. In this co express my sincerest thanks to the referees wh spared their most valuable time for the bettern the journal.

The journal also publishes Proceedings of National and International Meetings on Materials S Although we receive a number of requests in thi every year, we have to be selective in view of the ting costs of journal production. However, the promises to accommodate as many such requests as p

I trust that the community of materials scienti continue to offer their best cooperation in mai good standards of the journal.

E

later. Sci., Vol. 21, No. 1, February 1998, pp. 1–70. © Printed in India.

hniques and applications of electron spin resonance*

C S SUNANDANA
School of Physics, University of Hyderabad, Hyderabad 500 046, India

MS received 27 January 1996

Abstract. A broad-spectrum review of the applications of electron spin resonance to advanced mat presented. Starting with basic concepts the reader is taken through a quick tour of techniques in continuous-wave and pulse ESR, microscopy and imaging, as well as a few emerging techniques. Appl of spin identification, spin counting, spin mapping and spin imaging of a variety of advanced sol materials including metals and alloys, semiconductors, inorganics, electroceramics, catalysts, inte polymers, glasses, and organic charge-transfer complexes besides superionic conductors and high-temp superconductors are included. It is thus demonstrated that the technique is at once specific, sens composition, phase and texture yet accurate enough to be a quantitative but non-invasive tool that p to be useful in the study of newer and newer materials including multilayers, ferrofluids and nanom

Keywords. Electron spin resonance; advanced materials; ESR microscopy and imaging; semicon polymers; glasses; superionic; superconductors.

eamble

e of magnetic moment of an unpaired electron — amental particle with an intrinsic property of 'spin' 1) that is naturally found (or artificially created) erials as an essential part of their unique crystal res, and dictating their electrical, optical and mag- ehaviour — as a microscopic, resonance spectroscopic of characterization is the basis of electron spin nce (ESR) or more generally speaking electron para- ic resonance (EPR). It is the hierarchy of interactions magnetic moment with its neighbouring and the listant material environment that is exploited in this ue to learn more about either the materials processing or the induced process(es) that take place within terial. It could be said that the EPR technique and ed materials are 'made for each other'.

ing with a brief historical perspective, this article n to provide a brief account of the methods and tions of this technique. The spectrum of the ed materials covered include semiconducting ls, polymer materials, ceramics and glasses, and

2. A brief historical perspective

Electron spin resonance (ESR) or more generally s electron paramagnetic resonance (EPR), discove Zavoiskii (1944) in $MnSO_4$ employing a 47 magnetic field and a 133 MHz rf magnetic field extension of the original Stern–Gerlach experimen 1921; Gerlach and Stern 1924), on atomic beams demonstrated the space quantization of atomic m moments. In between, Rabi (1939a, b) had pe the 'nuclear Zeeman effect' experiment by using frequency electromagnetic field perpendicular homogeneous dc magnetic field. Theoreticall possibility of quantum transitions between m sublevels of atoms under the influence of an e magnetic field was suggested by Einstein and Eh (1922).

The earliest applications of microwave re spectroscopic technique were on (i) $CuSO_4{\cdot}5H_2O$ in which 'exchange narrowing' was discovered (B and Griffiths 1950), (ii) F-centres in alkali halide which structural information was obtained (Ki

Table 1. Properties of fundamental particles relevant for magnetic resonance spectroscopy.

Property	Electron	Proton	Neutron	
Charge (C)	$-1{\cdot}602192\times10^{-19}$		0	
Mass (kg)	$9{\cdot}109534(47)\times10^{-31}$	$1{\cdot}6726485(86)\times10^{-27}$	$1{\cdot}6749543(86)\times10^{-27}$	1
Magnetic moment (Joule/Tesla)	$9{\cdot}284832(36)\times10^{-24}$	$1{\cdot}401671(51)\times10^{-27}$		
		$2{\cdot}7923456(11)\mu_N$	$-1{\cdot}91304184(88)\mu_N$	4
		$\mu_N = 5{\cdot}0505\times10^{-27}$ J/T		
g-factor (Zeeman)	$2{\cdot}00231929$			1
g-factor (spin–orbit)	$2{\cdot}00463858$			

Sources:
1. Weast R C (ed.) 1988 *CRC Handbook of Physics and Chemistry* 1st Student edn.
2. Krane K S 1988 *Introduction to Nuclear Physics* (New York: Wiley).

An investigation of permeability of ferromagnetic metals Fe, Co and Ni, by Griffiths (1946) led to the discovery of ferromagnetic resonance. An examination of free radicals in leaves, seeds and tissue preparation saw the first biological application (Commoner *et al* 1954). McConnell pioneered the use of 'spin labels' or free radical substituents in biological systems (Stone *et al* 1965), while Sands (1955) pioneered a continuing structural investigation on transition metal ion-doped glasses. Weeks (1956) applied the technique for studying radiation-induced centres in crystalline quartz, and, Yasaitis and Smaller (1953) investigated the paramagnetic centres in irradiated borate glasses. The studies on mechanically produced free radicals in polymers were pioneered by Zakrevskii *et al* (1968).

The observation of electron spin echoes (Gordon and Bowers 1958; Mims *et al* 1961) ushered in the era of pulsed electron spin resonance, coming in the wake of Hahn's discovery of nuclear spin echoes (Hahn 1950). The last decade has seen the emergence of EPR imaging and microscopy (Ikeya 1991), again following the discovery of NMR imaging (Lauterbur 1973).

The bludgeoning activity in this field is evidenced by the very recent appearance of a number of comprehensive monographs and workshop proceedings (Pilbrow 1990; Yordanov 1991; Mabbs and Collison 1992; Ikeya 1993), besides the existing classics (Wertz and Bolton 1972; Atherton 1973; Abragam and Bleaney 1989).

motion of these moments and an
thereof; (iii) quantization of these
and I for electron and nuclei, resp
magnetic energy levels created by
static magnetic field and a separ
levels; (v) a substantial number of '
energy states at ambient temper
Boltzmann distribution law, accordin
lation difference between two energy
T is proportional to the negative ex
the difference between concerned ene
energy $k_B T$, where k_B is the Bolt
finally, (vi) the natural precession
Larmor frequency for the spin sy
electronic moment depends on th
field and for the nuclear moment on t
field) which may be approached ei
frequency of the alternating field at a
field or by scanning the static mag
frequency.

3.1 *Classical picture*

A planetary model of an atom with
($\mu_I \neq 0$) and an unpaired electron (μ
intrinsic property of 'spin' in a clas
An electron of spin S with a m
experiences — much like a tiny ba
$\mu \times H_0$ in an external magnetic field.

γ_e = electron magnetogyric ratio $= -ge/2mc$, with g the spectroscopic splitting factor, e the electron, m the electron mass (see table 2) and c the y of light. For the electron, the dipole moment s the angular momentum so that

$$= -\gamma \hbar S. \quad (3)$$

agnetic component of the electromagnetic field lies in microwave region for ESR and radio- ncy region for nuclear magnetic resonance or $|H_1| (\ll H_0)$ also rotates with microwave frequency exerts a torque $\mu \times H_1$ on μ. As long as $\omega \neq \omega_0$ rque is zero on the average but when $\omega = \omega_0$, μ ses around H_1 with a frequency $\omega_1 = \gamma_e H_1$ besides sual precession around H_0 with frequency $_1$). Consequently, μ slowly changes its direction g down and eventually reaching a position opposite original orientation (figure 2). In the flipping s work is done on the dipole moment by the vave magnetic field. In other words, the system s energy from the microwave field H_1 during nce. At resonance the oscillatory magnetic moment, to H, produced by Larmor precession interacts e small oscillatory magnetic field $H_1 \cos \omega t$, also to H, and changes the direction of component long H by 180°, and thus changes the energy of ctronic dipole, causing ESR absorption. Thus at nce,

$$= \nu_0 = g(e/2m)\, H\ (2\pi)$$

$$= 139{\cdot}96(gH)\ (\nu \text{ in Hz, } H \text{ in T}). \quad (4)$$

lso expressed in Oersted and gauss, with 10,000 nits to a Tesla.

uantum picture

m mechanically, the phenomenon of electron gnetic resonance is described as the magnetic transitions brought about by the interaction of the tic field of the microwave radiation with a magnetic t in the absorbing system. Quantum mechanics helps ing at the probability of these transitions and shows his probability has a sharp maximum when

when the total magnetic field acting on the spin is the vector sum

$$\mathbf{H} = H_1(i \cos \omega t + j \sin \omega t) + H_0 k,$$

and g_e is assumed to be 2. The resonance conditi be arrived by considering the allowed energies electron magnetic dipole

$$\mu[\,|\mu| = \gamma \hbar\, S(S+1)^{1/2}],$$

in the field H_0, using the energy operator

$$\mathcal{H} = -\mu \cdot H_0 = \gamma \hbar S \cdot H_0\,.$$

Taking H_0 along $+z$ axis (figure 2) the allowed e are

$$E_{M_s} = \gamma \hbar H_0 M_s,$$

where the quantum number M_s specifies the values of the z-components of S viz. $-S$, $\ldots S-1$, S. For $S = 1/2$, $M_s = \pm 1/2$ and the energies are

$$E \pm \frac{1}{2} = \pm \gamma_e \hbar H_0.$$

Transitions between these levels (figure 3) cau magnetic dipole radiation require that $\Delta M_s = \pm$ resonance condition that the energy quantum $\hbar\omega$ must satisfy is

$$\hbar\omega = E \pm \frac{1}{2} - E - \frac{1}{2} = \gamma_e \hbar H_0\,,$$

which coincides with the classical picture $\omega = \gamma$ The basic gyromagnetic ratio for the free electro

$$\gamma_e = 2\pi(28{\cdot}0246\ \text{GHz}/T).$$

3.3 *Spin relaxation*

The above pictures are valid for the hypothetic of a single isolated spin or a paramagnet. In t world materials contain a large number of spins, the concept of a 'reservoir' or a 'bath' or the of a 'thermal equilibrium' comes into the pictu

netic nuclei and hyperfine coupling constants from electron spin resonance studies.

in	Nuclear dipole magnetic moment (μ_N)	$\lvert \psi_{na}(o) \rvert^2$ (a.u.)	$\langle r^{-3} \rangle$ (a.u.)	Isotropic coupling A_{iso} (G)	Anisotropic coupling (B_0)	g_N	Electric quadrupole moment ($\lvert e \rvert \times 10^{-24}$ cm^{-2})	Most stable paramagnetic form (S)	λ (cm^{-1})
2	+ 2·79284	0·314 (0·318)$		508 (1430)$		5·586912	–	H^-	
	+ 0·85743			78		0·8574376	0·002875		
2	– 2·12762	(1·867)		(– 6357)		– 4·255248			
	+ 0·822056			39		0·8220514	– 0·000644		
2	+ 3·25644	0·1673 (0·2101)		105 (364·9)		2Ã170961	– 0·040	Li^0	0·2
2	– 1·1776	0·5704 (0·7188)		130 (– 451·6)		– 0·7850	0·053		1
	+ 1·8007	1·408	0·775	242		0Ã600216	0·08608		
2	+ 2·6886	(1·775)	(0·9293)$	725 (2547)	t8	1·792424	0·040		11
2	+ 0·70241	2·767 (3·358)	1·692 (2·002)	1130 (3777)	66				29
	+ 0·40376	4·770 (5·599)	3·101 (3·599)	552 (1811)	34	2·0382	0·01932		76
2	– 0·28319			775	48	0·4037607			
2	– 1·89379	7·638 (8·669)	4·974 (5·820)	1660 (– 5263)	104	– 0·757516	– 0·026		151
	+ 2·62887	11·966 (12·53)	7·546 (8·766)	17200 (52870)	1·084	5·257934			270
/2	+ 2·21752	(0·7797)		317 (927·1)		1·478391	0·108	Na^0	11
/2	– 0·85545	(1·763)		(– 485·9)		– 0·34218	0·22		20
/2	+ 3·64150	2·358 (3·327)	1·055 (1·493)	985 (3911)	42	1·456601	0·150		75
/2	– 0·5553	3·807 (5·115)	2·041 (2·691)	1220 (– 4594)	62	– 1·1106			149

Nuclear dipole magnetic moment (μ_N)	$\lvert \psi_{na}(o) \rvert^2$ (a.u.)	$\langle r^{-3} \rangle$ (a.u.)	Isotropic coupling A_{iso} (G)	Anisotropic coupling (B_0)	g_N	Electric quadrupole moment ($\lvert e \rvert \times 10^{-24}$ cm^{-2})	Most stable paramagnetic form (S)	λ (cm^{-1})
+ 0·68412			1395	84	2·3006	− 0·06493		
+ 0·39146			83		0·2609909	0·054		38
	(1·066)		(228·5)					
− 1·298						− 0·067		
+ 0·21487			45		0·1432542	0·060		
− 1·3173					− 0·376414	< 0·23		
	(2·063)		(− 640·7)					
+ 4·756					1·35906	− 0·22		
	(2·506)	(1·851)	(2823)					
− 0·7885					− 0·31539	0·29	Ti^{3+}	154
	(2·975)	(2·444)	(− 7820)					
− 0·10417					− 0·315477	0·24		
+ 3·34745					0·556593	0·209		
+ 5·1514					1·46836	− 0·0515	V^{4+}, V^{3+}	104
	(3·378)	(3·114)	(4165)				V^{2+}	55
− 0·47454					− 0·3147	− 0·0285/	Cr^{2+}	57
	(2·811)	(3·414)	(− 748·2)			+ 0·022	Cr^{3+}	87
+ 3·4687					1·3819	0·33	Mn^{2+}	–
	(4·300)	(4·721)	(5036)				Mn^{3+}	85
+ 0·09044					0·1816		Fe^{3+}	
	(4·832)	(5·659)	(747·20)				Fe^{2+}	− 100
+ 4·627					1·318	0·42	Co^{2+}	− 180
	(5·233)	(6·710)	(5947)					
− 0·75002					− 0·50001	0·162	Ni^{2+}	− 335
	(5·755)	(7·864)	(− 2499)				Ni^{3+}	
+ 2·2233					1·484	− 0·222	Cu^{2+}	− 852
	(4·617)	(8·455)	(5995)					
+ 2·3817					1·588	− 0·195		
+ 0·8755	4·5222		376		0·350312	0·150		386
	(6·379)	(10·52)	(2087)					
+ 2·01659	6·9493	2·8665	2675		1·34439	0·168		551
	(10·18)	(3·973)	(12210)					
+ 2·56227			3400		1·70818	0·168		

Nuclear dipole magnetic moment (μ_N)	$\lvert \psi_{na}(o) \rvert^2$ (a.u.)	$\langle r^{-3} \rangle$ (a.u.)	Isotropic coupling A_{iso} (G)	Anisotropic coupling (B_0)	g_N	Electric quadrupole moment ($\lvert e \rvert \times 10^{-24}$ cm^{-2})	Most stable paramagnetic form (S)	λ (cm^{-1})
+ 1·43947	12·5606	6·9871	3430		0·959647	0·29		1550
	(16·75)	(9·102)	(14660)					
0·53506	15·7791	9·2284	4840		1·0693			1688
	(20·41)	(12·05)	(20120)					
+ 2·1064	19·4127	11·8758	7810		1·404266	0·293		2460
	(24·47)	(15·25)	(32070)					
2·2706			8400		1·513706	0·27		
− 0·9767					− 0·215704	0·26		
	(29·12)	(18·76)	(− 5937)					
+ 1·35302					0·541253	0·273		
	(2·000)		(1037)					
+ 2·7512					1·83427	0·130		
− 1·693					− 0·24291	0·15		
	(3·617)		(− 853·6)					
− 0·1373					− 0·274836			
	(4·616)	(2·373)	(− 1250)					
− 1·3036					− 0·521448			
	(5·283)	(3·126)	(− 2753)					
+ 6·1705					1·3712	− 0·28		
	(4·736)	(3·494)	(6590)					
− 0·9133					− 0·3656	− 0·019		
	(5·264)	(4·318)	(− 1984)					
− 0·9335					− 0·3734	0·2		
− 0·6413					− 0·279	0·076		
− 0·7188					− 0·279	0·44		
	(6·085)	(6·145)	(− 1764)					
− 0·0884					− 0·1768	–		
	(6·414)	(7·179)	(− 1229)					

Nuclear dipole magnetic moment (μ_N)	$\lvert \psi_{na}(o) \rvert^2$ (a.u.)	$\langle r^{-3} \rangle$ (a.u.)	Isotropic coupling A_{iso} (G)	Anisotropic coupling (B_0)	g_N	quadrupole moment ($\lvert e \rvert \times 10^{-24}$ cm^{-2})	paramagnetic form (S)	λ (cm^{-1})
− 0·6217					+ 1·2454			
+ 5·523					1·22864	0·846		
− 0·918					− 1·8377			
− 1·000					− 2·00208			
− 1·046					− 2·09456			
	(17·46)	(9·160)	(− 43920)					
+ 3·359					1·3455	− 0·33		
	(21·51)	(12·25)	(351000)					
+ 2·547					0·72876	− 0·68		
− 0·7359					− 1·4736			
− 0·8871					− 1·7766	–		
	(25·29)	(15·47)	(− 55590)					
+ 2·808					1·12530	− 0·789		
	(29·27)	(18·92)	(41600)					
− 0·7768					− 1·55595	–		
	(33·79)	(22·57)	(− 67790)					
?					0·461240	− 0·120		
+ 2·579					0·7378477	− 0·003		
	(2·538)		(2467)					
+ 0·8365					0·55884	0·20		
+ 0·9357					0·62515	0·34		
	(4·722)		(3971)					
2·778					0·79520	6·22		
	(5·492)	(3·127)	(6007)					
+ 3·707					0·74238	0·51		
	(4·950)	(4·953)	–					
4·25				− 11·87375	1·6	− 0·041		800
	(5·208)	(5·565)	(12490)					
− 1·08					− 0·3076	− 0·56		900
	(5·309)	(6·201)	(− 2399)					
− 0·66				+ 64·60	− 0·190	− 0·29		
− 0·813				− 58·7543	− 0·2322	− 0·18		1200

Nuclear dipole magnetic moment (μ_N)	$\lvert \psi_{na}(o) \rvert^2$ (a.u.)	$\langle r^{-3} \rangle$ (a.u.)	Isotropic coupling A_{iso} (G)	Anisotropic coupling (B_0)	g_N	Electric quadrupole moment ($\lvert e \rvert \times 10^{-24}$ cm^{-2})	Most stable paramagnetic form (S)	λ (cm^{-1})
+ 3·464					1·389	1·53		1416
+ 1·530				0·6134	3·92			
	(5·952)	(8·261)	(5722)					
− 0·27					− 0·1723	1·30		1540
	(6·970)	(3·993)	(− 2546)					
− 0·36					− 0·2253	1·34		
	(6·971)	(3·993)	(− 2546)					
+ 1·95					1·342	1·34		− 1770
	(6·142)	(9·783)	(13630)					
− 0·48						− 0·189	2·47	− 1860
	(− 0·71415)							
+ 0·673					0·266	2·51		
	(6·459)	(10·59)	(2963) (6)					
+ 4·173					1·192	2·73		− 2000
	(6·624)	(11·43)	(13560)					
− 0·5665					− 0·1618	2·827		− 2350
	(3·739)	(12·31)	(− 1934)					
− 0·2316								
	(6·919)	(13·26)	–					
+ 0·4919					0·9885			− 2940
	(− 3·6302) (4)	(13·26)	(− 5835)					
− 0·6776					− 0·27185	2·8		
	(7·245)	(14·19)	(− 3670)					
+ 2·2327					0·63943	5·68		
	(8·700)	(4·588)	(10630)					
+ 3·19					0·454	8·0		
+ 0·7935					0·2267	4·5		
	(9·942)	(5·756)	(4410)					
− 0·6409					− 0·1424	5·1		

Nuclear dipole magnetic moment (μ_N)	$\lvert\psi_{na}(o)\rvert^2$ (a.u.)	$\langle r^{-3}\rangle$ (a.u.)	Isotropic coupling A_{iso} (G)	Anisotropic coupling (B_0)	g_N	Electric quadrupole moment ($\lvert e\rvert \times 10^{-24}$ cm^{-2})	Most stable paramagnetic form (S)	λ (cm^{-1})
+ 3·2197					1·2878	2·22		
	(13·09)	(9·454)	(35490)					
+ 0·0646					0·1311			
0·6599					0·488	0·8		
	(13·90)	(10·79)	(13200)					
+ 0·1461					0·097	0·78		
+ 0·1591					0·107	0·70		
	(14·87)	(12·19)	(3493)					
+ 0·6095					1·2190			
	(12·53)	(12·81)	(34410)					
+ 0·1457					0·097968	0·594		
	(12·86)	(14·31)	(2876)					
+ 0·5059					1·011770			
	(17·37)	(16·78)	(41880)					
− 0·5602					− 0·373483	0·42		
+ 1·6222					3·244514			
+ 1·6382					3·2754			
	(22·97)	(10·13)	(183800)					
+ 0·5926					1·1748			
	(27·96)	(14·72)	(81510)					
+ 4·110					0·938	− 0·46		
	(33·09)	(19·15)	(77530)					
− 0·35					− 0·10	4·3		

) 1988 *CRC handbook of physics and chemistry*, 1st student edn
P W and Symons M C R 1967 *The structure of inorganic radicals* (Amsterdam: Elsevier)
ıc (1993)
ıic parameters from Hermann-Skillman wavefunction. Weltner Jr W 1983 *Magnetic atoms and molecules* (New York: Dover)

Equation (11) ensures that there is always an excess spin population in the ground state ready to undergo transitions. More significantly, since the $N^- > N^+$ energy absorption would occur until $N^- = N^+$, when the spin system would become saturated and no resonance would be detectable. In fact, there are two mechanisms acting within the material by which energy is effectively transferred by the spin system to the surroundings. The spin–lattice relaxation, characterized by time T_1 and exponential in time, results from interactions of the electronic magnetic moments with each other and with the other electrons of the host material, or the 'lattice'. This 'longitudinal' relaxation causes changes in the component of μ parallel to H_0. A short T_1 affects the linewidth of the resonance through the energy–time uncertainty relation $\Delta E\ \Delta\tau \geq \hbar$, ΔE being the uncertainty of an energy level and $\Delta\tau$ being the lifetime of that state, i.e. T_1. A very short T_1 would thus imply a large ΔE and a broadened ESR line at ambient. ESR lines can be broadened by magnetic interaction among the spins themselves, as a result of which the different spins would experience slightly different local fields in the z-axis, leading to a spread in the Larmor precession frequencies. Eventually the spins would not precess in phase at all, and there would be a gradual dephasing, exponential in time, the process being characterized by a transverse or a spin–spin relaxation time T_2. Spin–spin relaxation processes are adiabatic because there is no exchange of energy between the spin system and the reservoir.

Thus the spin relaxation mechanisms are crucial to the observation of electron spin resonance spectra. Aspects of lineshape and linewidth are considered in § 6.

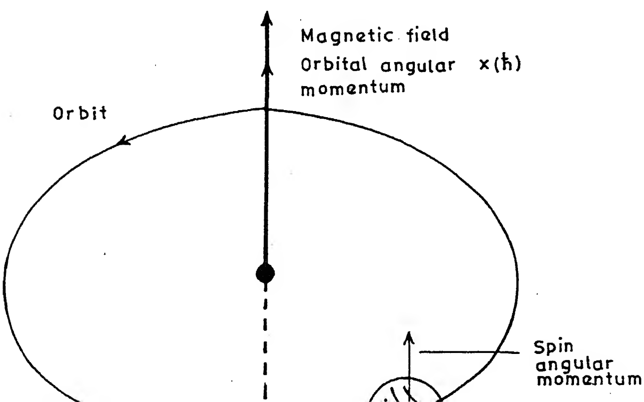

4. ESR and allied phenomena

4.1 *Electron spin resonance*

When a material containing electro placed in a static magnetic fiel electromagnetic radiation, absorp magnetic dipole transitions occu characteristic frequencies in the mic electromagnetic spectrum.

For a system with electron spi silicon ($S = 1/2$)) there are $2S + 1$ static magnetic field H given by:

$$E = \langle \psi_i \mid \hat{\mathcal{H}} \mid \psi_i \rangle = M_s\, g\, \mu_B H,$$

where ψ_i is a characteristic wave

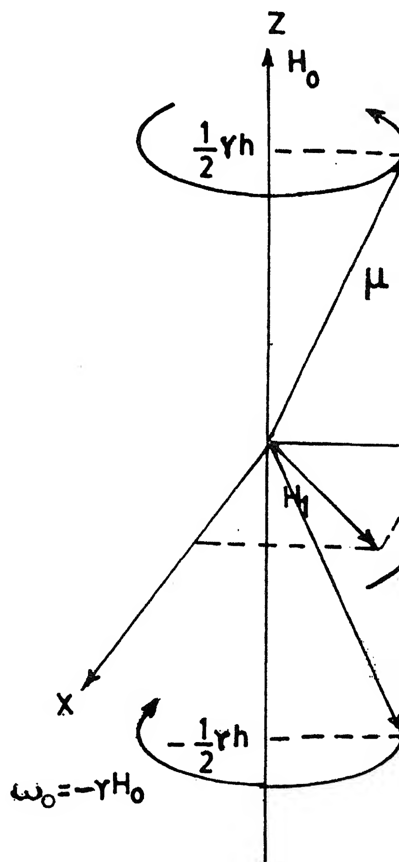

component of the spin angular momentum $S_z\hbar$, and $\hat{\mathcal{H}}$ is the spin Hamiltonian operator

$$\hat{\mathcal{H}} = g\mu_B H\hat{S}_z\,, \tag{13}$$

μ_B or the Bohr magneton is a unit for the magnetic moment of the electron $\mu_e = 1/2\, g_e \mu_B = 9{\cdot}28485 \times 10^{-21}$ JT^{-1} and the free electron g-value is 2·00232. The magnetic dipole transitions between the Zeeman levels (so-called because the dc magnetic field separates the levels as in Zeeman effect observed in atomic spectra) are induced by the magnetic component of the microwave electromagnetic field, when the energy of the microwave photon matches the energy level separation

$$\Delta E = h\nu = \Delta M_s g\mu_B H_r, \tag{14}$$

where $\Delta M_s = \pm 1$ is the selection rule for ESR (figure 4). Equation (14) implies a reorientation of the electron magnetic moment, or a flipping which is possible only when the electromagnetic field is polarized such that the oscillating magnetic field has a component perpendicular to the static magnetic field.

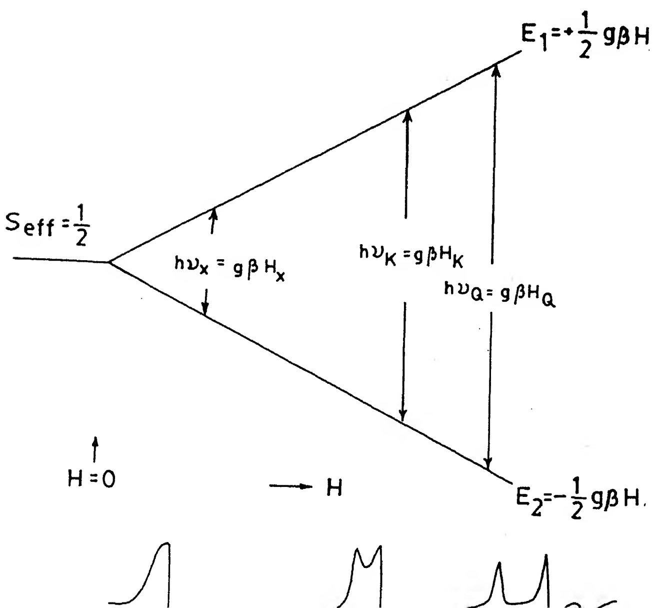

The g-factor of (13) is in general a

$$\hat{\mathcal{H}} = \mu_B \hat{S}\cdot\tilde{g}\cdot\hat{H},$$

$$\text{or } \hat{\mathcal{H}} = \mu_B (S_x S_y S_z) \begin{bmatrix} g_{xx} & g_{xy} & g_{xz} \\ g_{yx} & g_{yy} & g_{zy} \\ g_{zx} & g_{zy} & g_{zz} \end{bmatrix} \begin{bmatrix} H_x \\ H_y \\ H_z \end{bmatrix}$$

where S_x, S_y, S_z and H_x, H_y and H_z ar of $\hat{S}$ and $\hat{H}$, measured with respect to x, y, z of mutually orthogonal axes in th materials. The tensor components g_{ij} re along the j-axis when the magnetic fiel

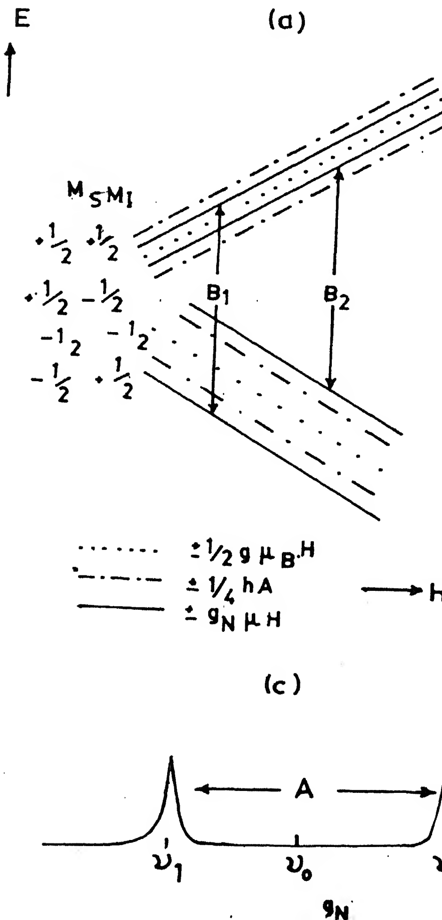

the i-axis. Many nuclei (H through Bi in the periodic table of elements, see table 2) also possess an intrinsic spin angular momentum $I\hbar$ which produces an intrinsic magnetic field of the electron H_e that adds on to H_r so that the new resonance condition becomes

$$h\nu = (H_r + H_e)\, g\mu_B. \qquad (14a)$$

For a nucleus such as ^1H or ^{31}P, $I = 1/2$ so that in the applied field H the nucleus may take up one of the two configurations $M_I = +1/2$ or $M_I = -1/2$, where M_I is the z-component of the nuclear spin quantum number. The two applied fields at which resonance will occur are:

$$H = h\nu/g\mu_B = H_0 \pm H_e = H_0 - aM_I. \qquad (16)$$

Thus ESR is split into two, or, in general $(2I+1)$ line 'hyperfine structure', a being the hyperfine splitting constant. The origin of the hyperfine field H_e is traced to the nonzero probability of the unpaired electron being found at the nucleus. This probability is maximum for electrons in s-orbitals, where wave functions are isotropic. The mutual magnetic interaction between the electron and the nuclear dipoles gives rise to the anisotropy of the hyperfine interaction.

Including the hyperfine interaction, as also the nuclear Zeeman interaction and the electric quadrupole interaction, (15a) becomes

$$\hat{\mathcal{H}} = \mu_B \hat{S} \cdot \tilde{g}\, \hat{H} + h\hat{S} \cdot \tilde{A}\, \tilde{I} - g_N \mu_N \hat{I} \cdot \hat{H} + h\hat{I} \cdot \tilde{Q}\, \hat{I}, \qquad (17)$$

where I_N and μ_N are the nuclear g-factor and nuclear Bohr magneton respectively, and, $\tilde{A}$ and $\tilde{Q}$ are the hyperfine and quadrupolar interaction tensors, symmetric and diagonalizable. In the next section, the g- and A-tensors are related to physical quantities. Equation (17) is the spin Hamiltonian (Abragam and Bleaney 1989) — generally a polynomial in S_{eff}, the effective spin angular momentum — where $2\,S_{\text{eff}} + 1$ equals the total number of electronic states whose properties are being described and which may be used to determine the energy levels of the spin system and thus deduce the ESR transition frequencies. Therefore, the spin Hamiltonian such as (17) makes the contact between theory and experiment.

Considering the case of a spin-half nucleus containing

$|-\frac{1}{2}, -\frac{1}{2}\rangle$ define the four spin stat given by:

$$E = M_s, m_I \mid \hat{\mathcal{H}} \mid M_s, m_I\rangle$$

$$= M_s g\mu_B H + M_s m_I ha - m_I g_N \mu_N$$

Figure 4 shows these levels as a ESR selection rule $\Delta M_s = \pm 1$ corr in the spin angular momentum of $\hbar$. and in the presence of hyperfine s change so that the total angular mo spin and the electron spin system implies the extended selection rul The resulting ESR transitions are

$$h\nu = g\mu_B H_0 \pm \tfrac{1}{2} ha.$$

From (16) and (14b), $A_{\text{iso}} = h\ a/g\mu_B$ hyperfine interaction (see § 5).

ESR measures 'g' and hyperfi but does not measure g_N because energy does not normally affect t Thus the unambiguous identificat nucleus is generally impossible possible to resolve the ambigui establishing ESR ($\Delta M_s = \pm 1$, $\Delta m_I =$ netic resonance (NMR), (i.e. the r radio frequency radiation b ($\Delta M_s = 0, \Delta m_I = \pm 1$)) in a techni nuclear double resonance' or END this technique, the magnetic mome beam of hydrogen atoms has been (Winkler *et al* 1972).

4.2 *Electron nuclear double reso*

Electron nuclear double resonanc technique in which the conditions ESR and NMR are established si be easily seen from figure 4. To magnetic field is set at one of the H_1) and the microwave power lev transition is partially saturated. Th field at high power is applied and

R selection rule is the opposite of the ESR selection $M_s = \pm 1,\ \Delta m_I = 0)$.

$$_1 = -\frac{ha}{2} + g_N \mu_N H_0 ,$$

$$_2 = \frac{ha}{2} + g_N \mu_N H_0 . \quad (20)$$

nportant to note from (20) that while the difference measures a directly, the mean frequency $(\nu_1 + \nu_2)/$ sures g_N and unambiguously identifies the interacting s. (See table 2 for g_N values of magnetic nuclei). principal advantage of the basic ENDOR technique mbines the resolution of ESR with the sensitivity IR is the precise determination of the spin Hamil- parameters, due to the greater rate of energy tion at microwave frequency and the greater tion differences involved in the ENDOR levels. hermore, ENDOR spectra are simpler than the ponding ESR spectra. If several nuclei with the or similar interactions are coupled to the unpaired n, the ESR pattern becomes complicated and the hyperfine' structure is not usually resolved. But OOR, all nuclei with the same interaction can give only two ($S = 1/2$) ENDOR lines which greatly e the resolution.

he semiconducting materials containing impurities, discussed later, as in X-irradiated alkali halides, alkaline–earth halides and oxides (Henderson and on 1973; Spaeth and Koschnick 1991), the ENDOR a are markedly dependent on the orientation of the line solid in the applied field, so that the Hamil- of (17) is now anisotropic. The point symmetry defect (e.g. tetrahedral for Si and octahedral for at Mg^{++} site) helps to determine at least one pal axis of the defect so that the latter can be ied. In diagonal form (17) is

$$\mu_B \Sigma g_{ii} H_i \hat{S}_i - g_N \mu_N H \cdot \hat{I} + h \Sigma A_{ii} S i I_i + h \Sigma Q_{ii} \hat{I}_i \hat{I}_i , \quad (21)$$

H, $\hat{S}$ and $\hat{I}$ are written in the principal axis system A, and Q tensors.

t generally the electron interacts with n-shells tuted by first ($n = 1$), second ($n = 2$) etc nearest ours in the crystal structure) of equivalent nuclei

which has eigenvalues

$$E = M_s g_{\text{eff}} \mu_B H + \sum_n \left\{ - m_I(n) g_n \mu_N H + h M_s m_I(n) \right.$$

$$\times [A(n) + B(n)] \left\{ 3\cos^2\theta + \frac{1}{2} h P_n [3\cos^2\theta_n - 1 \right.$$

$$\left. \left. \times \left[m_I^2(n) - \frac{I(I+1)}{3} \right] \right\} \right\} ,$$

where g_{eff} is the effective g value, $A_0(n)$ and $B(n)$ isotropic and anisotropic hyperfine structure para corresponding to the nth nucleus ($A_0 = 1/3(A_{xx} + A_y$ and $B = 1/6(-A_{zz} - A_{xx} - A_{yy})$), θ_n is the angle m the symmetry (Z) axis of the paramagnetic c (which is along the magnetic field) involving t nucleus, with the principal axis of the complex.

And the total nucleus spin quantum number m the nth shell is given by

$$m_I(n) = \sum_k m_I(k)$$

$$= kI, kI - 1, \ldots - (kI - 1), k\delta .$$

The intensity of each hyperfine components depe (i) the number of ways in which $m_I(n)$ is comp and (ii) the abundance of isotopic species (table

The case of ENDOR of transition metal ion, s interstitial Cr^+ in Si due to Si ligands, illustrates a with $S > 1/2$ and $I = 1/2$. The effective spin Hami for this system with $S = 1/2$ is

$$\hat{\mathcal{H}} = g\mu_B H \cdot S + 1/6a [S_x^4 + S_y^4 - S_z^4 - 1/5\, S(S+1)$$

$$\times (3S^2 + 3S - 1)] + \sum_i (S \cdot \tilde{A}_i I_i - g_N \mu_N H \cdot I_i).$$

Here, the first term describes the impur electron–magnetic field interaction, the second t the cubic field splitting i.e. the splitting of the state multiplet of Cr^+ by a crystalline electric f cubic symmetry, the third term is the interaction b the impurity electron and a ^{29}Si nucleus, and t term represents the nuclear Zeeman interaction.

4.3 *Electron spin echo technique*

Advanced materials are not often available in single crystal form but are readily obtainable as ceramics and glasses, and they often give broad EPR spectra (linewidth ~ 1 mT, even at low temperature) due to strains and unresolved magnetic interactions due to nearby nuclei as seen by ENDOR in favourable cases. But in cases where this broadening is not resolved, one needs a technique to overcome this problem. This is possible through the electron spin echo technique that utilizes the programmed pulsed excitation of the sample through the inherently coherent, high power microwave radiation and detects the 'echo' signals that the sample 'emits' which may be observed in the time domain to obtain 'phase memory' or 'spin coherence times' of the spin system. Let us illustrate the principle of two-pulse spin–echo formation (Slichter 1978). Let at time $t<0$ or O^- (figure 6a) the equilibrium magnetization (M_0) of the spin system point along z-axis of an orthogonal co-ordinate system. Then at $t=0$, upon application of a $\pi/2$ or 90° pulse of microwaves, M_0 would be tilted by 90° away from its equilibrium position (figure 6b) parallel to the microwave magnetic field H_1 along x-axis in time $t_w = \pi/2\,|\gamma|\,H_1$, where γ is the gyromagnetic ratio. Left to itself, the pulse will decay, usually exponentially, producing transient or free induction decay of the mag-

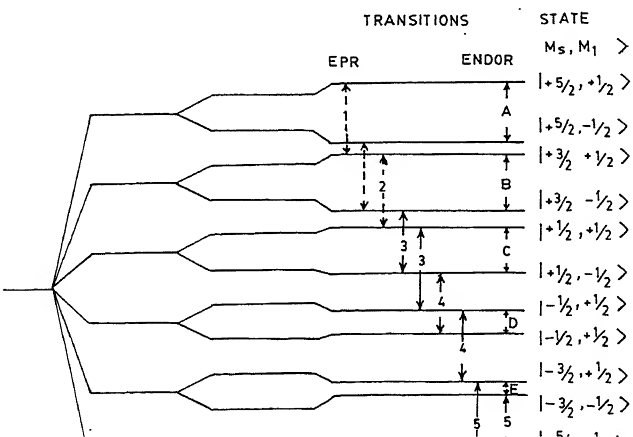

netization (figure 6c). This is du
precession frequencies of inhor
electrons in the sample. A puls
π-pulse applied at $t=\tau$ reverses
electron magnetization vector. No
are not equilibrium ones and the
return to equilibrium at a defini
used to determine the relaxation
The echo is formed 2τ seconds la
a refocusing of all the elements
reconstruction of the original ma

The so-called phase memory
decay of transverse magnetizatio
plane) created by the $\pi/2$ pulse,
relaxation time (T_1) governs the de
magnetization (i.e. M along z-axis)
In fact, T_1 is a measure of the t
magnetization energy to be transf
namic levels of the lattice, and
less for electrons.

In a given material containin
dependence of the echo signal
interval τ, which is usually reco
periments, is governed by: (i) the
relaxation process (T_1 and T_2^*) tha
perturbed by microwave pulse to
and (ii) the frequently observed int
electrons with magnetic nuclei
the echo signal decay or 'electro
modulation'.

These two processes are statist
thus one observes a product of r
and oscillating functions that g
nuclear environment around t
(Dikanev and Ashtashkin 1989; I

5. The ESR spectrometer

5.1 *The continuous wave ESR s*

The continuous wave (CW) ESR
guished from the pulsed ESR expe
later, is a steady-state experiment,
of the unpaired electron spin sy

y and measured by comparison with a quartz standard in the frequency counter. A linearly static magnetic field derived from an electromagnet ie pole pieces symmetrically flanking the cavity, superconducting magnet separates the Kramers' ts (i.e. two energy levels that differ only in spin tion) and prepares the sample for the resonance nent. The typical spectrometer for X-band ESR is shown in schematic in figure 7. The typical s used and the magnetic field patterns inside them o shown (figure 8). These cavities which may be to the incoming microwaves concentrates the on in its standing wave pattern. The sample is in the region corresponding to the maximum vave magnetic field. The level of power in the may be ascertained by tapping a fraction of it to stal (Si-rectifier) detector which converts the vave radiation into a dc signal.

nall alternating magnetic field modulation (figure per-imposed on the static field, enables the field swept through resonance twice during each cycle. tput signal from crystal detector will be modulated e the frequency of modulation. For high sensitivity odulation frequency should be high compared to frequency. Of course there is a trade off between equency and the excess noise produced by the ng system. There is a broad minimum around Iz, which corresponds to the maximum sensitivity, e excess crystal noise ($1/f$ noise) at 100 KHz is very small. This fact coupled with the simpli design has made 100 KHz as the standard moc frequency of most commercial spectrometers. Us pair of modulation coils are embedded in the the cavity whose walls are thin enough to let the 1(modulation without attenuation but thick enough short for microwave frequencies. The static m field strength required depends on the microwav employed. X-band (3·2 cm) work requires up to while for Q-band (~ 8 mm) work fields ~ 1·3 T are Work at shorter wavelengths (higher frequencies as 4 mm and 2 mm requires superconducting n which produce fields ~ 5 T. The magnetic field n uniform over the volume of the specimen, to the of 0·1 ppm to resolve spectra to better than 25 2·5 μT). Therefore it has to be stabilized and co by a Hall-effect probe located in the magnetic nuclear magnetic resonance fluxmeter (Gaussm employed to measure the magnetic field and m be used for stabilization. Resonance field positi usually accurate to 5 significant figures.

The usual method of detection is based on the heterodyne' principle of mixing the signal reflecte cavity with the output of a local oscillator (K operating at 39 MHz above or below signal K to produce an intermediate frequency, which in amplified and detected. (Note that 30 MHz as me before corresponds to maximum sensitivity). detection, 100 KHz signal is sent to a narrov

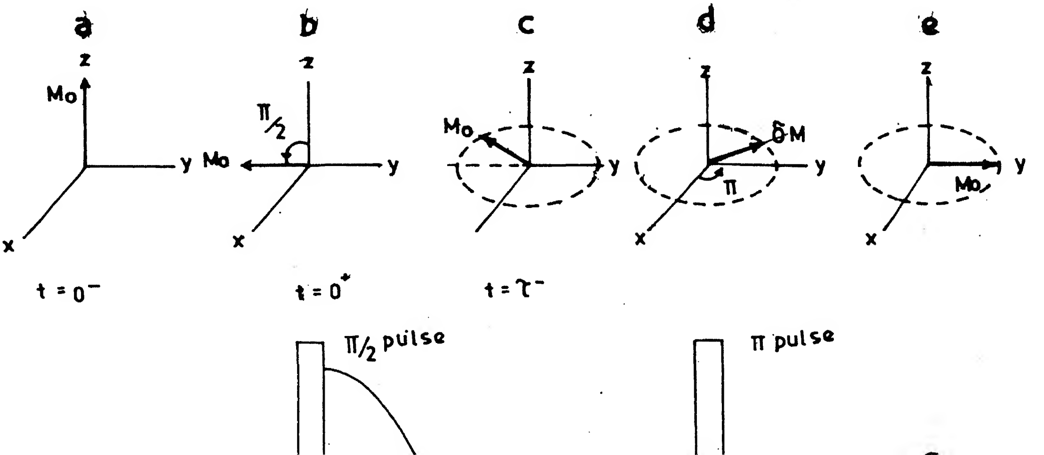

amplifier and then on to a phase sensitive detector. The operation of the latter is as follows: The amplified signal is mixed with the output of the modulating 100 KHz oscillator. If the two signals are in phase opposition, the output of the system is minimum, if the two phases coincide exactly, the output is maximum. The composite signal is rectified, filtered and recorded. The output signal, i.e. the final ESR spectrum naturally depends markedly on the relative phase and amplitude of the signal and reference voltages. The signal shapes before and after phase sensitive detection are shown in figure 9b.

The actual signal from the spectrometer is proportional to the first derivative of the absorption line contour. If signal dispersion is to be avoided, the amplitude of modulation sweep must be less than half the linewidth of the spectral line (figure 9a). The sensitivity of detection and display system depends only on the bandwidth of the actual recording equipment.

The voltage output of the phase-sensitive detector may be changed to a pulse train by a voltage-to-frequency counter and these pulses are counted and stored in the channels of the signal averager, which enables repetitive scans to be made through the spectrum to improve signal to noise ratio. Finally the output may be plotted as a curve or digitized using an analog-to-digital converter and computer-interfacing electronics.

5.2 *The pulsed ESR spectrometer*

The pulsed or the Fourier transform ESR spectrometer system (figure 10) detects the resonance in the time domain by observing the recovery of the magnetization of the spin system from a condition of extreme non-equilibrium to which it was deliberately driven previously.

In a simplified version of a pulsed-ESR spectrometer, the microwave radiation, from a high power (~ 1–2 kW) Klystron is converted into microw
by a pulse gate. These pulses are
travelling wave tube (TWT) amp
the resonant cavity situated betw
the electromagnet. The in-phase
ponents of the magnetization recov
simultaneously with separate dete
these two signals are combined
as the Fourier transform output.

A general time-domain spectror
used for relaxation experiments
relaxation times could be measure
or (ii) time-dependence of ESR si
excitation of the sample could b
as a block diagram (figure 11).
the type of pulse sequence necess
The pulse programmer generates
The computer also controls the d
after amplification the ESR signa
bridge, and starts digitizing the si
of the excitation pulse. After re
digitizer transfers the digitized s
which in turn process it and ou
computer also controls the magne
scan the magnetic field (for CW
at a desired value (for time-domai
sensor gives the magnitude of th
main modules of this spectromete
based microwave set up, (ii) th
control (AFC) of Klystron-based
quency oscillator, and (iii) the a
based on an electronic phase shi
correct phase relationship betwee
ESR signal, for any length of tir

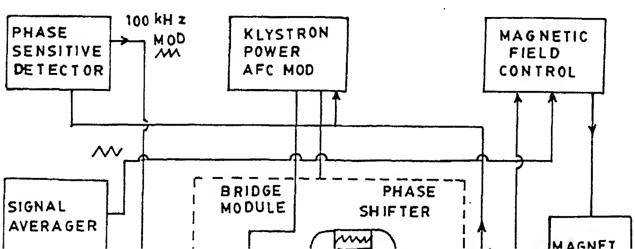

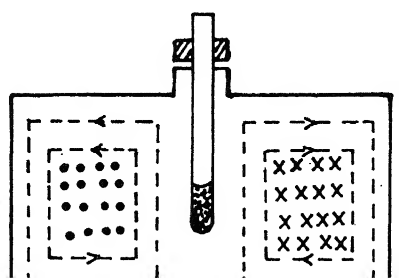

umber of special purpose continuous wave and ESR spectrometers have been built. Salient features ew of these are summarized in table 3.

NDOR spectrometer

NDOR spectrometer monitors and detects changes electron spin populations in a sample subjected imultaneous irradiation at microwave and nuclear tic resonance frequencies, at a dc magnetic field oonding to an ESR transition which is partially ed. This is done by choosing the microwave power nough such that the transition probability for the vave transition far exceeds the spin lattice relaxation vhen the spin levels connected by the microwave on become equally populated. This results in a se and an eventual disappearance of the observed absorption because microwave emission and tion probabilities are equal. But the levels not ted by the microwave transitions are not affected. an ENDOR spectrum would be a record of the s in the ESR signal as the NMR frequency is

The major problem in the ENDOR spectromete get sufficient r.f. power to the sample. There are solutions to this problem: (i) placing an r.f. coil the cavity, either split the cavity to allow r.f. fielc (Holton and Blum 1962) or use a silvered glass This method preserves the Q of the cavity (i.e. sens but is extravagant in the use of r.f. power, and r.f. coil is placed inside the cavity so that less r.f. is required. In any case the r.f. coil is driver power amplifier fed by an external tunable osc The details of the ENDOR experiment are as f The ESR superheterodyne spectrometer (figure 7) i for the observation of dispersion or absorption and the magnetic field is set to the centre of th This line is partially power saturated, while e that the magnetic field stays on resonance. Ther the r.f. oscillator the nuclear transition is observ return of the unsaturated ESR signal. This procedure gives rise to baseline problems beca detection of a small change due to ENDOR in

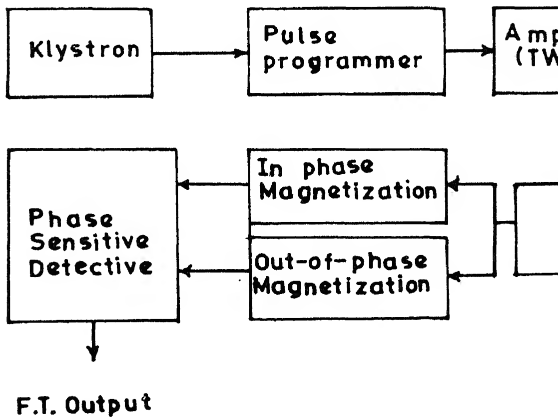

Figure 10. Block diagram of a pulsed ESR spectro

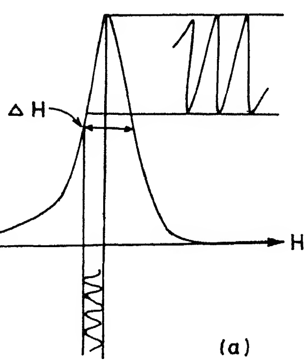

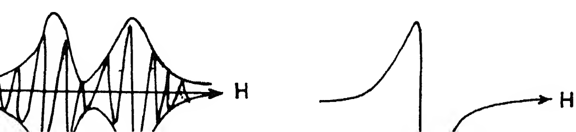

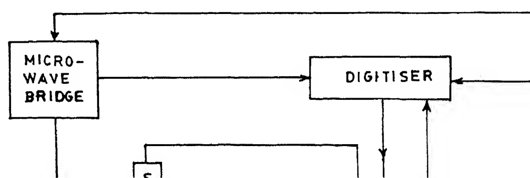

ESR absorption signal. The use of dispersion mode of recording also leads to electronic noise and baseline problems. However, using absorption mode with the r.f. power amplitude modulated at an audio frequency followed by lock-in detection of the ENDOR signal overcomes these problems. In the lock-in detection technique the signal input does not vary in phase relative to the reference signal. Thus the detector output is proportional to the absorption. An output proportional

to the first derivative of the abso
by frequency modulation of r.f
frequency ν_m and using a phase-
reference signal set at ν_m. This m
convenient for investigating hyperf
in materials. Signal averaging in
of the ENDOR spectrometer (Reic
Commercial spectrometers are now
work (Bruker Almanac 1993).

Table 3. ESR spectrometers.

Type	Frequency	Main components and characteristics	
1. Continuous wave (CW), portable	9·1–9·6 GHz	Nd–Fe–B permanent magnet (1·3 T) 275 Hz modulation Volume: $0{\cdot}33 \times 0{\cdot}12 \times 0{\cdot}25\ m^3$	Radiation and ESR
2. CW	300 MHz	Loop gap resonator: 10·2 cm outer diameter, 15·0 cm long with 1·55 cm gap separation Unloaded Q: 5000. Automatic tuning, coupling and phase control circuits. Magnetic field gradient coils	*In vivo* biologica
3. CW	250 MHz	Strip-line type resonator	*In vivo* i
4. CW microstrip induction spectrometer	X-band	Microstrip bimodal square patch resonator Superheterodyne detection	Thin film ESR
5. Pulsed	X-band	Klystron, Waveguide-based diode switches, Boxcar integrator	Measurer lattice rel echo life
6. CW/pulsed	X-band	Computer-controlled magnetic field-microwave frequency interlock saturation recovery	Spin rela radicals, with tran
7. CW/pulsed		High power (1 kW) TWT amplifier. Low power (20 w) CW TWT amplifier	
8. Spin-echo		Pulsed Travelling Wave Tube (TWT) 'pulse former'. Low noice TWT-based homodyne detection	
9. Pulsed/CW (Transmission)	140 GHz	Pulsed: Extended interaction Klystron (300 w). 3·0 T field; Fabry–Perot resonator; signal averaging CW: phase locked 139·5 GHz Gunn oscillator; 500 Hz modulation and phase detection; digital oscilloscope	Dynamic electrons high ser time scal spectral r
10. Magnetic resonance force microscopy		Detection of ESR through periodic saturation of electron spin magnetization; Force between field gradient and spin moments measured with a microcantilever	Imaging

...e ESR spectrum and its analysis

...he ESR spectrum

...ESR spectrum is generally a plot of the first ...ive of the imaginary part of the complex magnetic ...tibility of the paramagnetic system with respect ... applied dc magnetic field. The spectrum may ... of a single line or a group of lines, and could ...vith changes in temperature or the orientation of ...ecimen (e.g. a stretched polymer or a Si single ...) relative to the magnetic field. Four basic quantities ...ble from the spectrum are: (i) g-factor or g-tensor, ...perfine splitting parameter or A-tensor, (iii) line ...and line width, and (iv) double integrated intensity. ...nalysis of these four quantities reveal the following ...ation about the system: (i) the nature of the para...tic centre or complex, i.e. electron or 'hole'-type, ...e precise identity of the complex/centre in terms ...nearest neighbours and symmetry, (iii) the distri... of unpaired spin density over the neighbours, and ...e number of paramagnetic centres per unit volume, ...us the bulk paramagnetic susceptibility of the ....

The g-factor: In the simplest of cases — that of ... spin system $S = 1/2$ with a single line spectrum ... the transition from $M_s = -1/2$ to $M_s = +1/2$ — ...sonance condition $h\nu = g\mu_B H_r$, where h is the ...'s constant and μ_B the Bohr magneton gives ...actor, the frequency ν is accurately known ... is measured accurately from the spectrum. ... $g = 21{\cdot}4198\bar{\nu}/H_r$ ($\bar{\nu}$ in cm^{-1}, H_r in deca Tesla or ...1557×10^{-6} (ν in Hz, H_r in mT)). However, it is ...e to determine g accurately using standard ...s along with the test samples. A selection of these ...tion samples are given in table 4.

...general, neither is $g = 2{\cdot}0023$, the free electron ... nor is it a single number, i.e. isotropic with ... to sample rotation within the magnetic field. The anisotropic g (particularly in materials with tra... metal ions as impurities) arises from the coupl... the orbital angular momentum to the spin ... momentum via spin–orbit interaction. The e... Zeeman interaction responsible for the ESR spect... represented as the leading term in the spin Hamil...

$$\mathcal{H}_Z = \mu_B \hat{S}\tilde{g}\hat{H},$$

where $\tilde{g}$ is a second-rank symmetric tensor and ... effective spin operator. With reference to a Ca... coordinate frame x, y, z in which the electron m...zation is parallel to the applied magnetic field wh... latter has components along x, y and z, $\mathcal{H}_Z$ becc...

$$\mathcal{H}_Z = \mu_B(g_{xx}S_xH_x + g_{yy}S_yH_y + g_{zz}S_zH_z).$$

A study of a monocrystalline material (e.g. BaTiC... or a glassy material (e.g. photochromic glass) is ... at obtaining g_{xx}, g_{yy} and g_{zz} and their direction ... with respect to x, y and z through angular varia... ESR spectrum or computer simulation of observe... trum — a first step in the analysis of the spect... which further details are available. In general, a ... with $g_{av} = (g_{xx} + g_{yy} + g_{zz})/3 > 2{\cdot}0036$, is referred t... 'hole centre' (e.g. V centre in X-irradiated alkali h... while a centre with $g_{av} \leq 2{\cdot}0036$ is called an 'el... excess centre' (F-centre in alkali halides) (Her... and Garrison 1973).

In case of paramagnetic systems, in which the ... and excited states are mixed by spin (S)–orbit ...teraction ($\lambda L \cdot S$), the elements of the g-tensor are ... by

$$g_{ij} = 2\delta_{ij} - 2\lambda \frac{\langle n| L_i |0\rangle \langle 0| L_j |n\rangle}{E_n - E_0},$$

where $\delta_{ij} = 1$ $i = j$ or 0 otherwise, $|0\rangle$ is the ... singlet ground state of energy E_0, $|n\rangle$ is the excite... of energy E_n and λ is the spin–orbit coupling c...

...le 4. Standards for calibration of g-values.

...dard	g-value	ΔH_{pp} (mT)	Spin concentratio... (cm^{-3})
...H (Di phenyl picryl hydrazyl	2·0037(2)	0·28	$1{\cdot}5 \times 10^2$

(see table 2 for numerical values of λ). The larger the λ, the larger is the deviation of g from 2·0023, the 'free spin' value.

6.1b *The hyperfine coupling constant (A)*: Just as the quantization of electron spin produces the simple ESR spectrum, quantization of the nuclear spin $(I, (2I+1)\,m_I)$ of the magnetic nucleus associated with the unpaired electron (e.g. H atom, $S=1/2$, $I=1/2$) gives rise to additional splitting of levels $(\Delta M_s = \pm 1, \Delta m_I = 0)$ due to the interaction between the electronic magnetic dipole and nuclear magnetic dipole.

In terms of the spin operators S and I,

$$\mathcal{H}_{hf} = S \cdot A \cdot I, \tag{28}$$

where A is a symmetric second-rank tensor like g. In a reference frame xyz where A is diagonal,

$$\mathcal{H}_{hf} = A_{xx} S_x I_x + A_{yy} S_y I_y + A_{zz} S_z I_z\,. \tag{29}$$

In a majority of cases, however, the A-tensor is axially symmetric, so that

$$\mathcal{H}_{hf}\,(\text{axial}) = A_{\parallel} S_z I_z + A_{\perp}(S_x I_x + S_y I_y), \tag{30}$$

where z-axis being the axis of symmetry of the complex containing the unpaired electron. The A-tensor contains information about (i) isotropic contribution (A_{iso}), due to s-electron density at the magnetic nucleus and (ii) the anisotropic contribution due to the spin and orbital dipole–dipole interactions with the nuclei. The so-called Fermi-constant interaction is the origin of $A_{iso} = (A_{\parallel} + 2A_{\perp})/3$. This interaction is given by

$$\mathcal{H}_{contact} = \frac{8\pi}{3}\, g \cdot \mu_B g_N \mu_N\, |\psi(0)|^2 \quad \text{S.I.}, \tag{31}$$

from which

$$A_{iso} = \left(\frac{8\pi}{3}\right) g \mu_B g_N \mu_N\, |\psi(0)|^2$$

$$= 4{\cdot}24\, g_N\, |\psi(0)|^2 \text{ (mT) using } \mu_N = \mu_\beta/1836, \tag{32}$$

where g and g_N are electron and nuclear g factors and μ_B and μ_N are Bohr and nuclear magnetons, and $|\psi(0)|^2$ (in cm^{-3}) is the unpaired electron density at the

A_{iso} (theory) has been computed atoms from H to Bi (McMillan the case of paramagnetic ions suc give a large value of A_{iso}, despite density at the nucleus, Fermi con account for A_{iso}. In such cases electrons (e.g. $3s$ in the case of the valence electrons, and these 'c have a sizeable spin density at give a large A_{iso} given by:

$$A_{iso}\ (\text{core polarization}) =$$

$$\frac{8\pi}{3}\, g_\rho \mu_\beta g_I \mu_I \sum_{ns} \{ |\psi_{ns}(0)|\uparrow$$

where arrow '↑' indicates the spin electron (McMillan 1974).

The anisotropic part of the A_{aniso} is due to the dipole–dipol electron and nuclear dipoles.

$$\mathcal{H}_{dipolar} = g_e g_N \mu_B \mu_N \left[\frac{S \cdot I}{r^3} - \frac{3(S\right.$$

which may be written in terms o the vector (r) joining electron magnetic field

$$\mathcal{H}_{dipolar} = g_e g_N \mu_B \mu_N \left(\frac{3\cos^2\theta -}{r^3}\right.$$

In terms of equivalent magnetic f action gives rise to the anisotro interaction

$$A_{aniso} = \mu_N g_N \left\langle \frac{3\cos^2\theta - 1}{r^3} \right\rangle I_z,$$

spatially averaged over all of the function. A_{aniso} is thus proportiona

A typical polycrystalline ESR sp anisotropic g- and hyperfine stru Cu^{++} in $KHSO_4$ (Ramasastry and an environment of rhombic sy figure 12.

larly for transition metal ion ESR. If $\Delta t = T_1$, the
ıttice relaxation time, then the magnitude of T_1
decide the 'lifetime' broadening and linewidth.
newidth is related to the intensity through the
pe function because the computation of the
dth depends on the lineshape function.
vidual ESR signals usually have two familiar shapes
1983) — the Lorentzian and Gaussian shapes —
mer is due to a homogeneous broadening mecha-
n which all dipoles experience the same static
me average magnetic fields but different instan-
s magnetic fields. The latter corresponds to the
f inhomogeneous broadening in which the dipole
ected to slightly different effective magnetic fields
t at a given time only a small fraction of the
s in resonance as the external magnetic field is
through the line. Thus the observed signal is a
osition of a large number of slightly staggered
ual 'spin packets' or an envelope. An inhomo-
s magnetic field or anisotropic interactions (g-
perfine structure) in materials like glasses and
cs or unresolved hyperfine structure results in
an shapes. Metal clusters and conduction electrons
als give Lorentzian and the Dysonian ESR lines
ively, while defects and free radicals in insulators
aussian lines. Normalized plots of Lorentzian and
an lineshapes are shown in figure 13 (Sunandana
while the mathematical expressions for possible
pes are given in table 5. Lorentzian lines are
r than those broadened by T_1. A relaxation time
ld be related to the width of the normalized line,
absence of saturation, as

$$\begin{Bmatrix}\text{shape}\\ \text{constant}\end{Bmatrix}\begin{Bmatrix}\text{gyromagnetic}\\ \text{ratio}\end{Bmatrix}\begin{Bmatrix}\text{linewidth at}\\ \text{half height}\end{Bmatrix}, \quad (39)$$

the shape constant is unity for Lorentzian and
2 for Gaussian lines. $1/T_2$ being a linear function
width, includes 'lifetime' or T_1 broadening and
homogeneous mechanisms characterized by T_2' so

$$= \frac{1}{T_2'} + \frac{1}{2T_1}, \quad (40)$$

ne spin–spin relaxation time, usually $\ll T_1$ for free

sample and to the net paramagnetic susceptibility
sample.

Assuming that (a) ESR lineshape is Lorentzi
the Curie law (i.e. $\chi \propto 1/T$) is applicable, (
microwave power applied to the sample does not s
the resonance, and (d) the signal-to-noise ratio
ESR cavity is unity, the ESR detection sensiti
the minimum number of paramagnetic centres de
in ESR (N_{min}) Feher (1959) is given by

$$N_{min} = \frac{3 V_c k T_s \Gamma}{2\pi g^2 \mu_B^2 S(S+1) H_1 Q_u'} \left(\frac{F k t_d b}{P_0}\right)^{1/2},$$

where V_c is the volume of the rectangular cavity o
in the TE_{102} mode; k the Boltzmann constant;
sample temperature; Γ the half width at half ma
(Gauss) of the absorption line; H_r the magnetic
the centre of the absorption line; Q_u' the effective u
Q factor of the cavity $= Q_\varepsilon Q_u/(Q_\varepsilon + Q_u)$ (Q_ε the di
Q, Q_u = unloaded Q); T_d the detector temperature
bandwidth (Hz) of the entire detecting and amp
system; P_0 the microwave power (erg/s) incident
cavity; F the noise figure (due to sources oth
thermal detector) = 1 for an ideal spectrometer.

Typically, $Q_u' = 5000$, $T_s = T_d = 300$ K, H_r
$\Gamma = 0{\cdot}1$ mT, $g = 2{\cdot}00$, $S = 1/2$, $V_c = 11$ cc (X-band
cavity); $F = 100$; $b = 1$ Hz; $P_0 = 10^6$ erg/s = 100 m
that $N_{min} \approx 10^{11}$ ('Worst case sensitivity') (We
Bolton 1972).

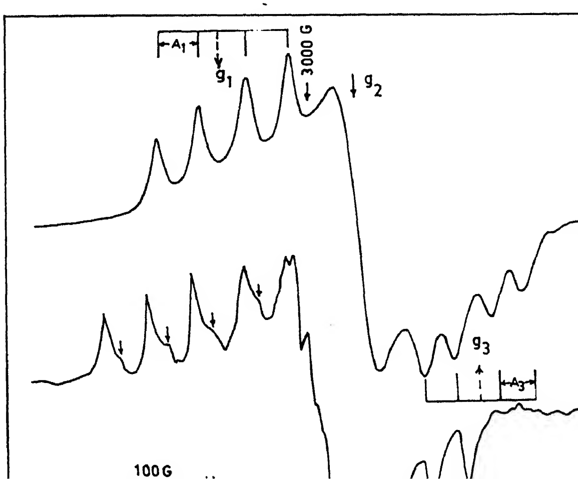

The absolute intensity of the observed ESR signal is determined by: (i) the area under the absorption curve or the double integrated first derivative curve (A), (ii) modulation amplitude (M), (iii) amplitude of the magnetic component of microwave field (H_1) at the sample. H_1 is a function of P_0, Q_u' and its own distribution within the cavity, (iv) the receiver gain of the spectrometer (G), (v) sample temperature, (vi) g-factor, (vii) microwave frequency, and (viii) filling factor (η) . $\eta \sim 2V_s/V_c$, where V_s is the sample volume and V_c the cavity volume.

Assuming that the geometry of the are the same, so that H_1 is the sam neither the standard nor sample s concentration $[x]$ of the paramagneti sample is given, relative to that of by

$$[x] = \frac{[\mathrm{std}] A_x G_s M_s g_s^2 \, [S(S+1)]_{\mathrm{std}}}{A_s G_x M_x \, (g_x)^2 \, [S(S+1)]_x},$$

provided the scanning of the magne

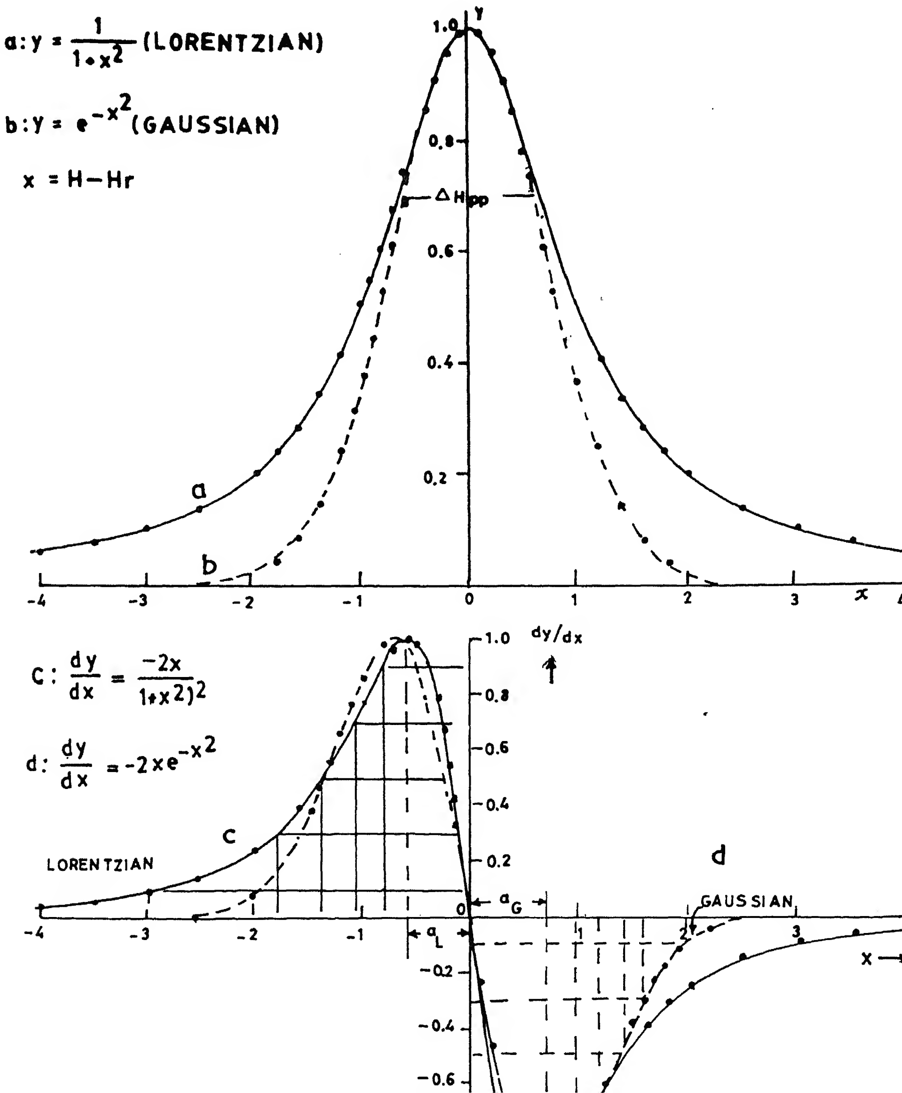

ble 5. ESR lineshapes.

sorption lineshape d linewidth)	First derivative absorption: Lineshape	First derivative absorption: Linewidth (fullwidth at half maximum) $\Delta H_{1/2}$	Area
rentzian			
$\text{H)} = \dfrac{y_{\mathrm{m}}}{1 + \dfrac{(H-H_{\mathrm{r}})}{\frac{1}{2}\Delta H_{1/2}}}$	$\dfrac{\mathrm{d}Y^{\mathrm{L}}}{\mathrm{d}H} = \dfrac{16 y_{\mathrm{m}'} \dfrac{(H-H_{\mathrm{r}})}{\frac{1}{2}\Delta H_{\mathrm{pp}}}}{3 + \left[\dfrac{(H-H_{\mathrm{r}})}{\frac{1}{2}\Delta H_{\mathrm{pp}}}\right]^2}$	$\sqrt{3}\Delta H_{\mathrm{pp}}$	$\dfrac{2\pi}{\sqrt{3}} Y_{\mathrm{m}'} (\Delta$
$= \text{maximum amplitude}$; $\text{I}_{1/2} = \text{half-amplitude linewidth}$	$y_{\mathrm{m}'} = \text{total vertical height}$; $H_{\mathrm{r}} = \text{resonance field}$; $\Delta H_{\mathrm{pp}} = \text{peak-to-peak width}$		
ussian			
$= Y_{\mathrm{m}} \exp\left[-0.693\left[\dfrac{H-H_{\mathrm{r}}}{\frac{1}{2}\Delta H_{1/2}}\right]^2\right]$	$\dfrac{\mathrm{d}Y^{\mathrm{G}}}{\mathrm{d}H} = y_{\mathrm{m}'}\left[\dfrac{H-H_{\mathrm{r}}}{\frac{1}{2}\Delta H_{\mathrm{pp}}}\right] \exp\left[-\dfrac{1}{2}\left\{\left(\dfrac{H-H_{\mathrm{r}}}{\frac{1}{2}\Delta H_{\mathrm{pp}}}\right)^2 - 1\right\}\right]$	$\sqrt{2\ln 2}\cdot\Delta H_{\mathrm{pp}}$	$(2\pi e) Y_{\mathrm{m}'} (\frac{1}{2}$
igt			
$= \dfrac{\sqrt{\ln 2}}{\pi}\left(\dfrac{\Delta H^{\mathrm{L}}_{1/2}}{\Delta H^{\mathrm{G}}_{1/2}}\right)x \dfrac{e^{-x^2}\,\mathrm{d}x}{\left(\dfrac{\Delta H^{\mathrm{L}}_{1/2}}{\Delta H^{\mathrm{G}}_{1/2}}\right)^2 \ln 2 + \left(2\sqrt{\ln 2}\left[\dfrac{H-H_{\mathrm{r}}}{\Delta H^{\mathrm{G}}_{1/2}} - x\right]\right)^2}$			
$\text{I}^{\mathrm{V}}_{\mathrm{pp}}\,(\text{observed}) = \dfrac{\Delta_{\mathrm{G}}^2 + 0.9085\,\Delta_{\mathrm{G}}\Delta_{\mathrm{L}} + 0.4621\Delta_{\mathrm{L}}^{2\mathrm{S}}}{\Delta_{\mathrm{G}} + 0.4621\,\Delta_{\mathrm{L}}}$			
$,\ \Delta_{\mathrm{G}} = \text{Assumed Lorentzian and Gaussian half-widths}$			
sonian			
$= -\left[\dfrac{\omega H_1^2 R^2 \omega_0 x_0 T_1 A \delta}{8}\right] F_{\mathrm{D}}(R, x, \chi, \eta)^*$			

oole 1983
oneham A M 1972 *J. Phys.* **D5** 670

$$_{\mathrm{D}}(R, x, \chi, \eta) = \left\{ \frac{R^4(x^2-1) + 1 - 2R^2}{\ldots}\left[\frac{2\chi}{\ldots} + R^2(x+1) - 3\right] + \frac{2R^2(1-R^2x)}{\ldots}\left[\frac{2\eta}{\ldots} + R^2(x-1) - 3\right]\right\}$$

the same way for standard and sample. If the lineshape of the ESR signal is accurately known (to be Lorentzian or Gaussian) then an estimate of the number of spins per unit volume (N_s) may be made using the formula

$$N_s = I_{pp} \Delta H_{pp}^2, \tag{43}$$

where I_{pp} is the peak-to-peak amplitude (intensity) and ΔH_{pp} the peak-to-peak width of the resonance line. Kwan and Yen (1979) have given the modified, easy to apply, but exact formula

$$N_s = 0{\cdot}285\, I_{pp} \Delta H_{10}^2, \tag{44}$$

where ΔH_{10} is the width at the position 1/10 of the peak-to-peak height of the first derivative curve.

The high frequency magnetic susceptibility involved in ESR is $\chi^* = \chi'(\omega) - i\chi''(\omega)$, where $\chi'(\omega)$ is the real part or the dispersion component, and $\chi''(\omega)$ is the imaginary or absorption component (strictly speaking χ'' is also a function of magnetic field which considerably alters the description of ESR spectra (Zhong and Pilbrow 1991)). The measurement of the usually processed ESR absorption signal, proportional to $\chi'' H_1$ or the derivative proportional to $d(\chi'' H_1)/dH_1$, where H_1 is the strength of the microwave magnetic field, leads to the paramagnetic susceptibility of the sample. But unlike in the conventional measurement of χ using Faraday or Guoy balance or vibrating sample magnetometer there is no need to correct for the diamagnetic contribution to χ in the ESR measurement.

The absorption susceptibility is given by

$$\chi'' = P_0 (2\omega H_1^2)^{-1}, \tag{45}$$

where P_0 is the power absorbed by the spin system when the microwave held H_1 is perpendicular to static field H and $\omega = 2\pi\nu$, ν being the microwave frequency. For an unpaired spin system $S = 1/2$ with isotropic g

$$\chi'' = \delta N \frac{1}{4} \pi g^2 \beta^2 \frac{f(\nu - \nu_0)}{h}, \tag{46}$$

where $\delta N = N(+1/2) - N(-1/2)$, the population difference between states with $M_s = +1/2$ and $M_s = -1/2$ and of the population difference. For an
broadened ESR signal i.e. one due t
whose resonance fields form a Gaussian
to unresolved hyperfine interactions o
nearby magnetic nuclei, the steady stat

$$\frac{d}{dt}(\delta N) = 0 = \frac{1}{T_1}[(\delta N)_0 - \delta N] - 2\delta N W$$

where W is probability for the $M_s = +$
transition, given by $\pi^2 (g^2 \mu_B H_1)^2 f(0)/h$

$$\delta N = (\delta N)_0 \left[\frac{1 + 2\pi^2 (g\mu_B H_1)^2 T_1 f(0)}{h^2} \right]$$

and finally

$$\chi''(\nu_0) = (\delta N)_0 \frac{1/4\, \pi (g\mu_B)^2 f(0)}{h} \times \left[\frac{1 + 2\pi^2 (g\mu_B H_1)^2\, T_1 f(0)}{h^2} \right]$$

Thus for small H_1, the ESR absorption
proportional to H_1 while for large H_1
proportional to H_1 (figure 14) (Sunan
to the saturation factor or the expression
For measurements of spin concentration
it is important to avoid saturation
measurements are made on saturated E

6.2 *Analysis of ESR spectra*

Advanced materials may be
microcrystalline or glassy, and, thus,
may be rich and well-resolved or poorly
crystal ESR spectra contain maximum
way of well-resolved and narrow lines
netic centre trapped at several symmetry
cally distinct sites in the crystal lattic
often having magnetic neighbours tha
with the unpaired electron. However,
poly-crystalline or glassy materials of
poorly resolved/unresolved features fro
to extract spin Hamiltonian parameter

s and sometimes from the neighbouring magnetic as in silicon alkali halides.

task of deducing the principal g- and A-values two tensors begins with the identification of three lly perpendicular directions in the crystals (e.g. [010] and [001] axes of an orthorhombic crystal). need not always correspond to the crystallographic Then ESR spectra are recorded for rotations of ystal mounted on a specially designed goniometer 15), about each of the three orthogonal axes, say and z-axes. The rotations about a given axis, say i.e. in a given plane yz are affected every 5° or pending on the magnitude of the anisotropy. From ree sets of spectra arising from rotations about axes, 'isofrequency plots' are generated, plotting onance magnetic field of each observed line against entation θ of the crystal (in a given plane) relative dc magnetic field. After identifying groups of corresponding to either chemically distinct centres sically distinct but chemically equivalent centres, d plots of g^2_{ij} or $(g^4A^2)_{ij}$ (ij = xy, yz, zx) vs θ are Thereafter each of the observed plots are fitted, method of least squares to the expression

$$(\theta) = U + V\cos 2\theta + W\sin 2\theta, \tag{49}$$

similar equation for g^4A^2), where

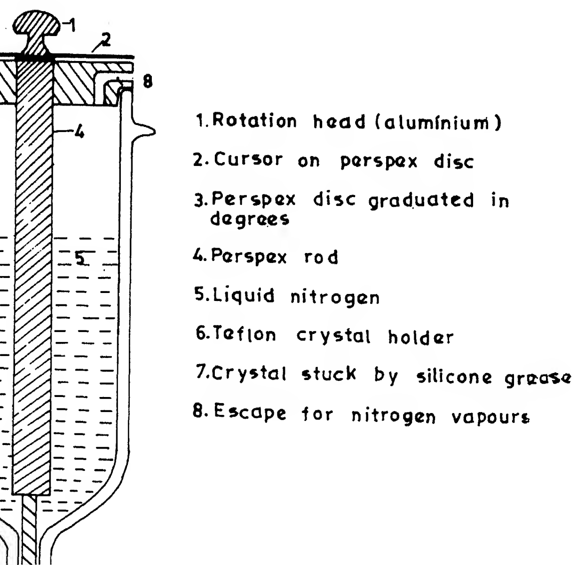

$$U = \frac{g_{ii}^2 + g_{jj}^2}{2},\ V = \frac{g_{ii}^2 - g_{jj}^2}{2}\ \text{and}\ W = g_{ij}^2.$$

Then the elements of the g^2 or hyperfine tens found and the matrix formed is symmetrizec diagonalized either directly, or using the Schor (1959) method. This latter method consists in acc locating the maxima and minima, using the r $\tan 2\theta = W/V$ and forming the matrix elements as fo

$$\{g^2\} = G = \begin{bmatrix} G_{XX} & G_{XY} & G_{XZ} \\ G_{YX} & G_{YY} & G_{YZ} \\ G_{ZX} & G_{ZY} & G_{ZZ} \end{bmatrix},$$

where

$$G_{XX} = \alpha_Y + \alpha_Z - \alpha_X,\ G_{YY} = \alpha_Z + \alpha_X - \alpha_Y,$$

$$G_{ZZ} = \alpha_X + \alpha_Y - \alpha_Z,$$

$$G_{YZ} = \pm\sqrt{(\delta_x + \alpha_y - \alpha_z)(\delta_x - \alpha_y + \alpha_z)},$$

$$G_{ZX} = \pm\sqrt{(\delta_y + \alpha_z - \alpha_x)(\delta_y - \alpha_z + \alpha_x)},\ \text{and}$$

$$G_{XY} = \pm\sqrt{(\delta_z - \alpha_x + \alpha_y)(\delta_z - \alpha_x + \alpha_y)}.$$

α's and δ's are determined by the accurately g^2_{max} and g^2_{min} for each of the three rotations a given by

$$\alpha_i = \frac{g^2_{max}(i) + g^2_{min}(i)}{2}\ \text{and}\ \delta_i = \frac{g^2_{max}(i) - g^2_{min}(i)}{2}$$

i = x, y or z.

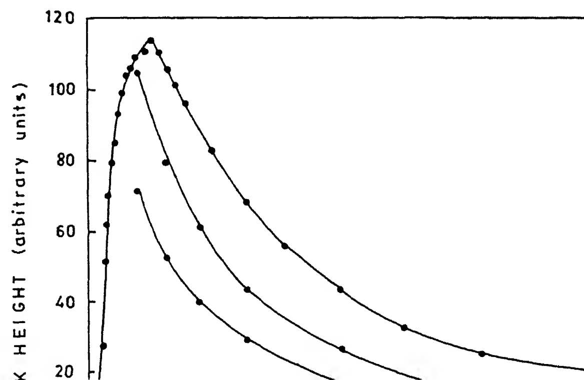

If the paramagnetic centre is found at n_1 sites for rotations about x-axis, n_2 sites for rotations about y-axis and n_2 sites for rotations about z-axis, then one has to sort out the correct matrix elements and matrix out of a possible n_1, n_2 and n_3 combinations of maxima and minima. The choice can be narrowed down by seeking coincidences in the g^2_{ij} values (for example, g^2_{xx} occurs twice, once each for rotations about y and z-axes) (Sunandana 1975). Finally, the diagonalization of the matrix is effected (using Jacobi method for instance) so that

$$\begin{bmatrix} l_{xx} & l_{xy} & l_{xz} \\ l_{xy} & l_{yy} & l_{yz} \\ l_{xz} & l_{yz} & l_{zz} \end{bmatrix} \begin{bmatrix} g^2_{xx} & g^2_{xy} & g^2_{xz} \\ g^2_{xy} & g^2_{yy} & g^2_{yz} \\ g^2_{xz} & g^2_{yz} & g^2_{zz} \end{bmatrix} \begin{bmatrix} l_{xx} & l_{xy} & l_{xz} \\ l_{xy} & l_{yy} & l_{yz} \\ l_{xz} & l_{yz} & l_{zz} \end{bmatrix}^{-1}$$

$$= \begin{bmatrix} g^2_{XX} & 0 & 0 \\ 0 & g^2_{YY} & 0 \\ 0 & 0 & g^2_{ZZ} \end{bmatrix}. \qquad (54)$$

Taking the square root of the elements of the diagonal matrix gives the principal values of g-tensor. The direction cosine matrix gives the directions of $g_{XX}(l_{xx}, l_{xy}, l_{xz})$, $g_{YY}(l_{xy}, l_{yy}, l_{yz})$ and $g_{ZZ}(l_{xz}, l_{yz}, l_{zz})$. Once the principal g- and A-values and their direction cosines are known, the ESR centre can be located in the crystal (Atherton 1973).

Single crystal EPR spectra of transition metal compounds occasionally consist of a single structureless, perfect Lorentzian line, for certain orientation of the crystal that indicate exchange averaging of g- and A-anisotropy and local dipolar fields. Such anomalous angular variation observed in (2,2′-bipyridine–3,3′-dicarboxylic acid) dichloro copper (II) monohydrate, in which long-range exchange interaction via lattice water was observed, has been analysed for the molecular g-tensor using a decoupling procedure that uses a molecular coordinate system and relates it to the crystal axes system through a coordinate transformation, in order to overcome the effect of incomplete averaging of g-anisotropy (Balagopala Krishna and Rajasekharan 1990).

6.2b *Polycrystalline ESR spectra:* Almost all varieties of advanced materials including electro-ceramics, optical materials, catalysts, polymers and glasses are composed of randomly oriented small crystallites. The ESR spectra

equally probable. The number of
field orientation between θ and
and $\phi + \Delta\phi$ are given by the sc

$$\Delta\Omega = \sin\theta\,\Delta\theta\,\Delta\phi.$$

But only a fraction of these ra
to microwave energy absorptio
between H and $H + dH$, this fra
individual linewidth ΔH and the
$H_r - H$. A function $f(H_r - H_1\,\Delta H$
where H_r the resonance field o
itself a function of orientation,
16b. The aim is to determine the
at the magnetic field H. The int
at a given magnetic field is the
defined above and the element of
over all solid angles, because al
to the absorption, in principle:

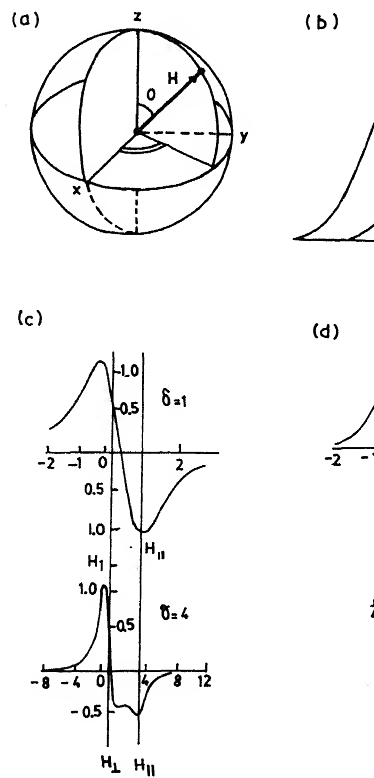

$$= 1/4\,\pi \sum f(H_r - H,\ \Delta H)\,\Delta\Omega_i$$

$$= 1/4\,\pi \sum_{j=0}^{2\pi} \sum_{i=0}^{\pi} f(H_r - H,\ \Delta H)\,\sin\theta_i\,\Delta\theta_i\,\Delta\theta_j$$

$$= 1/4\,\pi \int_0^{2\pi}\int_0^{\pi} f(H_r - H,\ \Delta H)\,\sin\theta\,d\theta\,d\phi\,, \qquad (56)$$

integral sign has replaced summation and $1/4\pi$ normalized factor.

the derivative absorption is usually measured

$$\frac{I}{H} = 1/4\,\pi \int_0^{2\pi}\int_0^{\pi} f'(H_r - H,\ \Delta H)\,\sin\theta\,d\theta\,d\phi.$$

pecific form of the function $f'(H_r{-}H,\ \Delta H)$ depends e shape of the individual derivative curves. For tzian absorption curve,

$$(H_r - H,\ \Delta H) = \frac{16}{\pi(\sqrt{3}\,\Delta H)^3}\,(H_r - H) \times \left[\, i + 4/3\left(\frac{H_r - H}{\Delta H}\right)^2 \right]^{-2}, \qquad (57)$$

H is the swept magnetic field and ΔH the magnetic eparation between the maximum and the minimum derivative curve, assumed to be constant, although be orientation dependent.

spin Hamiltonian for the given situation decides orm taken by H_r. If the paramagnetic centre ences only the Zeeman interaction, and has only mmetry axis along z-axis, then

$$_{x} = g_{yy} = g_{\perp} \text{ and } g_{zz} = g_{\parallel}\,.$$

$$_r = (h\nu_0/\mu_B)\,(g_{\parallel}^2\cos^2\theta + g_{\perp}\sin^2\theta)^{-1/2}, \qquad (58)$$

ν_0 is the experimental microwave frequency. Trivial ons of the above equations occur when θ is $\pi/2$ respectively, when

$$\frac{h\nu_0}{} \qquad \frac{h\nu_0}{}$$

glasses is quite general as there is a distribut anisotropic g-values due to random local str fluctuations, which gives

$$g^2 = g_{xx}^2\sin^2\theta\cos^2\phi + g_{yy}^2\sin^2\theta\sin^2\phi + g_{zz}^2\cos^2$$

where θ and ϕ relates as usual the resonance f the principal axes of the g-tensor. The anis linewidth that occurs in the lineshape function is exp by a similar function

$$\Delta H^{-2} = \Delta H_{xx}^{-2}\sin^2\theta\cos^2\phi + \Delta H_{yy}^{-2}\sin^2\theta\sin^2\phi + \Delta H_{zz}^2\cos^2\theta,$$

where ΔH_1, ΔH_2 and ΔH_3 are the half widths alo principal directions collinear with the correspondin of the g-tensor. Thus the simulated first derivativ spectrum has the general form

$$\iint f\left(\frac{H - H_r}{\Delta H}\right)\sin\theta\,d\theta\,d\phi.$$

The ESR spectrum of amorphous MoS_3 has been sin to obtain reasonably accurate g-values for the s hole centre and Mo(V) ions surrounded by sulph oxygen atoms (Berger and Haddad 1991). Taylo (1975) have given an exhaustive account of the sim of ESR spectra of polycrystalline solids. They treated three cases of usually encountered powder s (I) the most simple case of only the electron Z term i.e. the first term in the general spin Hami

$$\mathcal{H} = \mu_B S\cdot g\cdot H + S\cdot A\cdot I + S\cdot D\cdot S + I.Q\cdot I - \mu_N I$$

being dominant while the four other terms — hyp fine structure (that occurs for paramagnetic ion $S > 1/2$, e.g. Mn ($S = 5/2$) and triplet state organic cule ($S = 1$)) and the much smaller quadruple and Zeeman — are neglected, with two cases (i) symmetry — ($g_{xx} = g_{yy} = g_{\perp}$, $g_{zz} = g_{\parallel}$, $g_{\perp} > g_{\parallel}$) — cor of a shoulder and a divergence, and (b) the com anisotropic (rhombic case) $g_{..} > g_{..} > g_{..}$ (II) the

There exists an important relation between the ESR spectra of powders and those of single crystals: the turning points in the angular dependence of resonance fields of the single crystal determine the peak positions in this spectrum of the corresponding powder. Exploiting this relationship, Van Veen (1978) has shown that the derivatives of the resonant positions with respect to the spin Hamiltonian parameters, including the orientation of magnetic fields, can be used to calculate the peak position and intensities without the need to calculate the powder spectrum completely. He has presented a calculation scheme to simulate a complete powder spectra for spins upto 5/2 (Mn^{2+}) and applied it to the case of Fe^{2}(III) substituted AlOOH (diaspore).

7. Advanced materials and EPR

The EPR technique has been applied for spin identification, spin counting, spin mapping, spin motion and spin imaging of a variety of advanced materials in their solid state including metals and alloys, elemental and compound semiconductors (crystalline and amorphous), alkali and silver halides, transition metal, rare earth and actinide compounds, electroceramics, catalysts, intercalation compounds, polymers, glasses and organic charge transfer complexes, besides superionic conductors and high temperature superconductors. The technique has proved to be specific (local pro dynamic environment), sensitive tions sufficient) to compositio accurate enough to a quantitative (nonperturbing or nondestructive of the specific classes of materials has been applied and the inform

The subsequent sections of th following classes of materials: se polymer materials, glasses and c and superionic materials. A se microscopy discusses the basic pri and microscopy with certain exam work. This is followed by a bri the emerging techniques, which could be routinely applied to selec 'Spin labels' and biological materi proteins (Hagen 1992) have not article although they are of im 'spin label' ESR has been esta physical technique (Humphries a

8. Semiconducting materials

8.1 *General considerations*

Characterization of point defect and those induced by plastic d

Table 6. Basic expressions for generating EPR absorption spectra of powdered materials†.

Type of spectrum	Expressions
(a) Axially symmetric g-tensor, $g_\perp > g_\parallel$ ($g_1 = g_2 = g_\perp$, $g_3 = g_\parallel$) Features: Divergence at $H_\perp = h\nu_0/g_\perp\mu_B$ shoulder at $H_\parallel = h\nu_0/g_\parallel\mu_B$ ν_0 = microwave frequency	$S(H) = \dfrac{(h\nu_0)^2}{\mu_B^2 g_\perp \sqrt{g_\perp^2 - g_\parallel^2}\cdot H^2\sqrt{H^2 - (h\nu_0/g_\perp}$ for $h\nu_0/g_\perp\mu_B \le H \le h\nu_0/g_\parallel\mu_B$ $S(H) = 0$ elsewhere
(b) Rhombically symmetric g-tensor, $g_1 > g_2 > g_3$. Features: Divergence at $H_2 = h\nu_0/g_2\mu_B$ Shoulders at $H_1 = h\nu_0/g_1\mu_B$ and $H_3 = h\nu_0/g_3\mu_B$	$S(H) = \dfrac{2}{\pi}\dfrac{H_1H_2H_3}{\sqrt{H^2 - H_1^2}\cdot\sqrt{H_3^2 - H_2^2}\cdot H_2}\cdot K($ $(H_3 \ge H \ge H_2)$ $S(H) = \dfrac{2}{\pi}\dfrac{H_1H_2H_3}{\sqrt{H_2^2 - H_1^2}\cdot\sqrt{H_3^2 - H^2}\cdot H_2}\cdot K($ $(H \ge H \ge H)$

cal doping and thermal treatment during various of synthesis — is an important first step in the tion of semiconducting materials for applications s integrated circuits, infrared photodiodes and solar More specifically, the characterization of electronic states in a given semiconductor involves three s: (i) the number density of various defects (e.g. in crystalline Si or dangling bonds in amorphous), (ii) the energy position of defect levels relative conduction band/valence band edge, or the energy um which governs the macroscopic properties of miconductor, and (iii) defect wave function which the microscopic structure of the electronic defect, which enables assessment of (a) cross-sections for optical transitions, (b) electron correlation effect (c) metastability of defect densities and sample rative conditions.

7. Principal types of advanced materials studied by EPR.

f material	Information sought
etals and metallic aterials	
rromagnetic etals and alloys crystalline glassy	Magnetic phase identification, magnetization, damping and magnetostriction parameters
perconductors	Metal-insulator transitions, phase purity in ceramics, microwave impedance and penetration depth
miconductors	
crystalline	Defect type location, concentration and geometry
amorphous	Annealing behaviour under plastic deformation, irradiation and implementation
sulators	
organic	
monocrystalline polycrystalline glassy	Microscopic structure and electronic information
ganic	
monocrystalline polycrystalline	Free radical production, identification and detection, kinetics, motion of spin labels
lymers	
conducting	Behaviour under stress, irradiation and chemical doping. Defect

In the testing of semiconductors ESR and El techniques are particularly valuable as they are se to the short-range order of defect states, i.e. the lo of the defect in the crystal lattice/amorphous n and its neighbourhood.

Unpaired electrons in semiconductors — both ele (Si, Ge) and compound (III–V's: InSb, GaAs and I ZnS, CdS) — exist as: (i) electrons localized at i defects (impurity atoms), (ii) electrons in a partly band, and (iii) electrons in broken bonds (like ganic/organic free radicals).

Physically, semiconductors are attractive materi ESR investigations because: (i) they are intrin diamagnetic so that any impurity (H to Ag acro periodic table) could be studied without any interf from host lattice; (ii) these magnetically active imp have limited solubility and give rise to narrow res lines; (iii) they have highly symmetric crystal stru (cubic/hexagonal) with very few atoms per un (typically 2) with tetrahedral symmetry about each point so that theoretical modelling is relatively s (iv) they are tetrahedrally bonded (involving hyb atomic *s*- and *p*-orbitals) and this covalency is m as (a) a reduction in the hyperfine interaction with ion, (b) an additional hyperfine structure with ion, and (c) a reduction in orbital contribution to *g*- and (v) the rather small spin orbit interaction (esp in Si) and long spin-lattice relaxation time make res signals in doped semiconductors easily saturab thus ideal for ENDOR studies and 'spin mappin

Beginning with crystalline silicon-doped with to the present day porous silicon and low-temp GaAs, the ESR characterization continues unabated follows is a brief, material-by-material description. experimental data is compiled in table 8.

8.2 *Silicon*

8.2a *Donors, acceptors and impurities in crystal* Studies on crystalline silicon doped with shallow (P, Ag, Sb and Bi) and shallow acceptor (B, and In) impurities, 3d-transition elements (V, C

in semiconductors and related materials.

g-value(s)	Hyperfine coupling constant*	Location and origin	Remarks	Ref.
2·001(1)			[P]~ 2×10^8/cc Linewidth T-independent, $4 < T < 300$ K	a
0·34, ⊥: 1094 0·73, ⊥: 1·89		As donor dislocation dangling bond (db)	Upon optical (Hg lamp) pumping	**
0·85, ⊥: 1·91		Molecular donor	[0]: ~ 10^{14}/cc Dynamic tunneling system	***
2·019		Midgap db		b
2·012		Conduction band, Ge–Ge antibonding		–
2·053		Valence band Ge–Ge bonding		–
-1·10(5) 0·01(2)		Isolated substitutional N at a trigonal symmetric site		c
2·006 2·0055 ± 0·0002		Surface paramagnetic centre	$\Delta H = 0{\cdot}4$–$0{\cdot}75$ mT Relaxation time = 10^{-6}–10^{-7} s at 300 K – stable – Lorentzian ~ 10^{14} spins/cm^2	****
	^{75}As: 7·3 mT ^{31}P: 4·2 mT		Plastic deformation by (compression) at 1000°C and spectra at 4 K	†
2·00069	H_2: ∥: 217·8 MHz ⊥: 128·2 MHz	Label: Si–NL52	23·200480 GHz	††
2·00951	H^1: ∥ 4·81 ⊥ 1·5 MHz H^2: ∥ 12·1 ⊥ −5·0 MHz	Interstitial site	~ 4·2 K	d
g_2' + 0·002 − 0·031(1)				e

g-value(s)	constant*	Location and origin	Remarks	Ref.
2·0028 3·9846	^{107}Ag: 9·0, 3·9 ^{109}Ag: 10·5, 4·5	Silver impurity (X) pair		–
2·0004 1·9999	$D = 86$ MHz			
2·004 2·0065 2·0022 2·0078		Neutral Fe^0 (?) Si-db at surface/*c*–Si–SiO_2 interface	Xe-Light illumination	+
2·0055		midgap db		b
2·0044		conduction band Si–Si antibonding		–
2·01		valence band Si–Si bonding		–
2·004 2·008	$A_{iso} = 7·3 \pm 0·3$ mT $A_{aniso} = 1·8 \pm 0·3$ mT SHF = 2–3 mT	Si-db		++
2·0055		db		–
2·0012 2·0081		Si ≡ Si	$g_{\parallel}$ ⊥: (111)	
		Pb centre	ace ∥ (111) axes	
2·0005		Si ≡ Si	g_1 ∥ (111) axes	
2·0112		(G8)		
2·0096				
2·0012 2·0135 2·0150		Si ≡ Si at divacancy (G7)	–	+++
2·0023 2·0117 2·0106		Si ≡ Si at pentavacancy (P-1)	–	–
2·0151 2·0028 2·0038		Si–Si bent bond over vacancy (G2)	g_1 ∥ (011) axes	
2·0092 2·0026 2·0033		Si–Si bent bond, vacancy with 0 (B1)	–	

g-value(s)	Hyperfine coupling constant*	Location and origin	Remarks	Ref.
2·0087 1·9989 1·9989		Si–Si bent bond over vacancy	$g_1 \parallel (100)$ axes	
2·0018 2·0005 2·0003		$O_3 \equiv Si\ldots Si \equiv O_3$ at 0 vacancy	E' centre	
2·0026 2·0090 2·0210		Si–O Hole on non-bridging O	HC_1 centre	
2·0007 2·027	$A_{\parallel}/g\mu_B = 12$ mT $A_{\perp}/g\mu_B = 6$ mT	Atomic Cl	upon 100 keV X-irradiation observed at 77 K	f
2·0018 2·0013 1·9998		E'_{α}		
2·0018 2·0006 2·0003		E'_{γ}		
2·0018 2·0021 2·0021		E'_{δ}		
2·002		Bi-radical $S = 1$	$\lvert D \rvert / g\mu_B = 13{\cdot}4$ mT low OH	
·4		Triplet state ($S = 1$) defect	γ-irradiated O-deficient sample	g
2·0004 2·0030	$\parallel$: 68×10^{-4} cm^{-1} $\perp$: 40×10^{-4} cm^{-1}	$G6$ centre	V_2^+	
2·0012 2·0142	79 50	$G7$	V_2^-	
[illegible]	[illegible]	$G16$	[illegible]	h

-value(s)	Hyperfine coupling constant*	Location and origin	Remarks	Ref.
2·0018 2·0006	424 362	E'	O-vacancy in a-SiO_2	
)·28–0·50		conduction electron	$m^*/m = 0·015$	i
2·04 ± 0·01	$(866 \pm 10) \times 10^{-4}$ cm^{-1}	As-related antisite defect		@
	$(890 \pm 10) \times 10^{-4}$ cm^{-1}	As Ga^0 EL2 centre		j
2·003	5·7 mT			
	| Fine structure | = 1·55 mT			
1·993			20 K	
2·046	–			
	| Fine structure | = 37·4 mT			i
2·106				
8·1		Bound hole detected by uniaxial stress		
6·7		Bound hole detected by uniaxial stress		
2·04	A/h = 2700 MHz	Antisite defect ^{75}As $^{75}As_4$	Hole configuration	k
2·0032(4)		Dangling bonds in disordered layer	$\Delta H \sim 0·6$ mT, $T = 77$ K N-implantation $\geq 5 \times 10^{15}$/cc ESR intensity is proportional to no. of defects produced by implantation	l
2·002	60·5 ($S = 5/2?$)			i
2·023	| Fine structure | = 42·9 mT			

g-value(s)	Hyperfine coupling constant*	Location and origin	Remarks	Ref.
	SHF ^{31}P: $A_{\parallel}/h = 314$ MHz	$^{31}P^{31}P_4$	p-GaP	
	$A_{\perp}/h = 179$ MHz			
2·013	SHF $A_{\parallel}/h = 310$ MHz	Isolated Ga vacancy		
	$A_{\perp}/h = 124$ MHz			
2·089	SHF $A_{\parallel}/h = 112$ MHz		35 GHz, 20 K	
	$A_{\perp}/h = 55$ MHz		SHF by ENDOR at ~ 4 K	
-0·934				
l: 1·974	$\lvert$Fine structure$\rvert = 0{\cdot}031$ cm^{-1}			
.: 1·997	$D = -1{\cdot}860$ cm^{-1}			
1·999				
1·986		Cr^{4+} ?		
50·7–48·8		Conduction electrons	g-values, linewidth conc. dependent	i
3 line spectrum		Fe^{3+} in cubic symmetry	$T = 10$ K, $\Delta H \approx 12$ mT	n

Iz and cm^{-1}. 1 mT = 10 gauss = 28·02 MHz = $9{\cdot}346 \times 10^{-4}$ cm^{-1}.
expressed as $A/g\mu_B$ (cm^{-1}) in spectroscopy.
tructure.

Rev. **90** 988
D K 1988 *Amorphous silicon and related materials* (ed.) H Fritzsche (Singapore: World Scientific) p. 557
Conf. Series No 59 p. 81
n. Solids **24** 1467
us Solidi **B86** 269
J 1986 *Phys. Rev.* **B34** 7524
Rev. **B41** 7158
s. Lett. **50** 1450
ctors and semimetals (New York: Academic) Vol. 2, Chap 8
Res. Soc. Symp. Proc. Vol. 241, p. 69
Commun. **36** 15

ccordingly the ESR spectrum changes from a 2-line (I = 1/2) hyperfine pattern to a g-shifted and broadened attern as P concentration is increased (Slichter 1971).

Three general conclusions emerge from these studies n doped Si:

(I) The hydrogen-like energy states available to an olated impurity atom provide a set of localized atomic ates capable of producing deep levels in the band gap f the semiconducting host.

(II) The interaction of the atomic states of an impurity t an interstitial site with the host bunches these deep vels and confines them within the gap. Thus the terstitial site 'attracts' deep levels.

(III) The substitutional site, however, 'rejects' deep vels, and is thus not favoured.

Local interatomic distances between Si and an s–p onded impurity can be very accurately determined using PR hyperfine structure from magnetic ligands as has een demonstrated by Scheffler (1987) for the case of $^+$ in Si. Comparing the ratio of the experimentally etermined Fermi contact parameter and the dipole arameter (b) to the same ratios calculated as a function f local geometry (i.e. different S–Si bond lengths), the quilibrium geometry of the Si–S complex is established. he S–Si bond length thus determined is 2·345 Å, ractically identical with the 2·35 Å determined from xtended X-ray absorption fine structure (EXAFS) easurements.

The role of the interstitial hydrogen impurity in semi-onductors (especially Si) as a passivator of deep and hallow can never be over-emphasized. It is the most ndamental and one of the most challenging issues in e materials science of silicon. Hydrogen can diffuse rough Si rapidly at room temperature (unlike in metals here they can be stored). While it causes embrittlement f Si at low temperatures, it aids dislocation motion in i at high temperatures. It can exist in Si as a centre ith positive (H^+), neutral (H^0) and negative (H^-) states Myers *et al* 1992). EPR of the apparently isolated eutral hydrogen (H^0) has been observed (Gorelkinskii nd Nevinnyi 1987a, b) for Si after proton irradiation at 0 K. Two paramagnetic centres AA9 and AA10 — both ositively charged — have been identified. AA9 shows yperfine splitting due to H atoms. Both centres anneal 180 K.

Silver — an important 4d transition metal impurity in

stitial position and Ag in a substitutional posit 17), and (iii) an Ag-transition metal pair.

In briefly annealed (250°C, 15 min) Si sin samples implanted with 30 MeV hydrogen and (to ~ $10^{17}/cm^2$) an EPR spectrum attributed to a molecule oriented along ⟨111⟩ direction in the has been detected, in experiments performed K-band frequencies, at liquid He temperatures *et al* 1993). The hyperfine structure of H reduced at K-band as a triplet and a singlet a L52' spectrum is described by the spin Ham

$$\mathcal{H}=\mu_B H\cdot g\cdot S+S\cdot A_{H_2}\cdot H_{H_2}+S\cdot A_{H^1}\cdot I_{H^1}+S$$

where $S=1/2, I_{H2}=1$ for the triplet spec $I_{H2}=0$ for the singlet spectrum and $I_{H'}=t_{H}$. F the orthohydrogen molecule, while H^1 and H^2 hydrogens. The g and A parameters are includ 8. The capture of mobile H^- at the interstitia H^0 is proposed as the probable mechanism of of H_2.

The nonobservation of Au^0 in semiconducti EPR had been as intriguing as the nonobse Cu^{++} EPR in high T_c superconductors (M Anderson 1988). But from Zeeman effect 1·9 K, Watkins *et al* (1991) have established the single donor and the single acceptor leve in Si arise from isolated substitutional neutra ground state is paramagnetic $S=1/2$ and is t distorted with $g_{\parallel}\simeq 2{\cdot}8$ and $g_{\perp}\approx 0$, unlike the is Pt^-, for which $S=1/2, g_{\parallel}\simeq 2{\cdot}1$ and $g_{\perp}=1{\cdot}4$. T of Au^0 EPR in Si is thus a direct conse $g_{\perp}=0$, which implies that M_s values for the gr quantize along the defect tetragonal axis inde the orientation of the magnetic field. Thus th magnetic field dependent off-diagonal terms i Hamiltonian, and no $\Delta M_s=\pm 1$ transition induced by a microwave field.

An interesting EPR and ENDOR study by *et al* (1987) of interstitial Cr^+ centres in Si, to illustrate the application of the latter, as demonstrate the success of the model dev Ludwig and Woodbury (1962) to account for th effective spin and g-values of the 3d-transi impurity in Si. According to their model, the in

existence of a donor level in $Cr_i^{0/+}$ was established, from EPR to be 0·22 eV below the conduction level. Intriguingly, the observed hyperfine interaction between 3d electrons and the impurity nucleus is smaller than that

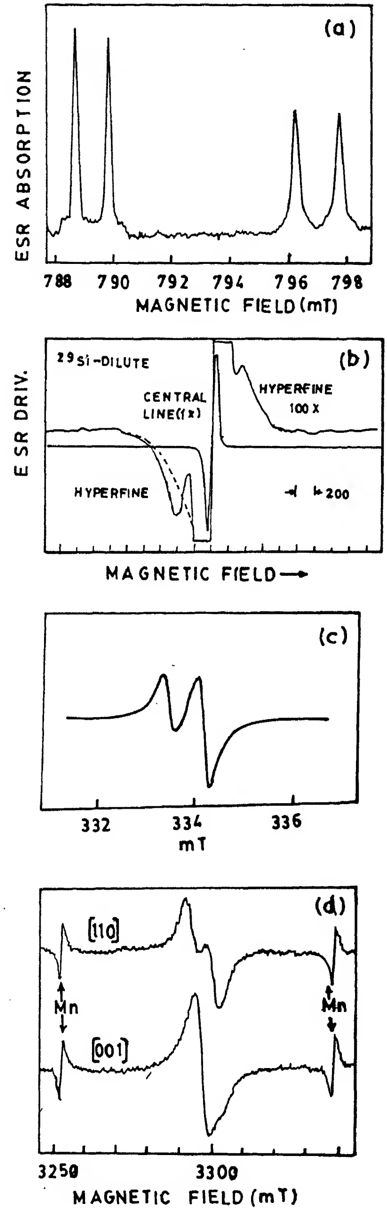

Figure 17. Typical ESR spectra of transition metal impurities and structural defects in different types of silicon. **a.** Spectrum

calculated for the free Cr_i^+ ion w
rather large delocalization of the
leading to a large hyperfine inte
ligands. But these interactions were
(figure 19a). ENDOR experiments
19b), that in Si : Cr_i^+, the impurity e
one hundred and two (102) Si at
shells surrounding the Cr impurity.
that emerges from this study is th
density is transferred from the i
crystal. This has resolved the cont
52% delocalization of the impurity
out on the basis of EPR data,
hyperfine interaction due to Si lig

8.2b *Deformed and implanted Si*:
Si gives rich EPR spectra due to
vacancy type, produced during de
those induced by radiation damag
the dangling bond type — almost a
$g_\perp - g_e > 0$ and $g_\parallel \approx g_e$. These centres
graphically equivalent orientation
intensity (Webb and Alexander 19

Ion implantation, an important
fabrication, is a process in which
^{75}As or ^{76}As) are introduced in,
substrate, and, occur at relatively l
as room temperature substrate. He
ion implantation leads to the for
layers in semiconductors (Masuda
annealed at low temperatures. It is

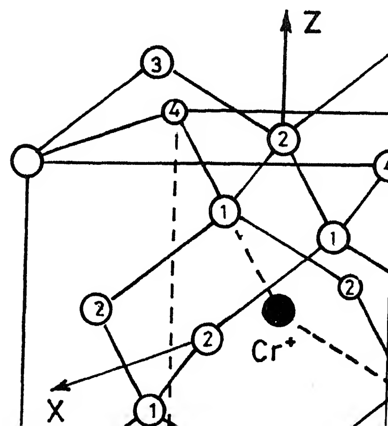

pic Lorentzian-shaped ESR signal with $g = 2{\cdot}006$ $\Delta H_{max \cdot slope} = 0{\cdot}48$–$0{\cdot}6$ mT which when annealed at 0°C yields the ideal amorphous state. Annealing d 500–550°C produces ESR due to conduction ons with $g = 1{\cdot}998$–$1{\cdot}999$ and complete recovery of harge carriers. The important result is that the ure of voids in the amorphous layer produced by -ion implantation has inhomogeneous characteristics the void, in contrast to that in clean surfaces ed in ultra-high vacuum.

heavily P-doped (7×10^{17} atoms/cm^3) Si, upon eV electron irradiation at room temperature, two-horus defect complexes are detected in EPR erts and Ammerlaan 1977) whose formation is ned by a slow diffusion of the phosphorus-vacancy or E centres during irradiation at 60°C and sub-nt trapping by other phosphorus atoms. An tion-induced diffusion mechanism is found to be ial for this process.

Amorphous silicon (a–Si) and hydrogenated phous silicon (a–Si : H): The main difference en crystalline and amorphous silicon is that in the the edges of the valence and conduction bands are what ill defined, so that the 'tails' of these two consist of states that exhibit a certain degree of zation. Thus these 'localized states' occur in the gap and give rise to characteristic EPR signals, ted to point defects.

most widely investigated centre in undoped *a*–Si –Si : H) is the so-called D centre due to Si dangling bonds, which are actually unbonded orbitals on coordinated (instead of the usual 4-coordinated) silicon atom (Si_3^0) in the disordered network. Due t of bonding partners, the fourth atomic sp^3 hyb unbonded and thus the electronic defect is 'dangling band', analogous to similar defect states surfaces/grain boundaries of crystalline silicon fingerprint of this electronic defect, which, in un *a*–Si : H essentially determines the lifetime of charge carriers and thus limits the performan *a*–Si : H thin films for many applications, is a c teristic ESR signal with $g = 2{\cdot}0055$ whose intensit convenient measure of the quality of a given specimen.

The attempts to describe the macroscopic pro of device grade *a*–Si : H within the framework of un microscopic structural models namely, (i) the ne correlation energy (U) model U being the effective required to place a second electron in a singly oc defect level, (ii) the thermal equilibration model an the dangling-band conversion model all of whic on the hypothesis that the dominant structural de *a*–Si : H is definitely the Si dangling bond.

Pantelides (1988) has proposed a floating bond in which 'floating bond' is likely to be more than the dangling bond. He argues that a mob centre is essential in accounting for the divers fascinating phenomena observed in *a*–Si. The crys analog of a floating band is an Si interstitial, whi of a dangling bond is a Si vacancy. The floating $Si^0_{(5)}$ is an over-coordinated Si atom as much

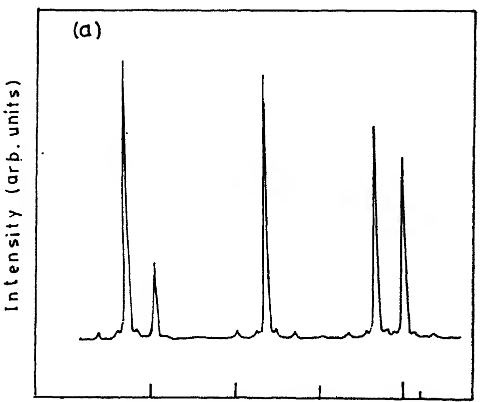

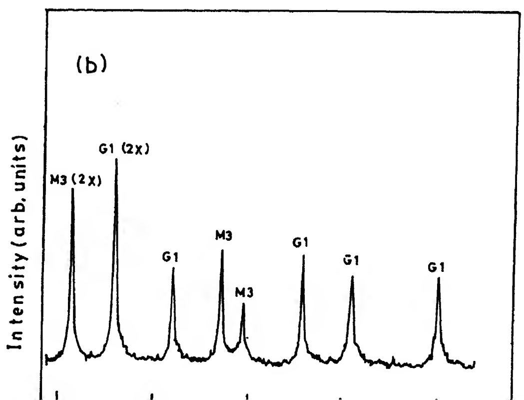

dangling bond $Si^0_{(3)}$ is an under-coordinated Si atom, and is characterized by a molecular orbital vis-a-vis the atomic orbital (Si–Sp^3) of the dangling bond. The advantage with the floating bond is that 'bond switching' rather than 'bond breaking' results in high mobility needed for electrical transport. Self annihilation of the bond is possible and a 'kick-out' mechanism of diffusion of hydrogen is postulated wherein the stationary Si–H bond is attacked by the mobile migrating floating bond, releasing or 'kicking out' a H into an interstitial. In this picture, the doping phenomenon in a semiconductor is conceived as a change in the coordination mediated by a mobile intrinsic defect, without the need for any electronic transition. Thus a 3-coordinated P defect would combine with a floating bond to yield a P_4. P_4^0 or the neutral donor observed in the EPR, if P-doped *a*–Si : H and *a*–Ge : H through well resolved ^{31}P and ^{75}As hyperfine structures provides some support for the floating bond model, although the question whether D-centres are mobile, still needs to be answered comprehensively. This pioneering ESR study of Stutzmann and Street (1985) has shown further that disorder-induced localization of states in *a*–Si : H makes the donor hyperfine structure (^{31}P or ^{75}As) greater than that in crystalline Si and broadens the distribution of states with similar electronic character.

The observation by Stutzmann and Biegelsen (1989) of hyperfine structure ^{29}Si of the $g = 2{\cdot}0055$ ESR in undoped *a*–Si : H containing the natural abundance of the ^{29}Si isotope (figure 17b, table 8) has allowed quantitative modelling of the underlying hyperfine and *g*-tensors. The structural parameters deduced for the $g = 2{\cdot}0055$ defect agrees very well with those of Si dangling bonds at the Si/SiO_2 interface. Significantly the ^{29}Si hyperfine structure observed by Stutzmann and Biegelsen (1989) appears to be incompatible with the floating bond model because the floating bond wave function would leave a much less weight on any Si atom than a dangling bond state.

ENDOR studies of *a*–Si : H (made by reactive sputtering (RS) and glow-discharge (GD) decomposition) have shown (Yokomichi and Morigaki 1987; Morigaki 1988) the existence of at least two different types of dangling bonds: (i) normal dangling bonds and (ii) dangling bonds having a hydrogen as their neighbour. These experiments carried out at 7 K, 9·0 GHz and rf current in the 1–150 mA

constant of 6 MHz was deduced.
sities estimated from ESR meas
and $1{\cdot}6\times10^{18}$ cm^{-3} for GD and
exposure (~ 5 h) of Gd sample
from Xenon lamp increased the
to $1{\cdot}8\times10^{18}$/cc.

There is a recent ENDOR
dangling bonds (Yokomichi and M
of a rather large hyperfine splitt
^{29}Si in unannealed and anneale
70°C by glow discharge. This
bond is more delocalized and ha
those of isolated, normal danglin

8.2d *Porous silicon*: Crystallin
band gap material, unlike the lig
is a direct band gap material. F
the result of efforts to 'enginee
Si so that it could emit light like
prepared this material by etchin
pores into a Si wafer by applying
process is accelerated by a smal
wafer. It is possible to etch aw
leaving an array of tiny 'dots'
'quantum dots'. ESR studies on
electrochemical anodization of Si
(Kubo *et al* 1992; Yokomichi *e*
that the main defect in porous s
bond located at the surface or at
It has trigonal symmetry with a
⟨111⟩ axis, with $g_{\parallel} = 2{\cdot}0022$
anisotropy of the defect implies
retains the crystallinity of the sub
Xe arc lamp light increases the
which are partially recovered on t
17d), unlike in *a*–Si : H. This ob
the light-emitting region of *p*–Si
crystal phase. This study has op
applied lines of investigation inc
of hyperfine interaction, to be c
and *a*–Si : H as well as light-em
both photo and electroluminescen

8.3 *Germanium*

In contrast to the extensively s

$$\mu_{\text{eff}} = \mu_B \left[1 - \frac{\left(\frac{m_0}{m^*} - 1\right)\Delta}{3E_g + \Delta} \right], \tag{63}$$

where μ_B is the Bohr magneton, Δ the spin–orbit interaction and E_g the band gap and the g-values are very much different from 2. Indeed, g — which depends on concentration of electrons in the conduction band — is too low for GaAs (0·28–0·56) while it is too high (50·7–48·8) for InSb. In the latter compound, the ESR line broadens with increasing electron concentration.

High-dose ion implantation of GaP crystals by 200 KeV nitrogen ions at room temperature produces highly disordered layers therein, and, dangling bonds created thereby give an isotropic, 0·6 mT wide symmetric Lorentzian ESR with $g = 2{\cdot}0032 \pm 0{\cdot}0004$. This is apparently a very sensitive nondestructive method to determine the nature of damage produced by ion implantation, particularly because (i) the density of dangling bonds is proportional to the amount of disorder and (ii) the ESR spectral intensity is proportional to the number of defects produced by implantation.

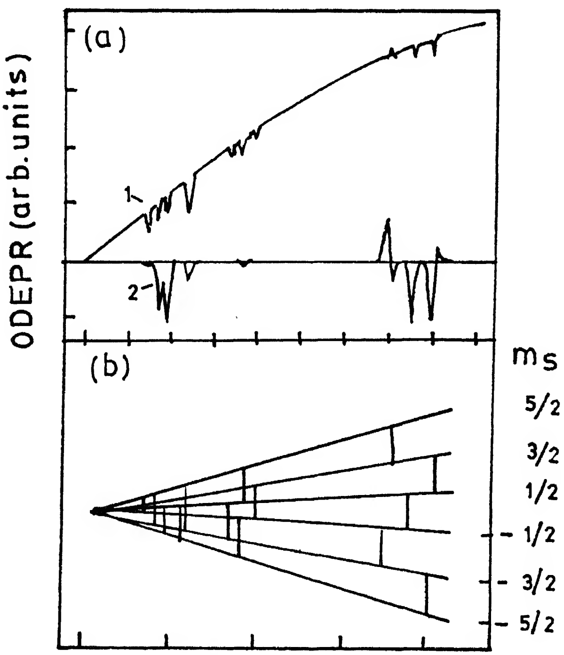

Fe^{3+} defect in InP — a material
optical devices — has been inv
optically detected EPR (ODEPR)
This paramagnetic ($S = 5/2$ $3d^5$
acceptor — makes InP a sem
Although ODEPR and EPR give
the same five fine-structure split
$g = 2{\cdot}024$ and a, and the cubic
MHz and the lowest field fine st
opposite sign compared to others
in the ODEPR spectra of Fe^{3+} in
behaviour arises from spin–lattice
Zeeman levels which operate
($\Delta M_s = \pm 2$) transitions than for al
sitions. The spin–lattice relaxat
transitions are 0·9 ms and 2·6 ms

Semi-insulating, undoped GaAs
by low temperature (200°C) mol
GaAs or Si substrates have been
devices, photoconductive devices
as buffer layer in GaAs FETs
layer in MOSFETs. This material
layer of $Ga_{0{\cdot}495}As_{0{\cdot}505}$, gives
EPR spectrum (Von Bardelebe
$g = 2{\cdot}04 \pm 0{\cdot}01$ and $A(866 \pm 10) \times$
with $A = (890 \pm 10) \times 10^{-4}\,\text{cm}^{-1}$ o
EL2-related antisite defects. Th
with thermal annealing. The lowe
to a change in the configuration
defects, which occur in both Czo
grown GaAs, and in amorphous-
be formed by electron irradiation
A values, fingerprints for specifi

8.5b *II–IV compounds*: Among
CdTe is well investigated for E
shallow and deep donors. Howeve
by implantation with B ions are
al 1987) in the fabrication of in
EPR spectra of $Hg_{0{\cdot}7}Cd_{0{\cdot}3}Te$ an
detected at < 78 K are sharp an
doses of $\geq 1{\times}10^{16}\,\text{mg/cm}^2$. For i
tions, $Hg_{0{\cdot}7}Cd_{0{\cdot}3}Te$ gives near-inte
than CdTe. Generally, the g-fact
sitions are identical and correspo

novel technique (Rodriguez 1987) called electric spin resonance has been applied to study spin–orbit ing strength in the conduction band of zinc blende vurtzite semiconductors — InSb and $Cd_{1-x}Mn_xSe$ in ular. A parity violating spin–orbit coupling mixes with opposite spin orientations and parities. This g allows electric dipole transitions between states , in the absence of spin–orbit coupling, have equal and opposite spins. This interaction is given by

$$\cdot H = 1/2\, g_0 \mu_B \sqrt{\varepsilon}\, \mathcal{E}\, (\hat{n} \times \hat{\varepsilon}) \cdot \sigma,$$

g_0 is the g factor of electrons for small fields the εE, electric field of the wave, ε the dielectric ant of the material and σ the Pauli spin matrix. InSb, $g_H - g_1 = -0.428$ where g_1 is the orbital g-factor which agrees very well with the theoretical va -0.42.

8.6 *Synthetic diamond*

Synthetic diamond (carbon) ($\geq 1.0\,\mathrm{cm}^3$) single c grown at a high temperature and under high pr has application in electronic devices. Diamond, lies directly above silicon in the periodic tab isostructural with silicon. But unlike Si, it can only Ni among the 3d-group metals, which gi ESR line at $g = 2.0310 \pm 0.0005$ in polycrystalline grown from a metal melt containing Ni (Loubs Van Ryneweld 1966). This signal is isotropic do 4 K, suggesting a high symmetry site for Ni diamond lattice without any charge compensation

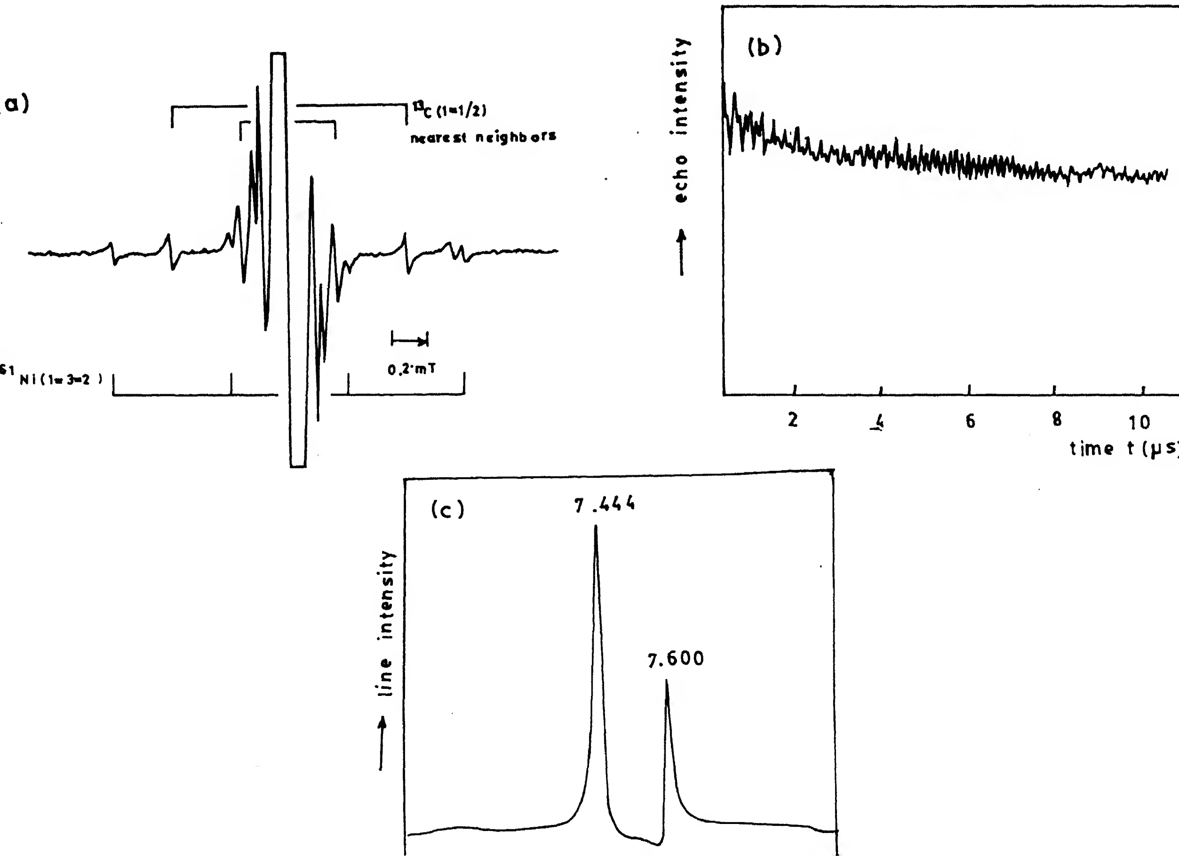

A comprehensive pulsed, Fourier transform and continuous wave (CW) EPR study has been carried out (Isoya *et al* 1990) on the Ni impurity in synthetic diamond, characterized by the $g = 2{\cdot}0319$ signal, whose linewidth is temperature dependent above 150 K due to strong spin–lattice relaxation. Figure 21 shows the CW spectrum, three-pulse echo modulation (In the 3-pulse echo technique, unlike in the 2-pulse spin echo technique discussed earlier, a third pulse applied whose distance from the first pulse is varied while the distance between first and second is fixed), and frequency domain spectrum for Ni. CW spectra (at 77 K) give an isotropic hyperfine splitting A (^{61}Ni, $I = 3/2$) of 0·65 mT and two sets of nearly isotropic splittings due to hyperfine interaction with nearest and next-nearest neighbours ^{13}C atoms (the substitutional site in diamond has 12 'next-nearest' neighbours whereas the interstitial site has only six next-nearest neighbours). The CW EPR fails to resolve all the sets of super hyperfine lines due to interaction of unpaired electron of Ni with ^{13}C nuclei, which produce a 'modulation' of the spin echo which is detected in the time-domain. Accurate measurement of the super hyperfine coupling constant is possible for recording the frequency domain spectrum in an experiment akin to ENDOR. The effective spin of Ni has been determined to be $S = 3/2$ (i.e. Ni is in -1 state at a substitutional site of tetragonal symmetry) 3d^7 from (i) the nutation of the magnetization by the microwave magnetic field (H_1) and (ii) ^{13}C nuclear frequencies. This pioneering study has opened up new possibilities for the characterization of synthetic diamonds.

In a recent study, the ESR of diamond-like nuclei produced in a Si surface layer by high-dose C-ion doping has been measured (Izumi *et al* 1993).

The distribution of substitutional nitrogen centres (with resolved hyperfine structural from ^{14}N) and Ni impurities has been determined by ESR imaging (Furusawa and Ikeya 1990) (see § 12).

9. Polymeric materials

9.1 *General considerations*

Polymers have been extensively investigated from the points of view of local structural confirmation, degrada-

to the propagation of one kineti
free radical chain reaction requi
step in which a radical specie
reaction mixture. Two processes

(1) Homolytic cleavage

$$AB \xrightarrow{+h\nu} A + B.$$

(2) Unpaired electron transfer fro
mer fragments formed by dissoc

$$R\text{–}R \xrightarrow{+h\nu} 2R.$$

$$R. + CH_2 = CHX \rightarrow R\text{–}CH_2 -$$

where R is an alkyl group and
dots denote unpaired electrons.

An example of an ESR study
the tunneling of methyl groups
formed by γ-irradiation of pol
(Iwasaki *et al* 1971). Other ra
include $CH_3OOC^{\cdot}$ or $HOOC^{\cdot}$
$OHC^{\cdot}$ which gives a doublet (s
course $^{\cdot}CH_3$ which gives a qu
ratio 1 : 3 : 3 : 1 and a spacing
interaction of unpaired spin wi
nuclei. Generally the ESR spectru
to irradiation may be characteriz

$$H_{res} = \frac{h\nu}{g\beta} - \sum_{i=1}^{\infty} (A_i + B_i)\, m I_i\,,$$

where A_i is the isotropic hyperf
the radical and nucleus i, and,
of this interaction depending on
radical. The singlet ESR referred
$A = B = 0$. For most hydrocarbon
α-protons i.e. H nuclei directly
atom. In highly-oriented polymers
mers these radicals have a strongl
hyperfine structure. In general, f
a spectrum with $(n + 1)$ lines w
the coefficients of binomial
observed. Thus for $^{\cdot}CH_3$ $(n = 3)$,

Highly-oriented polyethylene

protons have different hyperfine splittings so that ntet of lines due to four equivalent β protons, with quintet split into a doublet by the α proton are ved. The intensity ratio of the overall spectrum is 4 : 4 : 6 : 6 : 4 : 4 : 1 : 1. The primary radicals pro- by irradiation or milling are usually detected at emperatures in most of the common degraded ners. Table 9 presents the radicals thus produced lected polymers. An exhaustive list is given by h (1978). ESR affords a direct study of bond e (and formation of 'mechano radicals') in highly ed fibres and films of polyethylene, propylene, , PMMA, polystyrene, polyesters and poly- ptides. The fracture of rubber has also been studied y and Rabek 1977). Free radicals formed and d in polymer matrices under certain conditions can e graft polymerization. The grafting reaction ds on (i) the physical state of the polymer, and e properties of free radicals formed in the polymer. mple of electron or γ-irradiated polymer brought ontact with a monomer can diffuse into the polymer and thus reach the trapped radical site. The case tadiene diffusion in polyvinyl chloride has been d (Hamanone *et al* 1974). The use of a 'dynamic probe' (e.g. the nitroxide O=N–O. dissolved in ne) has helped probe glass transition behaviour of ners, chain motions on the surfaces of as-grown nnealed polyethylene single crystals in relation to e structure, and polymer–plasticizer interaction in cized PVC. Among other ESR applications are the –acceptor polymer complexes and the reinforcing rties of carbon black in rubber vulcanization.

Recent applications include studies of (i) rad induced cross linking of polyethylene in the prese acetylene, (ii) molecular motion of chain-end r of polyethylene molecules anchored on fresh surfa polyethylene and PTFE, (iii) interaction of mechan generated polypropylene radicals with phenolic oxidant in the presence of oxygen, (iv) ther generated free radicals in PMR-15 polyimide resi solitons and phase transitions in conducting pol and (vi) photo-induced charge transfer from poly C_{60} superconductor.

Some of these applications are discussed in below.

9.2 *Mechano-radicals*

9.2a *Polymerization*: Mechano-radicals are pro by mechanical fracture (e.g. grinding) of polym low temperatures. The radicals known as chain-en free-radicals are produced by the 'homolytic scission' of carbon–carbon bond in the polymer chain. For e.g. a polymer P with a P–P bond und the scission:

$$P - P \rightarrow P^{*},$$

to yield the mechano-radical P^{*}. In addition, 'me anions' produced by heterolytic bond scission

$$P - P \rightarrow \underset{\text{mechano anion}}{P^{-}} + \underset{\text{mechano cation}}{P^{+}},$$

Table 9. Primary radicals in certain degraded polymers detected by ESR*†.

Polymer	Experimental conditions	Radical(s) found
1. Polyethylene	Milling (77, 240 K)	$-CH_2-\dot{C}H_2$
2. Polypropylene	Milling	$-CH_2-CH_3\dot{C}H$
3. Polystyrene	Milling (77 K)	$-CH_2-C_6H_5\dot{C}H$
4. PTFE	Ball mill	$-CF_2-\dot{C}F_2$
5. Polyvinyl alcohol	Grinding (80–170 K)	$CH_2-OH\dot{C}H$; $-OHCH-\dot{C}H_2$

can be stabilized for instance by electron transfer due to contact in the dark e.g.

$$P^{-} + M \rightarrow P^{*} + M^{\bullet -}, \tag{70}$$

(where M = a molecule with high electron affinity like tetracyano ethylene TCNE) so that P^{*} may be detected by ESR spectroscopy. It is significant that these mechano radicals initiate polymerization at low temperatures under vacuum, as has been demonstrated for methyl methacrylate and ethylene (Sakaguchi *et al* 1989).

Polyvinylidenefluoride (PVDF) fractured alone and with isobutyl vinyl ether (IBVE) as well as TCNE (Sakaguchi *et al* 1988, 1989) by using a vibration ball mill (in the dark and at 77 K under vacuum) to produce dramatic changes in the ESR spectra (figure 22) show that (i) mechanical fracture of TVDF alone induces a heterocyclic bond scission in the main chain,

$$\mathrm{PVDF} \rightarrow \underset{\mathrm{I}}{-\mathrm{CH}_2^{+}} + \underset{\mathrm{II}}{{}^{-}\mathrm{CF}_2^{-}-}, \tag{71}$$

producing mechano cation $-\mathrm{CH}_2^{+}$ and (ii) a cationic polymerization of IBVE is initiated by this mechano cation

$$-\mathrm{CH}_2^{+} + \mathrm{CH}_2{=}\mathrm{CH}(\mathrm{OCH}_2\mathrm{CH}(\mathrm{CH}_3)_2) \rightarrow$$
$$-\mathrm{CH}_2^{\bullet} + {}^{\bullet}\mathrm{CH}{-}{}^{+}\mathrm{CH}(\mathrm{OCH}_2\mathrm{CH}(\mathrm{CH}_3)_2), \tag{72}$$

eventually producing the PVIBE homopolymer through the propagation reaction.

$${}^{\bullet}\mathrm{CH}_2{-}{}^{+}\mathrm{CH}(\mathrm{OCH}_2\mathrm{CH}(\mathrm{CH}_3)_2) \rightarrow$$
$$\underset{\mathrm{III}}{\mathrm{CH}_2^{-} - {}^{+}\mathrm{CH} - {}^{+}\mathrm{CH}(\mathrm{OCH}_2\mathrm{CH}(\mathrm{CH}_3)_2).} \tag{73}$$

A superposition of the spectra of radicals I, II and III is seen in the ESR spectra (not formed by the abstraction of el the anion that is produced by scission of C–C bonds in the the following reactions.

$$\mathrm{PVDF} \rightarrow 2\ \mathrm{R}^{\bullet},$$

$$\mathrm{PVDF} \rightarrow \mathrm{R}^{-} + \mathrm{R}^{+},$$

$$\mathrm{R}^{-} + \mathrm{TCNE} \rightarrow \mathrm{R}^{\bullet} + \mathrm{TCNE}^{-},$$

(iv) photo irradiation of a fractu

$$\mathrm{R}^{-} + \mathrm{TCNE} \xrightarrow{h\nu} \mathrm{R}^{\bullet} + \mathrm{TCNE}^{-}$$

and increase the yields of total r

9.2b *Radical motion*: Molecul chains seems to be restricted by of the chains with matrix mole and/or the intermolecular forces the matrix. The study of such looking — for instance — at the blends (Shimada *et al* 1988). S have made a comprehensive E radical motion of polyethylene ra surfaces of polyethylene (PE) and (PTFE). This radical, produced (under vacuum at 77 K), can in zation of ethylene monomer an chains which are bound to the m fresh surface of the polymer. The of this radical anchored on fresh even at 77 K because the wea between radical and PTFE mole to protrude from the PTFE surf isolated system. But the same ch

fresh surface of PE is held more strongly to the olecule and exchange motion takes place in this plated system at 77 K. These conclusions are based mputer simulations of observed sextet and quintet a of radical for the case of PE and PTFE surfaces tively. The simulation was done assuming Gaussian ape function and spin exchange rate.

Charge generation mechanism in polymers: -electricity in polymers arises when there is a er of charge between two insulating polymers or en a metal and a polymer when they are brought ontact and then separated. This phenomenon, which oplications in electrophotography and dry-ink elec- otography and is also the cause of troublesome electricity, is a century-old problem (Harper 1964). recent quantitative model of contact electrification ers (Duke and Fabysh 1978), it has been shown teady-state-exchanged charge resides in intrinsic ular ion states and the sign and order of magnitude asured contact charge exchange between polystyrene o-polymer of styrene and methyl methacrylate have correctly predicted.

ovel charge generation mechanism for the reaction chano anions and mechano radicals produced by nical fracture of a polymer main chain, based on studies has been reported in an attempt to deal triboelectricity as a phenomenon involving the nical fracture of a polymer chain on the friction e. By measuring the yield of the ESR active $^{\cdot -}$ produced under milling of PMMA, PP, PE, and PTFE with TCNE in the dark at 77 K, uchi *et al* (1990) have shown that (i) an electron er occurs from the mechano-anions to the mechano ls produced by mechanical fracture of polymer chains via friction: $A^- + B^* \rightarrow A^* + B^-$, where A are the two polymers involved, (ii) the sign of arge induced by friction can be estimated from ectron release potential of A and electron affinity and (iii) the triboelectric series exist: A – PP – PE – PVDF – PTFE, based on the reaction with TCNE, varying from high to low from left ht, a significant conclusion obtained. The ESR es of photo-irradiated with filtered infrared radiation, lentical to the triboelectric series of polymers ter 1962).

studies could also concentrate on (i) the nature active centres involved and (ii) the structure inclusion compounds. ESR could answer que regarding the host–guest and guest–guest interacti an intermediate level between the presence of mor and the polymer.

Sozzani *et al* (1986) have sought to establish t a comparative study of a number of homogeneous mers the structure of the propagating chain ends d from diene monomers, (butadiene, 1,3-pentadiene prene, 2,3-dimethyl betadiene, 2-methyl pentadier 2,4-hexadiene), the structure of the propagating ends derived from diene monomers, in particula prevailing direction of propagating monomer uni the strict relationship between the last and the pre monomer. During polymerization, ESR spectra attrib to allyl-type propagating radicals, e.g.

$$\begin{array}{ccccccccccccc} & & & & & & \beta & & \alpha & & \alpha & & \alpha \\ -\mathrm{CH} & = & \mathrm{CH} & - & \mathrm{CH_2} & - & \mathrm{CH_2} & - & \mathrm{CH} & = & \mathrm{CH} & - & \mathrm{CH_2} \\ 2' & & 3' & & 4' & & 1 & & 2 & & 3 & & 4 \end{array}$$

in polybutadiene, characterized by a 6-line spe spaced 1·4 mT, and an intensity ratio 1 : 5 : 10 (figure 23) were observed. Except for this radical polymer, all other radicals are stable over long p of time, in the range – 150° to + 60°C. Thus, the in methyl polybutalines are confirmationally fixed.

The ESR spectrum of allyl radical in polybut included in PHTP is temperature-dependent (figu and rotates around the C_1–C_2 bond even at roon perature, i.e. it is mobile even at ambient tempe The five α_1 and βH nuclei of the above radic coupled to the unpaired electron by about the constant, while the α_2 hydrogen is coupled to i much smaller coupling constant. The β–H consta given by

$$a_\beta = B^0 \rho_\pi \cos^2 \theta,$$

where θ is the angle between the p_z orbital axis allyl system and the projection of the C_1–H bo the plane perpendicular to the C_1–C_2 bond, B^0 constant (5·88 mT) and ρ the spin density on carbon (assumed 0·58 for the allyl radical). The

9.4 *Undoped and doped polyacetylene*

Ever since Shirakawa and Ikeda (1971) prepared polycrystalline polyacetylene, $(CH)_x$, a conjugated polymer, there has been an explosion of literature in the so-called 'synthetic metals', as the highly conducting, quasi one-dimensional polymeric materials are called. ESR has been a natural choice for the study of these systems in which intrinsic paramagnetic centres — to the extent of one spin per ~1500 carbon atoms — are present in *trans*-$(CH)_x$ with an order of magnitude less in *cis*-$(CH)_x$. While the spins are mobile in pure *trans*-$(CH)_x$, they are fixed in *cis*-rich-$(CH)_x$.

Undoped polyacetylene can be regarded as a Peierls-distorted linear chain (Rice 1979) involving π electrons at the half-filled band, with an energy of formation E_π and length l, which may be related to π-electron energy gap, 2Δ and bandwidth, W. Numerical values of E_π, Δ and W are calculated to be 0·4, 10 and 1 eV, respectively. Using a harmonic potential $1/2\,au^2$ ($u=$

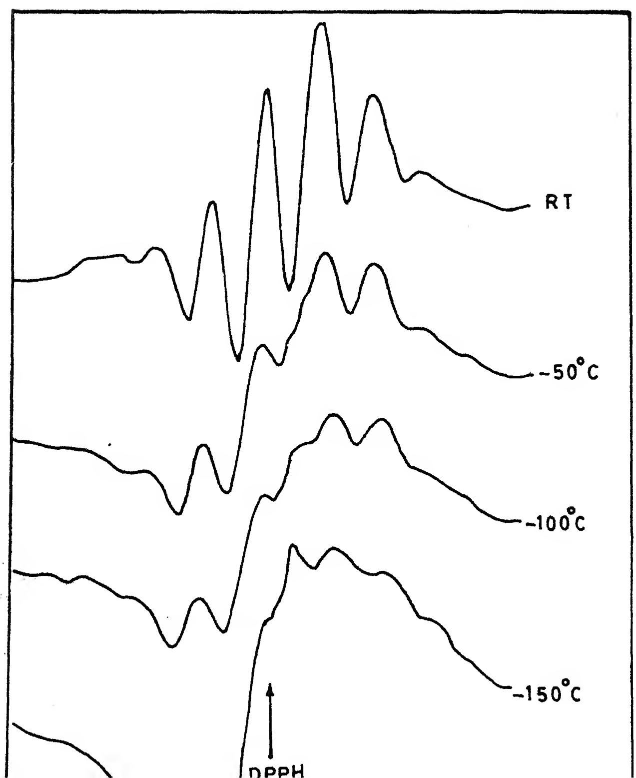

displacement) in which the elec
shown that $l/a \approx W/\Delta$ so that $l/$
is highly doped with electrons/ho
be accommodated in the form o
or soliton distortions rather than
tron band states. These distortion
of the polyacetylene chain gen
length l, a 180° variation in th
band alternation, separating e
change segment in which si
shifted by one C–C length. Th
charged domain walls. Thus, w
would represent the dilute limi
stored in the form of spinless c
doped (< 6 mol%) would create
which move to conduct electric
with alkali metals, AsF_5 etc.),
soliton to metal phase transition,
to be a first-order phase transi
studies of electrochemically Na
the ESR linewidth exhibits a
hysteresis, as functions of chem

A thorough analysis of the ESR
in undoped $(CH)_x$ (Holczer *et a*
al 1983), has established that
extremely sensitive to ambient co
not increase spin susceptibility)
on sample preparation. By taking
various stages of material prepara
a ΔH_{pp} of 0·044 mT, while a so
et al 1985) has yielded a very n
line. This narrow line, represe
dimensional) transport of mobil
whereas the fixed spins of *cis*-((
line considerably. The soliton ma
trapped to diffusive states, givin
line.

The first-order transition to th
acetylene, when it is heavily do
(Kivelson and Heeger 1985) in te
polymer model illustrated in fig

An abrupt crossover from a la
to a regular array of polaron-li
for this phase transition. In this
a 'dirty metal' in which there
gradual evolution of finite densit

e solid to give strong ESR signals. For instance, ning of nylon under vacuum, directly in the ESR , well-defined, structured spectra, similar to those ned upon γ-irradiation are obtained (Campbell and in 1968). In conducting polymers, such as 'new' cetylene (prepared by nonsolvent polymerization l with thermal treatment of catalyst solution at temperature), stretching (say by a factor of five) important means of increasing the probability of e carrier hopping and enhancing electrical conduc- by 5–6 orders of magnitude, because it is through ning that a parallel arrangement of polyacetylene is achieved. The basic question in conducting er research is: What molecular and morphological ure produces a high conductivity (~ 10^5 S cm^{-1}) upon g? In highly oriented polymers the ESR linewidth a dependence on the angle Θ between the direction entation of the polymer chains in the sample and c magnetic field of the ESR spectrometer. Thus, gree of stretching is easily correlated with molecular ty of the polyacetylene chain (Bartl *et al* 1993). egree of stretching $d_s = l/l_0 (l$ = length after stretch- $_0$ = initial length) while the ESR linewidth-related ter $\delta = (\Delta H_{\parallel} \cdot \Delta H_{\perp})/\Delta H_{\parallel}$ ($\Delta H_{\parallel}$ and $\Delta H_{\perp}$ are linewidth =0 and 90°, respectively), while d_s changes from , δ varies from 0·22 to 0·34. δ increases drastically degree of stretching, while at high orientation, ws a small effect. These behaviours correlate with crease of electrical conductivity as a function of ning.

'probes' for these studies, of structural and ori- nal aspects are the so-called neutral solitons which ramagnetic species with spin but without charge *et al* 1992). The mobile spins move along the gated chain segments obtained by 'doping' to pro- motionally narrowed ESR lines through exchange tion of electron spins with proton spins. Thus the of the undisturbed conjugate chain segments ines the ESR linewidth. Short segments show ESR lines while long segments produce narrow ines. As already stated, ESR linewidth shows a teristic dependence with respect to the orientation polymer chain relative to the magnetic field.

Polymer–fullerene charge transfer

carbon superconductor or Buckminsterfullerene (C_6 been investigated (Sariffici 1992). In this light-in ESR or LESR experiment, ion radicals originating charge separation

$$D + A \rightarrow D^{+\bullet} + A^{-\bullet},$$

where D is the electron donor (MEH–PPV) and electron acceptor (C_{60}), are photo-generated and de *in situ*. Upon irradiation at 80 K with an argon–ion beam (2·14 eV : 150 mW) two photo-induced signa at $g \sim 2{\cdot}0000$ with $\Delta H_{pp} = 0{\cdot}72$ mT, and (ii) ~ 1·9955 with $\Delta H_{pp} = 0{\cdot}6$ mT, due to (MEH–PPV) C_{60}^{-} were observed (figure 25). At 80 K, the ESR intensity increases during light ON–OFF – ON cycles, indicating the accumulation of photo-gen spins associated with $D^{+\bullet}$ and $A^{-\bullet}$ species. At 200 LESR signal nearly vanishes, demonstrating reversibility of the process, ruling out any residua due to photo chemical reaction products. The pro applications of this prototypical reaction are in mol optoelectronics, nonlinear optics and photovoltaics

9.7 *Polymer imaging*

The fact that ESR signals can be enhanced and cont by adding dopants to polymers has been exploit

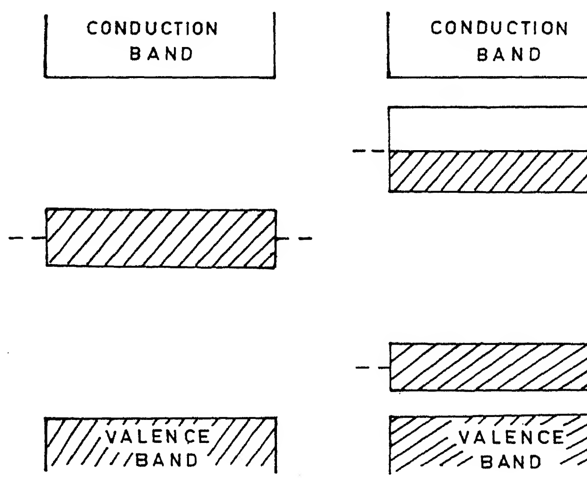

the nondestructive testing of polymer-based composite materials (Green 1990). When such materials are damaged by impact the existence and extent of damage cannot often be accessed and assessed by mere examination of the outer surface. However, by doping each layer of the polymer-based composite with a different dopant prior to lay-up, subsequent damage can be quantitatively determined as a function of depth into the composite by means of scanning EPR (figure 26). Thus both the spatial position of the dopant as well as its quantity are located (see § 12).

10. Glasses and ceramics

10.1 *Glasses*

Glasses form an expansive family of advanced materials which can be characterized by means of EPR. There are three groups of interest: (i) metallic glasses such as $Fe_{80}B_{20}$ and its ternary variants, which are soft amorphous ferromagnets (Bhagat 1973), (ii) semiconducting glasses such as V_2O_5–TeO_2 which are hopping ($V^{4+} \rightarrow V^{5+}$) electronic conductors or chalcogenide glasses (e.g. Se, As_2S_3) (Bishop *et al* 1977), and (iii) insulating glasses such as (a) soda-lime silicate glasses, containing paramagnetic impurities (e.g. Fe^{3+}) in trace quantities (Griscom 1980; Rao and Rao 1985) or else radiation induced paramagnetic centres (Griscom 1973/74), (b) soda-borate glasses of variable composition with a substitutional amount of a third component such as MoO_3 (up to 25 mol%), Mo^{4+} being an excellent sensor for the structure of borate glasses (Simon and Nicula 1983).

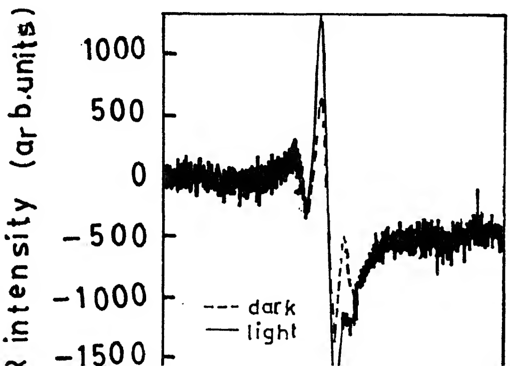

10.1.1 *Metallic glasses*

Metallic glasses are structurally c
obtained by rapid quenching of melt
as wires and ribbons. They are an
soft ferromagnetic materials that
formers in transformer cores. A f
crystalline or glassy, unlike a para
net nonzero internal magnetic field
spontaneous magnetization, (ii)
crystalline anisotropy, (iii) intrinsic s
(iv) extrinsic elastic stresses on the
effect. The presence of magnetostri
the orientation of the spontaneous m
dependent on the magnitude and dir
and external elastic stresses. From
of view, metallic glasses form a
strongly interacting electrons, comp
trostatic) interaction which gives rise
magnetic field mentioned above.
condition for ferromagnetic samples

$$\hbar\omega = g\,\mu_B H_{eff},$$

where H_{eff} is the effective field acti
magnetic moments and $\omega = 2\pi\nu$. Th
field and the intrinsic linewidth —
experimental quantities — depend o
greater extent. In fact

$$H_{eff} = H_{app} - H_{dem} + H_{ani},$$

where, H_{app} is the applied dc mag
demagnetizing field, a function of s

$$= 8\,M_s\ \cot^{-1}[(a^2+b^2+c^2)^{1/2}c/ab$$

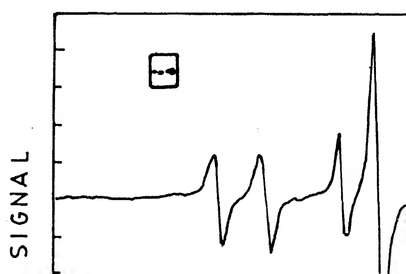

Using the intrinsic V^{4+} ($3d^1$) as the paramagnetic probe the ESR spectra of 55 mol% V_2O_5–45 mol% MO_2 (M = Ge, Se, Te) have been examined in the temperature range 298–498 K (Sunandana and Bhatnagar 1984). The three spectra at 298 K (figure 28) are characterized by a typical axially symmetric profile due to $3d^1$ ($S = 1/2$) electron interacting with a ^{51}V ($I = 7/2$) nucleus giving rise to a well-resolved (for M = Ge) to poorly-resolved (M = Se) pattern of 8 'parallel' and 8 'perpendicular'. The ESR parameters of selected semiconducting glasses are given in table 11. These differences are attributed to a monotonic increase in the covalency of the V–O bond on going from GeO_2 to TeO_2 to SeO_2. All the three compositions show dramatic but reversible temperature dependence by way of progressive broadening and eventual disappearance of the vanadium hyperfine

structure. This behaviour has bee
mally-activated delocalization of
leading to hopping V^{4+} electron
ening of the hyperfine structure
temperatures the hopping rate of
order as the hyperfine frequency

A comprehensive ESR investi
ternary glass system $(CuO)_x$ $(V_2O$
0·005, 0·01, 0·05, 0·1, 0·2 and (
conductivity measurements (Suna
has revealed that (i) addition
(0·5 mol%) of CuO has the effe
V^{5+} and thus suppressing the V^{4+}
conductivity, (ii) large concentratio
produces exchange effects of the
and g-shift of Cu^{++} ESR, with t

Table 10. Characteristic parameters for certain amorphous ferromagnetic materials determined from f

Material	T_c (K)	g	M_s (mT)	λ (10^8 s^{-1}) 300 K	77
$Fe_{90}Zr_{10}^{a}$	240 ± 1	2·07 ± 0·02	90 ± 1	5·18	–
$Fe_{91}Zr_{9}^{a}$	212 ± 1	2·07 ± 0·02	89 ± 1	5·07	–
$Co_{90}Zr_{10}$	00	2·09 ± 0·02	–	–	–
$Fe_{75-x}Ni_xB_{25}^{b}$					
$x = 35$	637 ± 10		76 ± 1	1·17(8)	1·3
$x = 45$	539 ± 10		72 ± 0·5	0·80(7)	0·9
$x = 55$	373 ± 10		51·5 ± 0·5	0·42(3)	0·7
$Fe_{83-y}Wy\ B_{17}^{b}$					
$y = 5$	450 ± 10		106·6 ± 0·4	1·28(20)	1·7
$y = 9$	354 ± 10			1·36(14)	2·4
$Fe_{20}Ni_{60}B_{20}^{c}$					
	93 GHz	420 ± 5	2·1	500·8	1·3
$(Fe_xNi_{1-x})_{75}P_{16}B_6Al_3^{d}$					
$x = 0·2$	92	–	26·3	–	–
$x = 0·25$	154	2·08	38·2	–	–
$x = 0·30$	221	2·08	43·0	–	–
$x = 0·35$	280	2·06	47·7	–	–
$x = 0·50$	440	2·08	66·0	–	–
$(Co_xNi_{1-x})_{75}P_{16}B_6Al_3^{d}$					
$x = 0·40$	88	–	15·0	–	

detectable at 289 K for a CuO content of 25 mol%. ...uctural model, showing probable path of hopping ...own in figure 29. While the hopping could be from ...to V^{5+}, the interactions between Cu^{2+} and V^{4+} ...d probably be mediated by $Cu^{2+}---O^{2-}---V^{4+}$ ...exchange mechanism.

... investigation of pseudobinary glass (0·5 MO) ... V_2O_5) (0·45 TeO_2), ($MO = TiO_2$, Cr_2O_3, MnO_2, ...$_3$ and Co_2O_3), with the 3d-transition metal ion par... substituting V-ion has shown (Sunandana 1987) ...while Ti^{3+}, Cr^{3+} and Co^{3+} modify the geometry of ...aramagnetic complex and thus control the electron ...ng process, introduction of Mn^{2+} and Fe^{3+} leads to ...tion of paramagnetic clusters.

...2b *Chalcogenide glasses*: ESR signals in pure ...ogenide glasses (Bishop *et al* 1977) are generally ...ved only upon optical excitation. The ground elec... states of these materials are invariably diamagnetic ...o spin pairing ($S = 0$). Amorphous Se, As and Ge ...ogenide glasses all exhibit a broad (≈ 50 mT wide) ...ance with $g = 2$ due to unpaired spin localized on

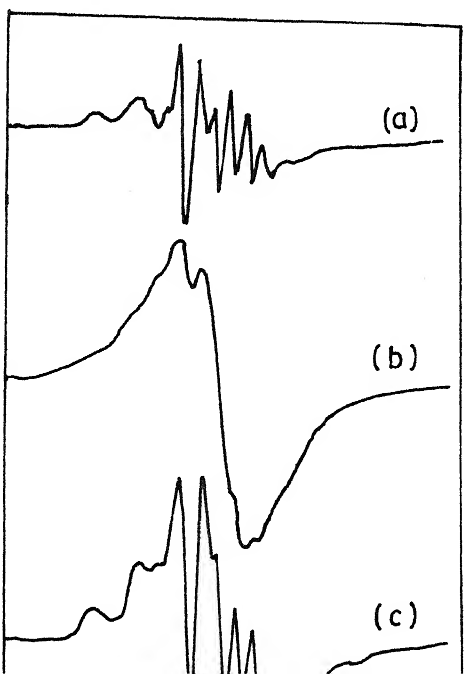

a single chalcogen atom. Amorphous As an... containing glasses exhibit an additional, much b... ($\Delta H \sim 150$ mT) resonance that could arise fro... unpaired electron localized on a predominantly ... orbital of As (reminescent of the P_4^0 centre in amor... Si), interacting with the ^{75}As ($I = 3/2$). This unre... hyperfine interaction could be resolved through ... ENDOR studies to obtain the exact neighbourho... this centre.

Structural imperfections or any deviation from ... random network structure or from chemically ... bonding expected from chemical composition in ... glasses play a significant role in their useful ele... and optical properties. These imperfections ... involve a pair of positively and negatively c... defects. Direct experimental evidence for the pr... of these defects help to understand their role ... context of their electrical and optical properties.

Kawazoe *et al* (1987) investigated, through E... the type of defects in chalcogenide liquids S and ... and As–Ge–S at a particular temperature, and (... manner in which these defects combine to form ... bonds during the cooling process. In liquid S, an ... Lorentzian, singlet homogeneously broadened ... absorption with $g = 2{\cdot}02$ is observed for temper... above 160°C, the temperatures at which S_8 ring mol... begin to break to form long linear chains. This ... is thus attributed to the formation of dangling bo... the liquid. The width of the line increases ma... with temperature due to a decrease in the life-ti... the radical. Likewise, liquid As_2S_3 gives a broad ... absorption at temperature greater than 360°C wi... lineshape changing from Lorentzian to Gaussian ... 500°C. The concentration of these broken bonds ... cooling the melts to form glass is determined ... chemical equilibrium between normal bonding ... (As–S), broken bonds (As and S) and homobonds (A... S–S). The concentration of these 'chain end ra... (somewhat like in fractured polymers) increases ma... reaching ~ 10 mol% at 700°C.

The enthalpy difference between normal bon... homobonds is usually small. Upon cooling the ... while the radical species disappear in the case of ... As–S, a fraction of the neutral defects or E' cen... ~ 2·01, $A \sim 24$ mT) remains in Ge–S, implying th... rate of ^{73}Ge recombination of radical species in ...

highlighted the crucial role of hierarchy of chemical bond strengths in determining the structure of glass forming chalcogenide liquids.

ESR studies on transition–metal–ion-doped Ge chalcogenide glasses have focused on aspects of local structure and bonding. In Ge_xSe_{1-x} ($0 \le x \le 0{\cdot}42$), containing 0·01 at.% Mn (Durny 1980), two characteristic resonances, one at $g = 4{\cdot}3$ with resolved hyperfine structure due to ^{55}Mn ($I = 5/2$) and the other at $g = 2{\cdot}0$ with hyperfine structure (A) rarely resolved are found. In this case $A = (51 \pm 5) \times 10^{-4}\ cm^{-1}$, which is correlated to the structure through the Hannay–Smith relation which relates the degree of covalency of the Mn complex (C) with the electronegativity difference between the Mn impurity and the chalcogen neighbours (L), $x_L - x_{Mn}$

$$C = 1 - 0{\cdot}16(x_L - x_{Mn}) - 0{\cdot}35(x_L - x_{Mn})^2. \tag{85}$$

To get the number of nearest neighbours around (n), Pauling covalency c/n is plotted against A. The above-mentioned A value is compatible with $n = 4$ so that Mn sites occupy Ge sites in the Ge–Se network with four Se neighbours. Mn^{++} in $Ge_{100-x}Sn$ ($x = 50$, 54, 58, 62, 66·7) gives rich ESR spectra (Watanabe *et al* 1978) with the composition $x = 58$ and 66·7 giving as many as four times at $g = 2{\cdot}0, 2{\cdot}8, 4{\cdot}3$ and 6·0, suggesting a large variety of internal electric fields of distinct symmetry in these glass compositions, while the $x = 50$ composition gives only the $g = 2{\cdot}0$ line, corresponding to Mn^{++}, in nearly cubic symmetry. The two other compositions $x = 54$ and 62 give two resonances at $g = 4{\cdot}3$ and $g = 2{\cdot}0$ with the latter exhibiting a hyperfine structure of magnitude $(65 \pm 5) \times 10^{-4}\ cm^{-1}$.

Ge_xSe_{1-x} ($23 \le x \le 44$) glasses containing 0·5 at.% Ti (Zhilinskaya *et al* 1991) give, when n lies between 32·5 and 41, a line with $g_{av} = 1{\cdot}982$, due to Ti^{3+} ($3d^1$) in a tetragonally-compressed octahedral environment. The concentration of this centre incre
For $x \le 33{\cdot}3$, an intrinsic paramag
I and I′ with principal g values 2
2·051, 2·025, 2·0036, correspondi
configurations of S in the Ge–S g
While doping with Ti or/and C
g-parameters, Ti doping decrease
affect the intensity depending on
Cu-doping decreases the concent

10.1.3 *Insulating glasses*

10.1.3a *Photochromic glasses*
glasses have the characteristic pro
of optical absorption. They are p
tation of Cu(I)-doped (0·01%) (Ag
halide microcrystals (~ 100 Å in
boro–silicate glass matrix. The p
due to photolysis of silver halide
akin to photographic latent ima
1992), is enhanced by Cu, a we
exists as optically inactive but
glass matrix and as optically a
Cu^+ in Ag-halide particles. The
the darkening mechanism are:

$$Ag^+ + Cl^- \xrightarrow{h\nu} Ag^0 + Cl^0,$$

$$Ag^+ + Cu^+ \xrightarrow{h\nu} Ag^+ + Cu^{++}.$$

The glass matrix does not allow
so that the darkening is reversi
absorption of colloidal silver (~
by Ag^0 aggregates on silver ha
darkening i.e. brown colouration
photoproducts are expected to e

Table 11. ESR parameters for V_2O_5–MO_2 glasses#.

Second component	$g_\parallel$ (±0·005)	$g_\perp$ (0·005)	$A_\parallel$ (mT ± 0·1)	$A_\perp$ (mT ± 0·1)
GeO_2 950°C	1·908	1·984	17·9	6·7
750°C	1·915	1·966	17·5	6·9
SeO_2	1·974	1·993	15·6 ± 1	7·5 ± 1
TeO_2	1·921	1·990	17·7	6·5
SrO	1·993	1·982	17·6	5·7

rquardt (1976) detected the ESR of photo-induced ions distributed among 16 distorted randomly-ted, approximately axial cation sites in the silver e phase. These Cu^{++} centres, resembling those in ed AgCl crystals doped with Cu^{++}, are characterized $_1 = 2{\cdot}05(2)$, $g_2 = 2{\cdot}11(5)$ and $g_3 = 2{\cdot}22(5)$, $A_1 \leq 2$ mT, $7{\cdot}8$ (0·5) mT and $A_3 = 9(0{\cdot}5)$ mT obtained by computer ation and are to be distinguished from matrix–glass- Cu^{2+}. A dual-cavity method together with micro- saturation of Cu^{++} was employed to enhance the ESR signal.

cent ESR studies (Caurant *et al* 1992) on photo-nic glasses containing 0·175 wt.% Ag, 0·204 wt.% 135 wt.% Br and 0·007 wt.% Cu have used a simple od which selectively eliminates the signal of matrix (figure 30). Keeping the dc magnetic field fixed tensity of Cu^{++} resonance is monitored as a function adiation time (mercury lamp light focused through al fibre). The role of the hole trapped by copper monstrated to be both to stabilize such holes and enerate the interstitial silver ions which trap the ons.

R studies of time evolution of photo-induced Cu^{++} ermally-bleached silver halide photochrome glasses ant *et al* 1993) have shown that during exposure V light, only one stable Cu^{++} species — a Cu^{++}–Ag cy complex with silver in a nearest neighbour on $(Cu^{++}–V_{Ag})_A$ — is formed. It is characterized by $\cdot 116, g_y = 2{\cdot}244, g_z = 2{\cdot}076$ and $A_x = 6{\cdot}8, A_y = 7{\cdot}0,$ 2·3 mT. This centre decays rapidly in the dark, gh two parallel mechanisms:

)islocation of the complex $(Cu^{++} + e^- \rightarrow Cu^+)$ by displacement of vacancy along a (Chen *et al* direction in the fcc lattice of $AgCl_xBr_{1-x}$, with ar vation energy of 0·44 eV and a frequency $3{\cdot}4 \times 10^5$ s^{-1}.

(ii) Conversion of $(Cu^{++}V_{Ag})_A$ to $(Cu^{++}\ Cl^-\ V_{Ag})_B$ the silver vacancy is in the next nearest neig position along (Chen *et al* 1985) direction, wi same activation energy as *A* but with a slightly frequency factor of $3{\cdot}1 \times 10^5$ s^{-1}. The $(Cu^{++}\ Cl^-$ centre with $g_x = 2{\cdot}066, g_y = 2{\cdot}077, g_z = 6{\cdot}5$ mT, slowly by a vacancy hopping mechanism $(B) \rightarrow Cu^{++})$ with an activation energy 0·22 eV frequency factor of 4·6 s^{-1}.

Annihilation of *A* and *B* centres via the formati a Cu^+ ion and a neutral complex $(Ag^{++}V_{Ag})_A$ (migrates to the surface of the silver halide pa

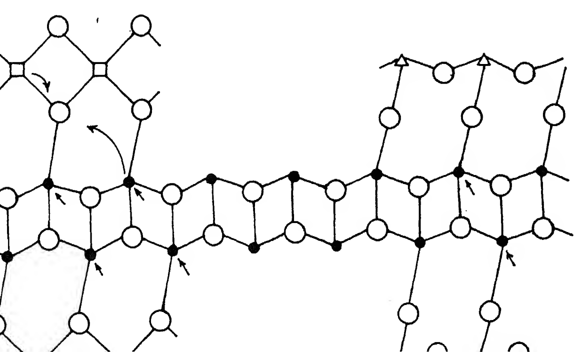

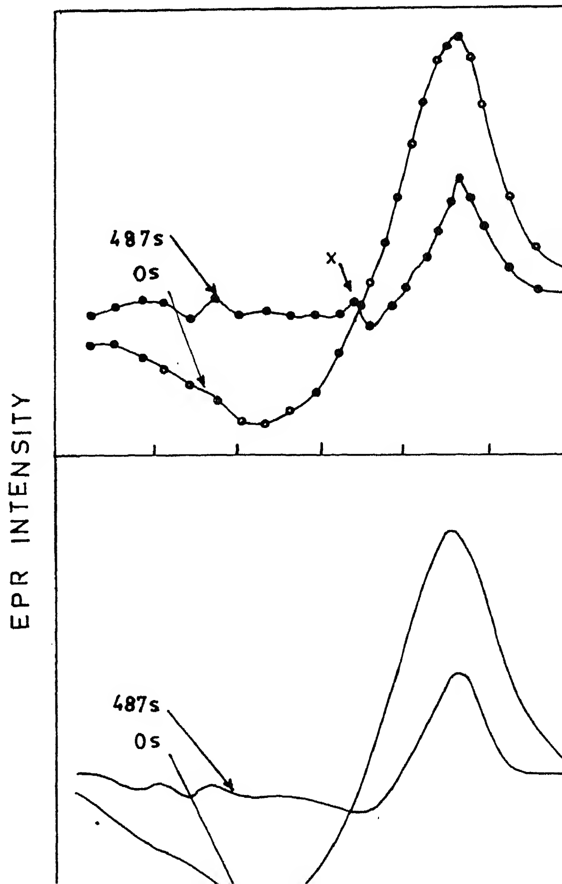

where electron–hole recombination occurs) explain these two decay channels. This study convincingly demonstrates that the $Cu^{++}(A)$ centre is the one detected at equilibrium darkening while Cu^{++} (B) is the one found at the end of thermal bleaching.

10.1.3b *Fluoride glasses*: Halide glasses in general and fluoride glasses in particular, are an important class of optical materials. Water-free BeF_2 glass for instance, is a laser host and a UV window material besides being a core material for ultra-low loss optical fibres. Structurally, BeF_2 glass is akin to fused silica so that a study of impurity ESR spectra would offer important clues to local structure. An ESR study of 'distilled' BeF_2 glasses containing traces of Mn^{++} (13 ppm), Ni (< 1·9 ppm) and Fe (20 ppm) have revealed (Griscom *et al* 1986) two resonances: (i) Mn^{++} resonance at $g = 2{\cdot}0$ of six primary hyperfine lines with each line showing a clear $^{19}F(I = 1/2)$. Super hyperfine splitting of at least six components due to F-neighbours, when studied at 35 GHz (figure 31) and (ii) an FMR signal due to precipitated heterogeneous magnetite-like phases similar to $NiFe_2O_4$.

A computer simulation of the Mn^{++} spectrum based on an isotropic ^{19}F splitting of 15 G and assuming an octahedral surroundings for Mn^{++} reproduces fairly well the experimental spectrum, leading to the conclusion that the predominant coordination state on Mn^{++} in BeF_2 glass is six-fold.

10.2 *Ceramics*

Ceramics are ubiquitous materials with uses ranging from capacitors and support for catalysts to devices based on high temperature superconductors. Paramagnetic centres occur in these materials as trace impurities or as deliberately doped additives or else as defects created as a result of the processing employed to synthesize or modify them. EPR could be used to monitor either the process itself or to characterize the processed materials.

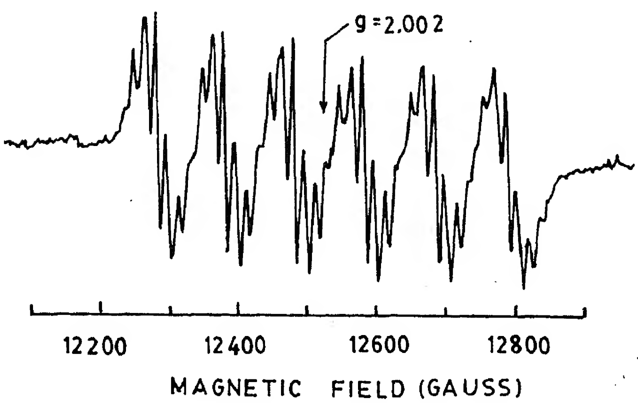

Figure 31. A 35 GHz ESR spectrum of Mn^{++} in distilled BeF_2 glasses, showing the six ^{55}Mn $(I = 5/2)$ primary hyperfine lines and the superhyperfine splitting of at least six components due to F neighbours in the glass network.

10.2.1 *Catalytic ceramics*

10.2.1a *Shock-modified rutile*: High pressure (4·5–27 GPa) shock-modified rutile is found to exhibit enhanced catalytic activity (Graham *et al* 1986). Shock compression does not introduce any structural changes but creates anisotropic residual strain leading to the formation of paramagnetic defects. These defects are stable even at 450°C where catalytic activity is monitored. ESR studies at liquid helium temperatures reveal unique features of these defects and their relation to enhanced catalytic activity. While the starting powder is white and exhibits no ESR, it turns dark grey upon shock compression, the darkness being a function of shock conditions. When the dark grey powder is annealed in air around 500–600°C, the original whiteness is restored.

Two intense resonances are produced due to shock compression: an isotropic one with $g = 2{\cdot}0029(3)$ and an axially symmetric defect with $g_{\parallel} = 1{\cdot}969(5)$, $g_{\perp} = 1{\cdot}937(3)$ for 20 GPa shock. The first one, due to free electrons trapped at a vacancy is less intense (concentration: 3×10^{16}) than the second one, due to a reduction in valence of interstitial Ti from +4 to +3. Higher shock pressures do not alter the concentration of the axial defects but introduce a strong dispersion in the lineshape.

10.2.1b *Vanadia catalysts*: The study of the mechanism of heterogeneous catalysis requires in-depth studies of the active intermediates formed by transition metal ions interacting with various molecules on the surface of a supported oxide catalyst. ESR offers a powerful and sensitive technique with which to determine (i) oxidation states, (ii) surface and bulk coordination, and (iii) the physical form of a transition metal oxide on a diamagnetic support (Kazanskii 1976). This technique has been applied to V_2O_5 catalysts supported on SiO_2, Al_2O_3, MgO as well as MoO_3 and TiO_2 to obtain specific information about (i) the local structure around the paramagnetic V^{4+} $(3d^1)$, (ii) the differences in the microstructure arising from the distinct nature of the support and (iii) the so-called 'carrier effect' involving the support and active sites. Results of such investigations allow definite conclusions to be drawn about the reactivity of V^{4+} with gaseous oxygen formed on the supported catalysts, which is the theme of heterogeneous catalysis.

Vanadia catalysis supported on alumina has been used in a number of oxidation and ammoxidation reactions involving aromatic hydrocarbons and also for reduction of NO with NH_3. ESR characterization of the catalyst with respect to the amount of transition metal oxide and

nditions of reduction is an important first step towards timization, for end use in an actual reaction.

n a typical study (Chary *et al* 1984), 3·41–20·11 wt% O_5 prepared by decomposition of NH_4VO_3, impregnated 60–70 mesh γ-Al_2O_3 support with a pore volume cm³/g and surface area 188 m²/g and reduced by wing hydrogen (500°C), was investigated by ESR. ile the colour of the catalysts ranged from light green dark yellow as V_2O_5 content was increased, none of catalysts exhibited any ESR at 300 K, unlike the upported V_2O_5 which shows a symmetric singlet ESR 300 K with $g = 2{\cdot}000$, $\Delta H_{pp} = 17$ mT which reduces to 2 mT at 109 K. The ESR spectra of the catalysts ained at 109 K (figure 32a) are characteristic of isolated or $(V\ldots O)^{2+}$ species in a ligand field of axial nmetry produced by a distorted octahedron of oxygen s (table 12). For V_2O_5 content equal to or in excess 9·84%, the low-field parallel ^{51}V ($I = 7/2$) hyperfine nponents (figure 32b) of the axial ESR spectra show iblet structure, characteristic of two chemically distinct V^{4+} species. The concentration of the second component attains a maximum when the V_2O_5 content in the catalyst is 20·11%. The second, weaker set of parallel components, also due to V^{4+} could arise from a relatively unstable intermediate whose ligands consist of adsorbed oxygen atoms. An examination of the crystal structures of the orthorhombic V_2O_5 (figure 32c) and cubic γ-Al_2O_3 reveals that the two distinct set of hyperfine peaks arise from V^{4+} occupying octahedral and tetrahedral vacant sites surrounded by oxygens in the γ-Al_2O_3 lattice. Thus on the surface of γ-Al_2O_3 one could have V^{4+} dispersed uniformly as active sites with tetrahedral or square pyramidal surroundings, with dynamic equilibrium between the two and with the number of sites available for occupation depending on the concentration of V_2O_5 in the catalyst.

10.2.1c *Molybdenum sulphide catalysts*: Heterocracking — an important catalytic process in the conversion of crude petroleum to gasoline — uses molybdenum

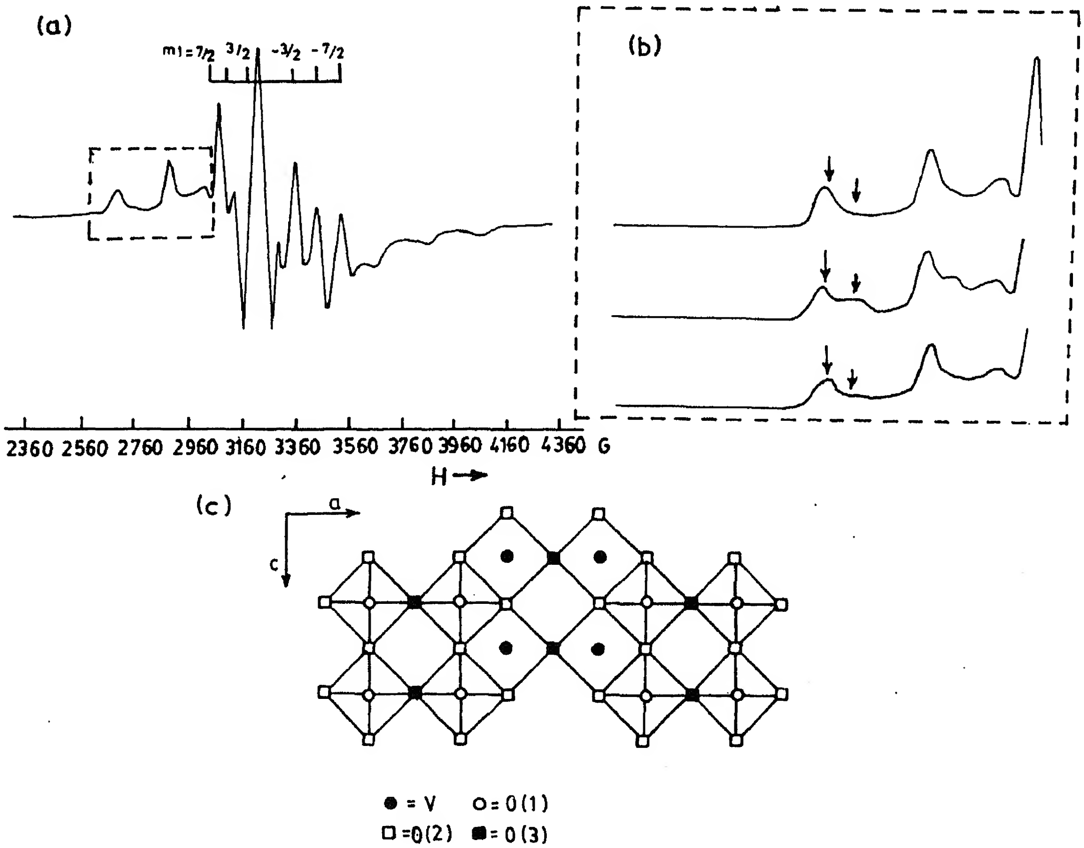

Figure 32. **a.** ESR spectra of a reduced 3·41% vanadia catalyst supported on γ-alumina, at 109 K. The parallel and perpendicular hyperfine structures of ^{51}V ($I = 7/2$) are clearly resolved, **b.** evolution of the low field parallel ESR peaks (marked area in (**a**)) as a function of V_2O_5 content. Top: 6·96%, middle: 9·84%, bottom: 11·89%. The lengths of arrows indicate relative peak heights of the main and subsidiary V^{4+} centres and **c.** schematic structure of V_2O_5 in the crystallographic ac plane with VO_5 polyhedra idealized to tetragonal pyramids. The O(1) oxygens forming the strongest bonds with V are shown as open circles (Chary *et al* 1984).

sulphide as a catalyst. The catalyst is prepared from Mo–oxides sulphurized either before melting with petroleum or directly *in situ*. Usually sulphurization is never complete, and thus the catalytically active compounds are Mo sulphides in which oxygen remains. The electron configuration of the catalyst determines the catalytic process.

ESR measurements of amorphous MoS_{2+x} $(0 \leq x \leq 1)$ and their compounds MoS_yO_z obtained by oxygen exposure at 130°C have revealed the nature and concentration of active sites (Bensimon *et al* 1992). The ESR spectrum is always the sum of three elementary signals arising from (i) unsaturated sulphur atoms and characterized by $g = 2{\cdot}027 \pm 0{\cdot}001, 2{\cdot}038$ and $2{\cdot}034$ for MoS_2, $MoS_{2{\cdot}6}$ and MoS_3, respectively, and (ii) Mo^{5+} $(4d^1)$ found in two different surroundings, as reflected by the g-tensors: A: 0·02, 1·99 and 1·97 and B: 1·94, 1·92 and 1·89. As the evolution from MoS_3 to MoS_2 proceeds, the spectra show a drastic modification around the composition $MoS_{2{\cdot}6}$ by way of a 'pseudo-transition' in which a change in the short-range structural order of the amorphous solid occurs. This is confirmed by the influence of oxygen exposure which leads to an increasing number of paramagnetic defects in accordance with catalytic properties.

10.2.2 *Cuprate ceramics*

CuO and its binary and ternary compounds with MO (M = Mg, Sr, Ca, Ba) and R_2O_3 (R = Y, La, Gd, Nd, Bi, Tl) form an extensive class of magnetic (e.g. Bi_2CuO_4 antiferromagnetic, $T_N = 42$ K) and superconducting ceramics (e.g. $YBa_2Cu_3O_7$ with $T_c \sim 90$ K, $Bi_2Sr_2CaCu_2O_8$ with $T_c = 120$ K) whose study is crucial to a basic understanding of magnetism and superconductivity, and, eventual applications to high-field magnets and magnetic levitation. Zero-field and low-field microwave absorption and ESR have played a significant role in the characterization of superconducting ceramics.

10.2.2a *Cupric oxide*: Cupric oxide, the precursor to high-T_c superconductors of the La-, Y-, Bi-, Tl-, and Hg-families, is a monoclinic-structured anti-ferromagnetic insulator, with a Neel temperature T_N of 230 K. A recent ESR study at 45 GHz (Kindo *et al* 1990), using pulsed magnetic field and a reflection cavity has detected a 1·6 T wide resonance line at room temperature, with a slight temperature dependence of $g \approx 2{\cdot}0$ and a lineshape between Lorentzian and Gaussian, and arises from anisotropic exchange interaction between Cu^{++} spins. The linewidth decreases as the temperature is decreased and the line broadens near T_N due to critical slowing down. One-dimensional spin correlation is seen in the ESR line-profile.

The antiferromagnetic coupling between Cu spins via oxygen atoms is believed to be important for the mechanism of superconductivity in cuprate superconductors.

10.2.2b *Ternary cuprates*: Compared to CuO, ternary cuprates $SrCuO_2$, Sr_2CuO_3, Ca_2CuO_3, Li_2CuO_2, and Bi_2CuO_4 have very small net magnetic susceptibilities and a few of these have very low T_N values. Li_2CuO_2, with $T_N = 9{\cdot}3$ K and Bi_2CuO_4, are both three-dimensional antiferromagnets. Bi_2CuO_4, which has a simple antiferromagnetic order consisting of magnetic moments

Table 12. Spin Hamiltonian parameters of V^{4+} in V_2O_5/γ-$Al_2O_3^{\#}$.

V_2O_5 content (wt %)	Colour of catalyst	$g_\parallel$	$g_\perp$	$A_\parallel$ (mT)	$A_\perp$ (mT)
3·41	light green	1·940	2·000	19·4	7·1
6·96	light green	1·939	1·997	19·4	7·3
9·84	dark green	M 1·942	2·000	19·4	7·0
		S 1·983		17·5	
11·89	light yellow	M 1·942	1·999	19·2	7·0
		S 1·983		17·0	
13·64	dark yellow	M 1·938	1·995	19·4	7·1
		S 1·971		17·4	
14·76	dark yellow	M 1·939	1·998	19·2	7·2
16·37	dark yellow	M 1·941	1·999	19·2	7·1
		S 1·977		17·5	
18·46	dark yellow	M 1·939	1·999	19·3	7·1
		S 1·966		18·0	
20·11	dark yellow	M 1·939	1·997	19·2	7·1
		S 1·960		18·0	

#Chary *et al* (1984); M: Main centre; S: additional centre.

gned ferromagnetically along c-axis and antiferromagtically between spins at the corner and body-centre es of the orthorhombic crystal lattice. ESR of the wder at $T > T_N$ at X-band gives a resonance at $= 2{\cdot}09$, while for a single crystal at 370·4 K and 265 K hta *et al* 1992), an axial spectrum is obtained with $= 2{\cdot}26 \pm 0{\cdot}01$ and $g_{\perp} = 2{\cdot}04 \pm 0{\cdot}01$ for $H_{\parallel}$ c-axis and c-axis, suggesting Cu^{++} situated at an pseudo octahedral e, even though there are only four oxygen ligands for $^{++}$. The line is Lorentzian and exchange-narrowed and linewidth $(0{\cdot}37 \pm 0{\cdot}03)$ T is almost field independent. antiferromagnetic resonance mode of the planar type iferromagnet has been observed below T_N.

.2.2c *Cuprate superconductors*: Nonresonant microve absorption in small magnetic fields is one of the st sensitive techniques for observing small amounts of superconducting phase in an otherwise nonsuperconducting environment (Muller *et al* 1980; Bhat *et al* 1987) or small amount of nonsuperconducting impurity in an otherwise superconducting sample, by way of Cu^{++} ESR with $g_{\parallel} = 2{\cdot}117$, $g_{\perp} = 2{\cdot}120$ for $BaCuO_2$ (Jones *et al* 1990). In this simple technique the sample is placed in a microwave cavity at ~ 9 GHz which is connected to a standard ESR spectrometer. A small magnetic field (± 10 mT) and a modulation field parallel to the external field are applied to the sample. The change in the microwave absorption is detected via lock-in amplifier when varying the external field.

The shape of the signal (figure 33a) is characteristic of a granular superconductor in the superconducting state. This frequency independent signal which vanishes above T_c is caused by weak links or Josephson junctions connecting large superconducting areas, and represents the change of the superconducting surface impedance as a function of the applied magnetic field. This technique has been applied (Mehring *et al* 1993) to the study of the topology of superconducting phase changes in La_2CuO_4 : Sr processing parameters especially the rate of cooling, which decides the size and shape of superconducting region. The low-field microwave absorption (figure 33b), shows a maximum at a field which is recognized as the lower critical field, H_c, of the superconductor. For $H > H_{c1}$ the superconductor enters the 'mixed state' which persists until the upper critical field, H_{c2}, ($H_{c2} \gg H_{c1}$) (Tinkham 1980). For $0 < H < H_{c1}$, the microwaves penetrate only the sample surface, while for

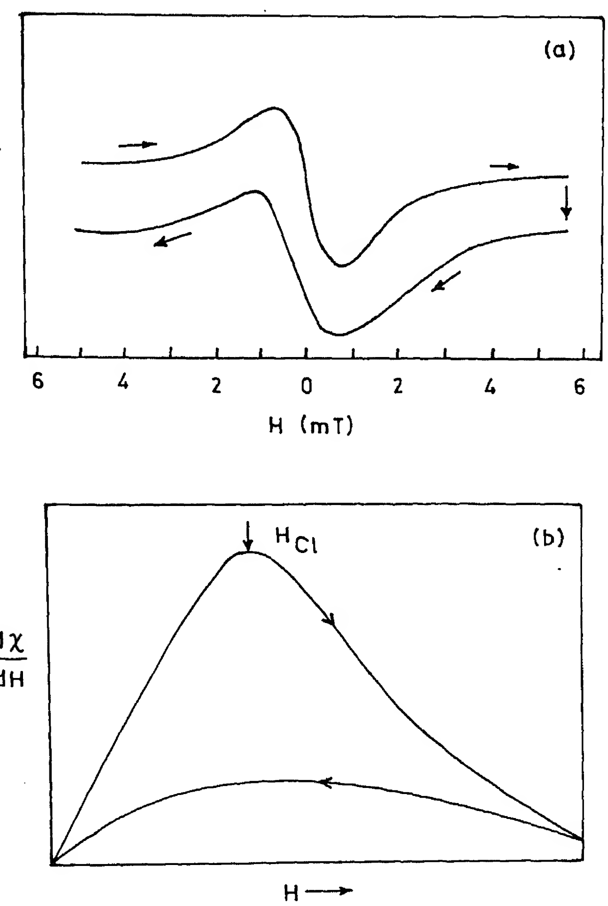

ure 33. Zero-field and low-field microwave absorption in h temperature cuprate ceramic superconductors (schematic). The frequency-independent, reversible, absorption as the dc gnetic field is scanned from negative through zero to positive **b.** the low-field microwave absorption showing hysteresis. turning point obtained upon increasing magnetic field from corresponds to the lower critical field (H_{cl}) which racterizes these granular, type II superconductors.

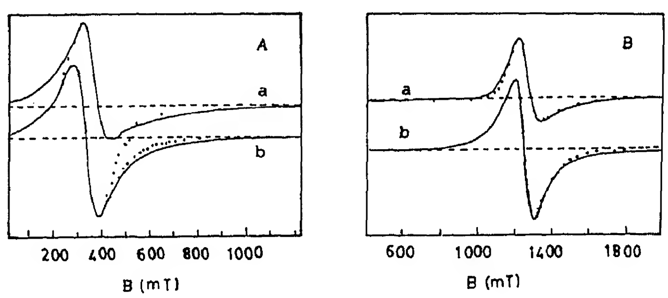

Figure 34. ESR spectra of superconducting, orthorhombic $GdBa_2Cu_3O_7$ (with $T_c \sim 90$ K), at 300 K. **A.** (**a**) X-band ($\nu = 9{\cdot}384$ GHz) spectrum of single crystal at 20 mW power and modulation of 2 mT peak-to-peak: $g_{eff} = 1{\cdot}82$, $\Delta H_{pp} = 128 \pm 6$ mT static field parallel to c-axis. The line has been fitted (*) to a Dysonian shape and (**b**) powder spectrum at 9·380 GHz $g = 2{\cdot}02$ $\Delta H_{pp} = 112 \pm 6$ mT, fitted to Lorentzian (*) and Gaussian (.) shapes. **B.** (**a**) Q-band (34·982 GHz) spectrum of single crystal at 5 mW power and 4 mT modulation amplitude. $g_{eff} = 1{\cdot}96$ and $\Delta H_{pp} = 124 \pm 8$ mT, fitted to a Dysonian shape (*) and (**b**) powder spectrum at 35·001 GHz and 5 mW. $g = 2{\cdot}004$ and $\Delta H_{pp} = 108 \pm 4$ mT fitted to Lorentzian (*) and Gaussian (.) shapes. In (**A**) and (**B**) the ESR intensity of same sample increased by factors of 7 and 20 respectively upon grinding (Deville *et al* 1993).

$H > H_{c1}$ microwaves penetrate into the core of the superconductor. Thus we have a quick and convenient method of determining H_{c1} of high T_c (type II) superconductor using a conventional EPR spectrometer after compensating for remnant field of the electromagnet (Janes *et al* 1991).

ESR has been applied to (i) look at the pinning centres for the flux motion in the $YBa_2Cu_3O_7$ superconductor (Baranov and Badalyan 1993), (ii) the nature of the paramagnetic systems in the normal state ($T > T_c$) of $GdBa_2Cu_3O_7$ (Deville *et al* 1993) (figure 34) and (iii) the study of flux line lattice through measurement of the magnetic penetration depth (λ) in ceramic $YBa_2Cu_3O_7$, $Bi_2Sr_2CaCu_2O_8$ (Rakvin *et al* 1990), and $Tl_2Ba_2Ca_2Cu_3O_{10}$ (figure 35) and single crystals of $YB_2Cu_3O_7$ (Koshta *et al* 1993), with the surfaces coated (decorated) by organic radical of DPPH (the calibration standard for g-factor). In the superconducting state, there is observed an inhomogeneously broadened ESR signal from DPPH due to the so-called flux-line lattice formation. From the temperature-dependent linewidth the magnetic penetration depth at 0°K (λ_0) is calculated. The variation of λ follows the law

$$[1 - (T/T_c)^4]^{-1/2}.$$

Experiments on single crystal samples show that the main contribution to inhomogeneous broadening comes from the flux lattice and not from granularity and screening effects.

10.2.3 *Fullerenes*: Superconductors based on the C_{60} or Buckminsterfullerene or fullerene, with soccerball structure and unusual electronic structure that makes it accept up to 6 electrons obtained by intercalating it with alkali metals K (Hebard *et al* 1991) and Rb (K_3C_{60} : $T_c = 18$ K; Rb_3C_{60} : $T_c = 28$ K), exhibit well-defined ESR spectra in their normal and superconducting states. A precise ESR study of K_xC_{60} (Kosaka *et al* 1993) ($x = 3$, face centred cubic (fcc); $x = 4$, body centred tetragonal (bct); $x = 6$, body centred cubic (bcc)) has clearly identified resonances at g's = 2·0014, 2·0004 and 1·9952 (figure 36) as arising from the fcc, bct and bcc phases, respectively. In another interesting application to Rb_xC_{60} compounds (Byszewski *et al* 1992), thermally-treated samples (diffusion of Rb into C_{60} powder at

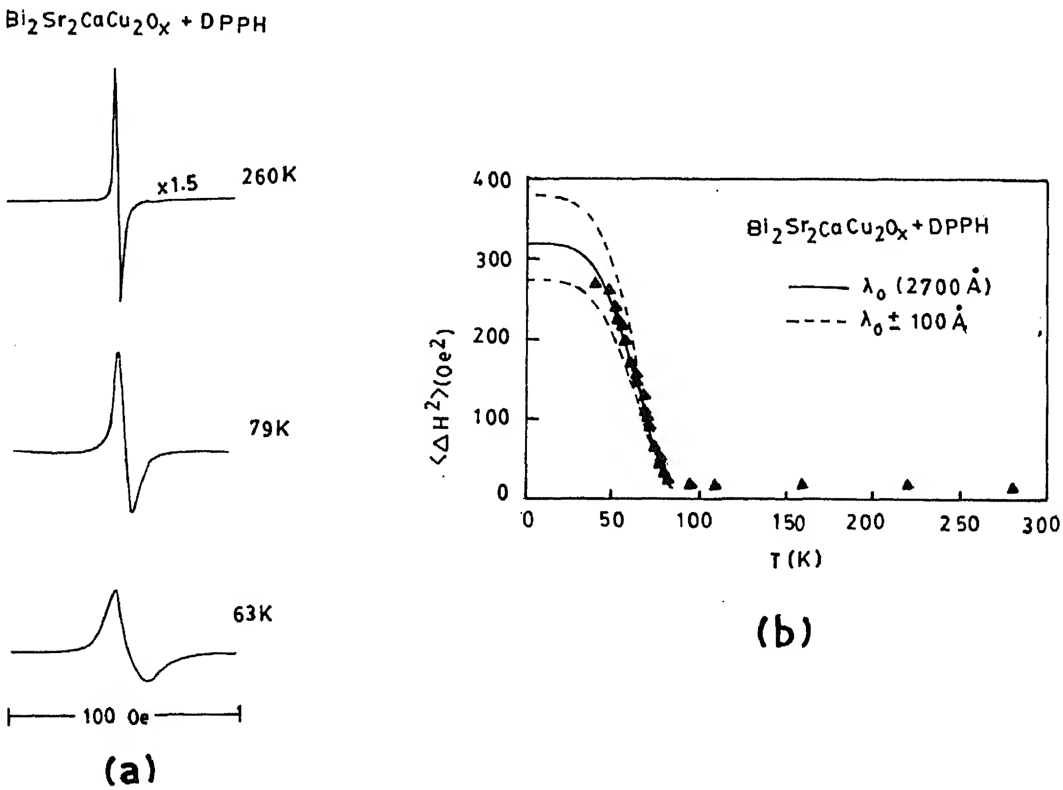

Figure 35. ESR spectra of DPPH absorbed on $Bi_2Sr_2CaCu_2O_x$ superconductor, in order to determine microwave penetration depth. **a.** Temperature dependence through the superconducting transition temperature ($T_c = 82$ K). Note the significant line broadening below T_c and **b.** temperature dependence of second moment or linewidth of DPPH ESR signal. The solid line is a theoretical fit (see text) which yields zero temperature penetration depth (λ_0) of 2700 Å with $T_c = 84$. The dashed lines correspond to fits with 2700 ± 100 Å which shows that the λ_0 deduced is accurate to better than 3·7% (Rakvin *et al* 1990).

)–450°C and subsequent homogenization at 200–)°C) exhibited ESR signals due to an on-molecule ctronic state. Thus clear differences exist in the ESR tern at the transition from normal to superconducting te, by way of a decrease in ESR signal amplitude at superconducting to normal state transition. Thus it ears that carriers partially localized on the C_{60} mole-es due to the Coulomb repulsion energy form super-ducting states by intermolecular coupling.

Optoelectronic and superionic materials

1 *Optoelectronic materials*

:oelectronic phenomena rely on the ability of certain erials (e.g. $BaTiO_3$, $Bi_4Ge_3O_{12}$) to exhibit photo-omic and photorefractive effects. These materials ond to light-induced space-charges by large changes he refractive index (Gunter and Heiguard 1988, 1989). se effects arise from the UV/visible light sensitivity transition metal impurities doped in these materials. R is thus a natural technique to apply to these materials learn about the valence state of the doping ions, nges in the valence state under illumination, and the sical location of the impurity in the crystal lattice. s basic characterization is crucial for all applications uding optical memory and information storage, uency doubling and parametric oscillation, as an ortant first step towards optimization of device formance.

11.1a *Barium titanate*: Barium titanate — the well known ferroelectric material — when doped with transition metal ions of iron group and suitably poled to give wide (~ 10 K) thermal hysteresis for the cubic-to-tetragonal phase transitions at nearly 130°C on cooling, exhibits high photorefractive gain and is thus of interest for many applications that involve optical phase conjugation and signal processing. The origin of its photorefractive properties i.e. the exact nature of the microscopic centres responsible for the large changes in refractive index light-induced space is linked with (i) control of doping level of single crystals, (ii) discrimination between dopant-related charge-compensation-related effects, and (iii) the oxygen vacancies created by thermal treatments (e.g. in oxidizing/reducing atmospheres).

EPR experiments with transition–metal-doped $BaTiO_3$ powder treated under a wide range of oxygen partial pressures revealed valence state changes in Co, Cr and Mn-doped material whereas for the dopants Fe, Ni and Cu such changes were absent, which suggest that the former group of ions are likely to show better photorefractive effect than the latter. Of Co, Cr and Mn, Mn has a smaller optical absorption while Cr-doped crystals of optical quality are difficult to obtain. Thus Co-doped $BaTiO_3$ emerges as the most promising candidate for photorefraction.

The EPR spectrum of powdered single crystal of 50 ppm Co-doped $BaTiO_3$ processed in a reducing atmosphere at 18 K (Rytz *et al* 1990) is shown in figure 37. It exhibits the extended hyperfine structure (by way of two overlapping octets) that arise from the

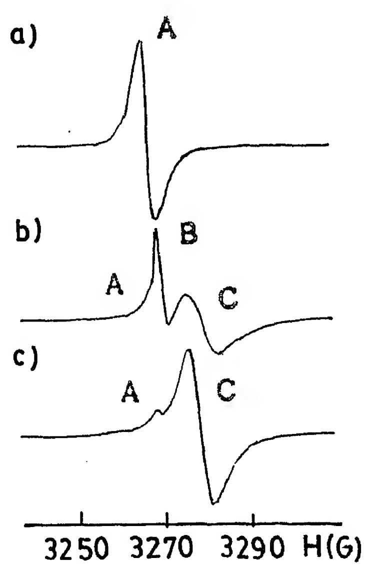

re 36. ESR spectra, at 5 K, of K-intercalated C_{60} **(a)** K_3C_{60}, K_4C_{60} and **(c)** K_6C_{60}. The signals A, B and C correspond cc, bct and bcc phases of these fullerenes (Kosaka *et al*).

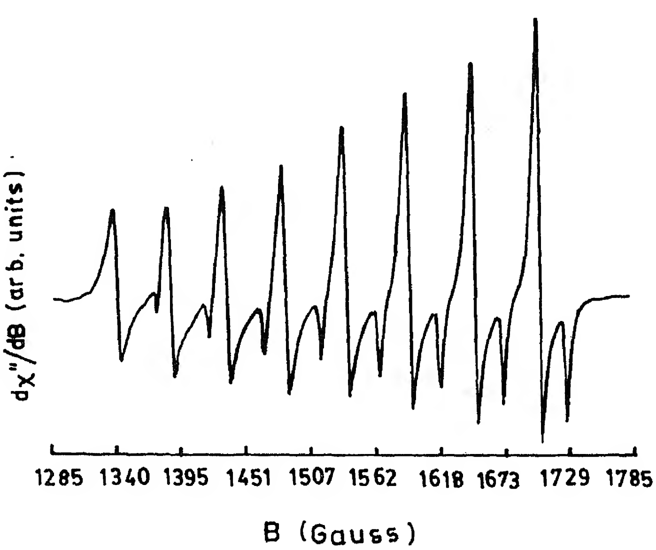

Figure 37. X-band EPR spectrum of powdered single crystal of $BaTiO_3$: Co at 18 K, recorded at 1 mW power, and 9·26569 GHz, with a field modulation of 0·2 mT. The octet is assigned to Co^{2+} with $S = 3/2$, $I = 7/2$, with $g_{\parallel} = g_{\perp} = 4{\cdot}341$ and $|A| = 5{\cdot}16$ mT (Rytz *et al* 1990).

100% abundant ^{59}Co ($I = 7/2$). For the intense octet, $g_{\parallel} = g_{\perp} = 4{\cdot}341$ with hyperfine constant $|A| = 5{\cdot}16$ mT. The octet is assigned to high spin Co^{2+} with $S = 3/2$. A spin Hamiltonian with isotropic g and moderate zero field splitting accounts for the spectrum. Besides this, an intense feature with $g = 2{\cdot}004$ due to high spin Fe^{3+} ($S = 5/2$) is also present. This high spin Co^{2+} not associated with an oxygen vacancy is EPR active, while Co^{2+}, (low spin $S = 1/2$) — oxygen vacancy, complex a product of reduction diamagnetic Co^{3+} (low spin) — oxygen vacancy complex — though EPR active is not detected at X-band frequencies.

11.1b *Lead–zirconate–titanate*: Ferroelectric lead–zirconate–titanate (PZT) thin films find use in nonvolatile memories and optical information storage devices. Defects and optically-induced metastable trapping centres in PZT control the electrical and optical behaviour. It is thus necessary to understand the nature of these trapping centres.

Warren *et al* (1993) have identified, through EPR, a positively charged Pb^{3+} defect centre in PZT (Zr/Ti = 53/47) ceramics. The charged traps were generated by ultraviolet illumination in the band gap region (3·4 eV). The EPR spectrum of the centre, recorded using high power microwave quanta of $0{\cdot}314652\,cm^{-1}$ and second harmonic detection, consists of an intense peak with $g = 1{\cdot}995$ at 0·5530 T arising from non-magnetic Pb nuclei, a weaker line 1·145 T, caused by a very large hyperfine ($A_{isotropic} = 1{\cdot}0803\,cm^{-1}$ or 1·1599 T, $A_{aniso} = 0{\cdot}00233\,cm^{-1}$ or 2·5 mT) with a less abundant ^{207}Pb nucleus with $I = 1/2$, on the basis of which the centre is assigned to Pb^{3+} which has valence-shell configuration of $6s^1$. Pb^{3+} could arise from some of the Pb^{2+} corner-sites in the perovskite PZT lattice, by capturing a hole and becoming paramagnetic. The centre is further characterized through its wave function with 40% 6s-character and at the most 8% 6p-character so that there is 48% localization of unpaired electron on Pb atom, with the rest of ≈ 52% unpaired spin density being spread over the 12 oxygen neighbours in the perovskite.

11.1c *Bismuth germanate*: $Bi_4Ge_3O_{12}$ has a crystal structure made up of a cubic arrangement of distorted oxygen octahedra surrounding each Bi^{3+} ion and oxygen tetrahedra around each Ge^{4+}. Thus it offers two sites — Bi^{3+} and Ge^{4+} — for occupation by a transition metal rare earth impurity ion (Bravo *et al* 1993). EPR studies have established that Gd^{3+} impurities occupy Bi^{3+} sites, while Cr ions, detected as Cr^{4+} occupy Ge^{4+}, and Cr^{3+} occupy Bi^{3+} sites. Mn^{++} ions are found to occupy Bi^{3+} sites without charge compensation, and undergo change of valence under UV illumination. Co^{2+} ions, likewise, are found to occupy Bi^{3+} probably without charge compensation.

11.1d *Lithium vanadate and lithium borate*: These are nonlinear optical materials employed for doubling of optical frequencies e.g. to obtain blue/green light from an infrared laser beam. These materials need to be thoroughly characterized for trace chemical impurities and for irradiation-induced defects because their optical and electrical properties are strongly influenced by defects and impurities.

Lithium vanadate (Li_3VO_4) when prepared in β-II phase, has a second harmonic generation behaviour comparable to that of $LiNbO_3$ (Sakita and Fujii 1991). Two ESR active, trapped hole centres are formed when Li_3VO_4 is exposed to X-rays at 77 K (Murata and Miki 1993): (i) CO_3^-, stable at ambient, with $g_1 = 2{\cdot}021, g_2 = 2{\cdot}011$ and $g_3 = 2{\cdot}0057$, coming from Li_2CO_3 used in sample preparation, and (ii) an intrinsic O^- type centre with one neighbouring vanadium ion, with $g_{xx} = g_{yy} = 2{\cdot}026$, $g_{zz} = 2{\cdot}028$ and $A_{xx} = A_{yy} = 2{\cdot}05$ mT, $A_{zz} = 3{\cdot}075$ mT due to ^{51}V ($I = 7/2$) nucleus. This second centre is unstable above 150 K and is completely annealed at room temperature. Two significant features of this centre viz. poor thermal stability and no coloration at ambient temperature favour the use of Li_3VO_4 as a frequency doubler.

LiB_3O_5 is a common second-harmonic generator material, involving a fundamental wave, around $1{\cdot}06\,\mu m$, with a phase-matching angle along a crystallographic axis. Two unique properties: (i) temperature dependent refractive indices, and (ii) wide (160–1300 nm) range of optical transmission make this an ideal nonlinear material.

Two prominent point defects: (i) a trapped hole centre localized on an oxygen ion near a ^{11}B nucleus (with a smaller ^{11}B hyperfine structure), and (ii) a trapped electron centre — also localized on a ^{11}B but with a larger hyperfine structure — have been observed in the ESR and ENDOR of this biaxial crystal irradiated with γ-rays near 77 K (Scripsick 1993). The significant findings are: (i) the lack of ESR spectra due to transition metal impurities Fe^{3+}, Cr^{3+} and Mn^{2+} present at < 100 ppb level in LiB_2O_5 rather than at ppm level in other SHG materials $LiNbO_3$ and $KTiOPO_4$, and (ii) both the irradiation-induced centres thermally anneal in the 120–130 K range.

11.1e *Other materials*: A recent EPR study has demonstrated (Whitmore 1993) that tetrahedral Cr^{4+} is responsible for the near-infrared laser activity in Cr-doped Forsterite (Mg_2SiO_4). Fe^{3+}, Fe^{3+}-oxygen vacancy, Co^{2+}, Co^{2+}-oxygen vacancy and Ir^{4+} have been identified in photorefractive $KNbO_3$ in its rhombohedral and orthorhombic phases (Possenriede 1989).

11.2 *Superionic materials*

Superionic conductors are ionic solids whose conductivities at ambient temperatures are of the order of molten salt electrolytes and thus they are also called solid

trolytes. Thus any application of ESR to such systems t aim at elucidating the effects of ionic motion and determine site symmetries of defects that block ured hopping paths in the superionic conductor. our such studies are noteworthy: (1) Mn^{++} in PbF_2, Cu^{++} in β-sodium gallate, (3) Ag^{++} in β-alumina and Ag^{++} in $AgI–Ag_2O–B_2O_3$ glass.

a *Mn-doped lead fluoride*: PbF_2 is an F^- ion conor at high temperatures where the high mobility of ons is expected to affect the EPR of Mn^{++} ions by of line narrowing, line broadening and disappearance dditional structure in each of the Mn^{++} ($I = 5/2$) rfine components (Evora and Jaccorino 1977) due nuclei observed at low temperatures (figure 38). ed, at the temperatures of onset of motional narrowing °C (^{19}F hf frequency)) $\tau_{\text{conductivity}} \sim 1$. Above 400°C, lines start to broaden due to a fluctuating crystal . The linewidth increases as m_I^2, where m_I is the ear magnetic quantum number, which is interpreted coustic phonon enhanced spectral density of the uating crystal field. F^- sublattice melting enhances nteraction. This phonon coupling is greatly enhanced rapid ionic diffusion, giving lines as narrow as mT.

) *Copper-doped β-sodium gallate*: In a study of oped single crystal β-sodium gallate isostructural β-alumina, and with nearly same Na^+ conductivity as found that at room temperature, the anisotropic rfine structure of ^{63,65}Cu ($I = 3/2$) and the g-anisotropy u^{++} resonance is washed out/averaged out due to symmetry fluctuations through Cu^{++}/ligand motion (Title and Chandrasekhar 1976). A correlation time (for the Cu^{++}/Cu-O complex) of 10^{-11} sec, two orders faster than Na^+ hopping time (10^{-9} sec) was deduced. A motional effect correlating with ionic diffusion is involved, whereby rapid fluctuations of bridging O^{2-} ions with respect to Cu^{++} triggered by rapid Na^+ diffusion could give rise to the isotropic, structureless ESR line observed.

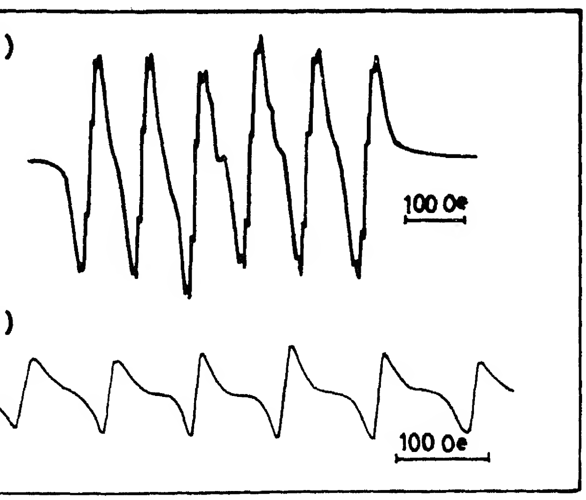

e 38. EPR spectra of Mn^{++} in PbF_2 at (a) 77 K and 60 K. Note the line broadening and absence of additional ure in (b) when PbF_2 is in the disordered superionic phase a and Jaccorino 1977).

11.2c *Ag centres in β-alumina*: Atomic Ag^0 centres and hole Ag^{2+} centres were detected in X-irradiated (77 K) β-alumina crystals (Badalyan and Zhitnikov 1985). Ag was incorporated by immersing Na^+ β-alumina crystals in molten $AgNO_2$ at 350°C. Orientation dependence of g-factor revealed that Ag^{2+} becomes stabilized at 77 K in a position between two oxygen ions as a minor plane. It is this minor plane that separates the four alternate spinel blocks (containing Ag and O ions) of the β-alumina (11 $Al_2O_3 \cdot Na_2O$) structure, and that contains the mobile Na^+ ions besides O ions, and it is these Na^+ ions that are replaced by Ag^+ ions. Two environments for Ag^{2+} are indicated, with the same axial g but with two different sets of planar g's. The ^{107,109}Ag hyperfine interaction constants are low, suggestive of a strong delocalization of the hole from Ag^{++} ion to two oxygen ions on the axis of the centre. A model for Ag^{++} based on these results is shown in figure 39.

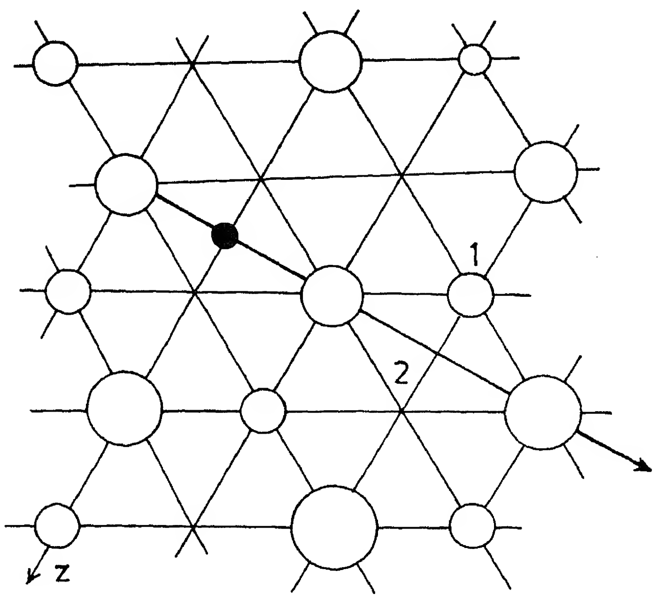

Figure 39. Schematic representation of a reflection plane in the hexagonal β-alumina (Na_2O 11 Al_2O_3) crystal containing Ag^+ ions showing the position occupied by Ag^{++} centre formed by X-irradiation (dark circle). Large circles are O^{2-} and small ones Ag^+/Na^+ ions. 1 and 2 are the occupied and vacant cation sites called Beevers-Ross and anti-Beevers-Ross sites. In the superionic state, Ag^+/Na^+ ions spend some time at 2 (Badalyan and Zhitnikov 1985).

11.2d *Ag^{++} in AgI–Ag_2O–B_2O_3 glass*: ESR-active Ag^{++} ions, stabilized during melt-quenching, in the optimum conductivity 60 AgI–30 Ag_2O–10 B_2O_3 glass have been used to probe the glass structure and Ag^+ conduction mechanism (Balaya and Sunandana 1990). Two clearly distinguishable Ag^{++} ESR species with different thermal stabilities were identified (figure 40, table 13) and attributed Ag^{++} in different chemical surroundings. The ESR data neatly correlate with Minami's structural model (Minami *et al* 1982) for this glass and Ag^+ conductivity. The centre I, with a smaller $A_\perp$ due to ($I = 1/2$ of Ag) is due to less mobile Ag^{2+} bonded covalently to non-bridging oxygens of BO_3, and thus thermally more stable, and not involved in conduction. While the centre II with a larger $A_\perp$, should arise from Ag^+ ion ionically bonded to bridging oxygens of BO_4 groups in the borate glass network, are more mobile and contribute to Ag^+ conduction. Ag^{2+} ESR has also been observed in Ag_2O–TeO_2 (Balaya and Sunandana 1992) glasses where the large covalency of Te–O bond in the glass structure leads to washing out of Ag-hyperfine structure in the ESR spectra.

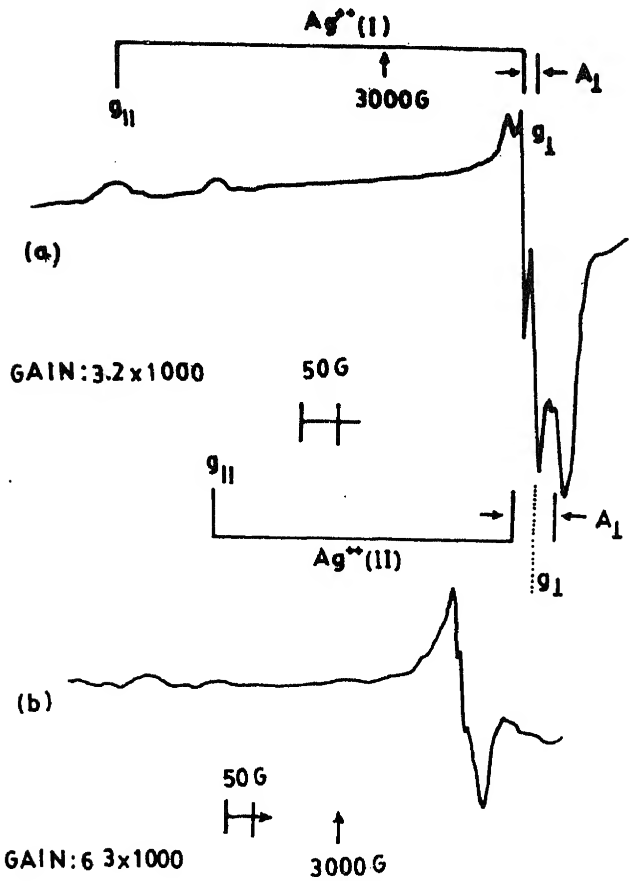

Figure 40. EPR spectra of Ag^{2+} in the superionic conducting 60 AgI·30 Ag_2O·10 B_2O_3 glass at (a) 303 K and (b) 413 K. Note that of the two centres Ag^{++} (I) and Ag^{++} (II), the first one is thermally more stable, and is thus less mobile, while the second one contributes significantly to conductivity (see text) (Balaya and Sunandana 1990).

11.2e *Other materials*: ESR of CO_3^- radical formed by X-irradiation in CO_3^{2-} doped $Li_2SO_4 \cdot H_2O$ single crystal (monoclinic) and cubic (fcc) Li_2SO_4 stabilized at ambient by programmed quenching from the melt aided by a few mole% Li_2CO_3 has been used as a structure sensitive probe (Balaya and Sunandana 1990). The high conducting cubic phase is characterized by a nearly isotropic ESR signal with $g = 2{\cdot}0094$ and $\Delta H_{pp} = 0{\cdot}6$ mT resulting from motional averaging of CO_3^- ions. ESR of DPPH adsorbed on AgI has been used to probe the hexagonal–cubic phase transition (147°C) in AgI (Murthy and Sunandana 1992).

12. ESR imaging and microscopy

12.1 *ESR imaging*

Imaging of the spatial distribution of the properties of advanced materials, especially on a microscopic scale enables a deeper insight into their (physico-chemical) nature to be obtained. ESR imaging (Ikeya 1991) allows for an accurate mapping of the spatially distributed paramagnetic species in the sample. In a typical continuous-wave magnetic resonance imaging experiment, the material is initially placed in a highly uniform dc magnetic field and its ESR spectrum measured (Lauterbur 1973). Then a small magnetic field gradient (1–10 mT/cm) is applied external to the microwave carrier (or inside it) and the broadened, convoluted ESR spectra is recorded. Deconvolution, with the original ESR spectral lineshape gives the spatial distribution of spins because the magnetic field intensity corresponds to the position under a linear magnetic field gradient.

Suppose small magnetic field gradients $\partial H/\mathrm{d}x$, $\partial H/\mathrm{d}y$ and $\partial H/\mathrm{d}z$ are applied, through properly positioned field coils, along x, y and z directions with the uniform field (H_0) along z-direction (H_0). Then the field at the spatial site (x, y, z) is given by

$$H(x, y, z) = H_0 + (\partial H/\partial x)x + (\partial H/\partial y)y + (\partial H/\partial z). \quad (88)$$

Resonance occurs at the magnetic field H_r, for the microwave frequency ν, when $h\nu = g\mu_B H_r$. Thus the field intensity obtained by sweeping H_0 is indicative of the positions.

The spatial distribution function of the spins being imaged, $f(z)$ can be expressed as a function $f(H)$ of the magnetic field H because

$$H = H_0 + (\partial H/\partial z)z = H_0 + bz. \quad (89)$$

The ESR spectrum under the field gradient, $g(H)$ is then expressed as a convolution of $f(H)$ and the signal shape function $r(H)$ in the uniform magnetic field as:

$$g(H) = \int_0^\infty r(H - H')f(H)\,\mathrm{d}H. \quad (90)$$

ıen the Fourier transform (FT) of the above integral obtained as

$$G(\omega) = R(\omega)\, F(\omega), \tag{91}$$

ıere $G(\omega)$, $R(\omega)$ and $F(\omega)$ are the FT's of $g(H)$, $r(H)$ d $f(H)$, respectively. Finally the distribution function H) may be obtained by deconvolution using the inverse of $F(\omega) = G(\omega)/R(\omega)$ with same filter function as $\omega)^{-1}$ diverges.

There are advantages of modulating the field gradient. The resolution of ESR imaging is limited by the ewidth of the resonance signals and the available field dients.

1a *Use of a linear field gradient*: By using a straight r-wire configuration inside a cavity, Furusawa and ya (1991) have imaged an irradiated teflon tube. The ear gradient coil system in a TE_{011} cavity is shown figure 41. The four copper wires connected to each er and to current sources constitute four independent rent loops, the current magnitude and direction of h of which is controlled to produce the linear gradient. ıs the current through the wire located at (γ, θ) in y–z plane is controlled by the equation

$$I(\theta) = I_{max} \cos(\theta - \phi), \tag{92}$$

ere r is the radius of the cylinder, θ the angle from is, I_{max} the maximum current per wire, ϕ the direc- of the linear field gradient produced. The magnetic d around the centre of the four-wire line on gradient e is

$$B_z(y, z) = \frac{4\mu_0 I_{max}}{\pi \cdot r^2}\,(y\cos\phi + z\sin\phi), \tag{93}$$

(where μ_0 is the magnetic permeability of the free space) which implies that the field gradient makes an angle ϕ with y-axis and has a magnitude $8\mu_0 I_{max}/\pi r^2$ (Furusawa and Ikeya 1991). The deconvolution process, the important intermediate step to imaging is shown in figure 42 for the case of a γ-irradiated teflon tube. The ESR spectrum of this sample, without a field gradient (figure 42a) is used as an instrumental function to obtain the deconvoluted spectrum (figure 42c) of the ESR spectrum recorded with field gradient of 1 T/m (figure 42b). The ESR image is finally obtained using the filtered back projection technique (Ohno 1982).

12.1b *Use of two-dimensional wire arrays*: Using an ordinary commercial ESR spectrometer, Ikeya *et al* (1991) have used two-dimensional wire arrays ($i \times j$) for scanning the local static (DC) field and the modulation (100 kHz.AC) field (figure 43a). These two fields — DC and AC — are electronically scanned by switching the current through the array. The spectra for the AC and DC currents at various locations of the $i \times j$ array are shown schematically in figure 43b. When the test sample (DPPH) is outside the loop current from ith to $(i+1)$th wires, an out-of-phase derivative signal is obtained. This is an example of a two-dimensional imaging which when obtained as a plot of signal intensities gives the distribution of spins on the sample surface.

A spectral-spatial two-dimensional imaging of E' defects in X-irradiated SiO_2 has been performed by Sukei *et al* (1993) using a Varian E.9 X-band spectrometer and an additional set of coils which give a gradient of 10 mT/cm/amp along the main magnetic field and a computer for data collection and iterative image reconstruction with filtered back projection.

Table 13. Ag^{2+} ESR parameters in silver iodo-borate and related glasses*.

	g		A	
Sample	$g_{\parallel}$	$g_{\perp}$	$A_{\parallel}$ (mT)	$A_{\perp}$ (mT)
$60AgI–30Ag_2O–10B_2O_3$				
Centre I	2·495(2)	2·060(2)	not resolved	1·8(0·3)
Centre II	2·373(2)	2·054(2)	not resolved	5·6(0·3)
$30Ag_2O–70B_2O_3$				
Centre I	2·503(2)	2·065(2)	not resolved	2·0(3·0)
Centre II	2·388(2)	2·059(2)	not resolved	6·5(0·3)
$30Ag_2O–70TeO_2$				
Centre I	2·493(2)		not resolved	not resolved
Centre II	2·389(2)	2·070	not resolved	not resolved
$Ag_2O–B_2O_3$ X-irradiated	2·310	2·040		
Silver activated phosphate glass X-irradiated at 300 K	2·350	2·050	not resolved	not resolved

*Adapted from Balaya P 1992 *Electrical, thermal and spectroscopic studies on disordered superionic conductors*, Ph.D. thesis, University of Hyderabad, Hyderabad.

12.2 *ESR microscopy*

A one-dimensional scanning ESR microscope based on a microwire array has been built by Miyamura and Ikeya (1993) to obtain ESR images of fossils. This instrument (figure 44a) involves scanning of the localized magnetic field moderation (instead of the static magnetic field) which is facilitated by placing the microwire array on the sample holder. The modulated ESR signals are detected by lock-in-amplifier, ensuring high-sensitive signal detection.

The images of a 'point' DPPH powder (figure 44b) and a naturally irradiated fossil shark tooth, containing CO_2^- radical detected at $g = 2{\cdot}0025$ and $g = 1{\cdot}998$. The signal intensities is high at the enamel point of the tooth at both edges (figure 44c).

Important emerging applications of ESR microscopy include the following (Ikeya 1991):

(I) Monitoring of distribution of active species during catalytic reactions to clarify mechanisms and to design large catalytic reactors.
(II) Evaluation of crystal perfection using anisotropic ESR signals.
(III) Information on crystal growth and inner mantle of the earth, using images of synthetic ruby/sapphire and natural diamonds, respectively.

13. Emerging techniques

Apart from the techniques discussed in § 4, which are routinely employed for the characterization of advanced materials, several new innovative techniques have been developed during the last decade. In what follows a few of these are briefly discussed and possible application areas mentioned.

13.1 *Loop gap resonators and multi frequency EPR*

The cavity resonators employed in EPR spectrometers (e.g. TE_{011} cylindrical cavity) are distributed circuits, and

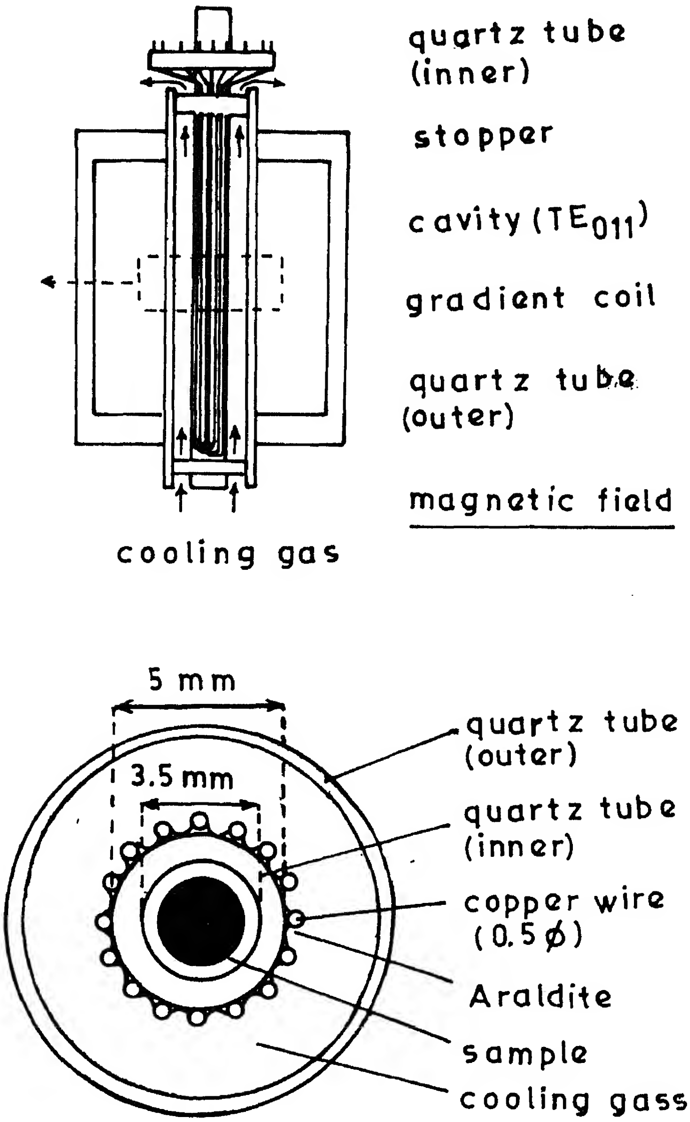

Figure 41. The use of a linear field gradient in ESR imaging. **a.** Field gradient coil in TE_{011} cylindrical cavity and **b.** cross section of the central portion of the gradient coil in the y-z plane (Furusawa and Ikeya 1991).

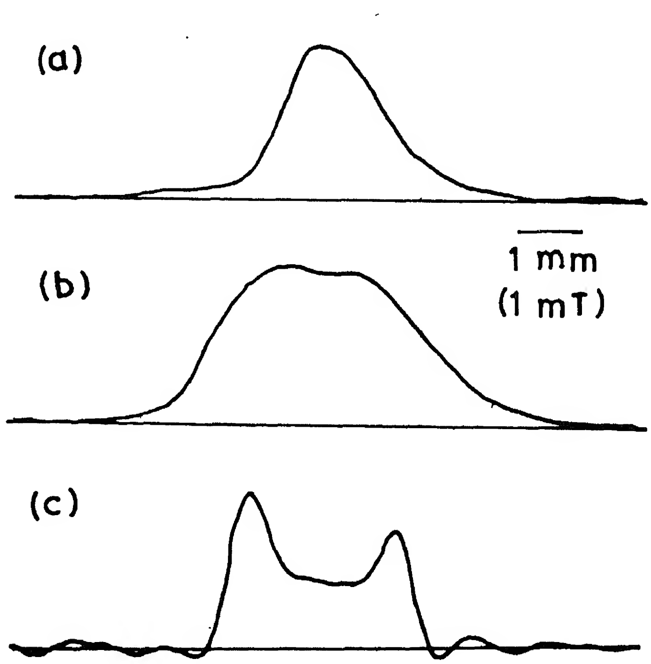

Figure 42. ESR spectrum of a γ-irradiated teflon tube. **a.** Without a magnetic field gradient, **b.** with a field gradient of 1 T/m and **c.** after deconvolution of **b** using spectrum **a** as an instrumental function (Furusawa and Ikeya 1991).

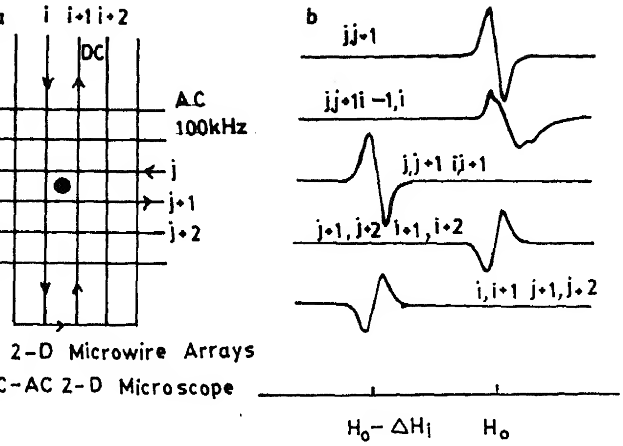

gure 43. Two-dimensional ESR imaging. **a**. Wire arrays ×j) for scanning the static (dc) field and the modulation (ac) ld and **b**. spectra for ac and dc currents at selected locations the wire array with ac current at jth and $(j+1)$th wires and current at jth wires as indicated (Ikeya *et al* 1991).

the dimensions of these cavities are of the order as the wavelength of the microwave radiation. The electric and magnetic field vectors are interdependent and related by Maxwell's equations. The loop gap resonator or LGR, on the other hand, is based on the lumped circuit concept, with the circuit elements R, L and C are clearly defined, the circuit dimensions being small compared to the wavelength by typically 1/10 to 1/3. Most importantly, the electric and magnetic fields are independent of each other in the lumped circuit limit.

For a simple loop of radius r with n gaps, each of width W, separated by t units, the inductance is given by ($n = 1$, 2, 4)

$$L = \frac{\mu_0 \pi r^2}{Z}, \tag{94}$$

and the capacitance by

$$C = \frac{\varepsilon WZ}{tn}, \tag{95}$$

where μ_0 and ε are free space permittivity and dielectric

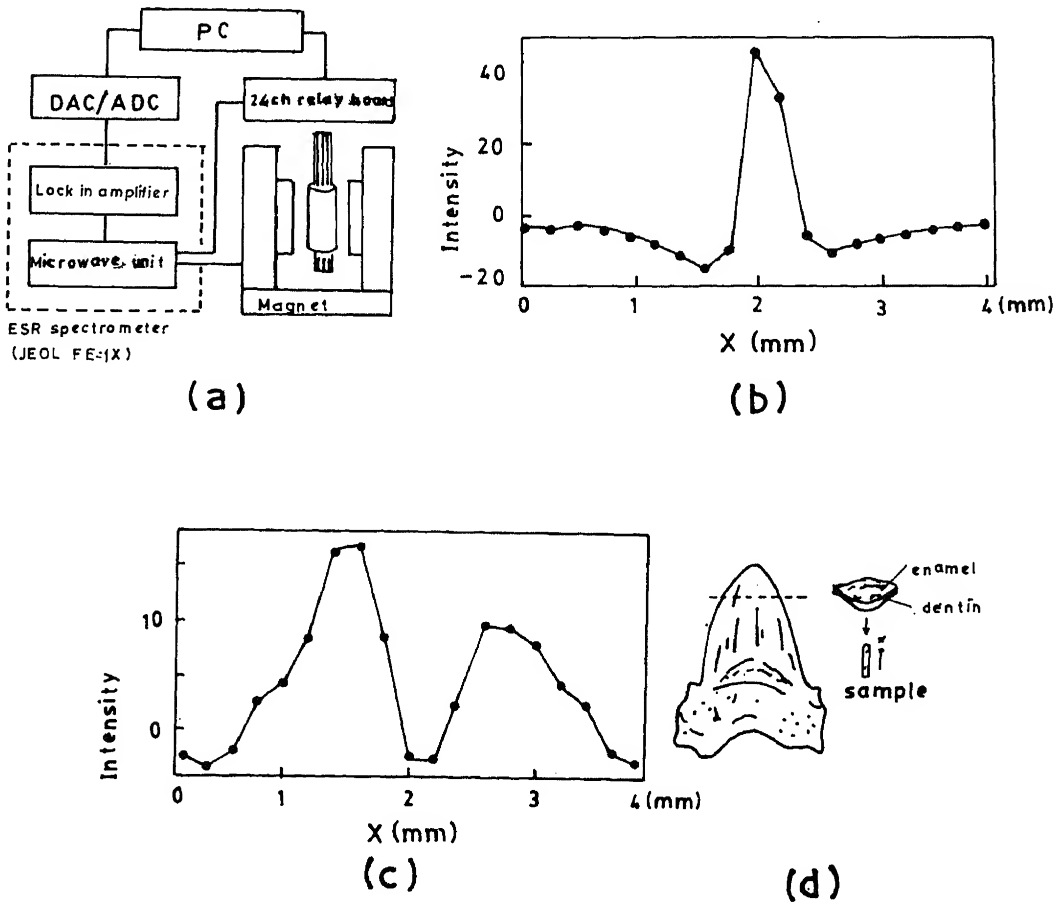

Figure 44. The scanning ESR microscope with micro-wire array and its applications. **a**. Block diagram, **b**. ESR intensity distribution for a DPPH point sample (powder), 200 μm diameter and **c**. one-dimensional ESR image of a fossil shark tooth, cut and scanned as illustrated (Miyamura and Ikeya 1993).

constant and Z the impedance of the circuit. The resonance frequency is

$$\nu_r = \frac{1}{2\pi\sqrt{LC}}. \tag{96}$$

An X-band LGR has a central loop 1–3 cm in diameter, which contains the sample whose EPR spectrum is required. The structure is shielded by a ~ 2 cm diameter radiation shield. The filling factor is nearly 1 for a sample in such a loop. Generally, LGR's have been constructed from low frequencies (10 MHz, for magnetic resonance imaging) to 35 GHz and Q's of 500–2000 have been realized.

An important technical advantage of LGR is the possibility of doing multifrequency EPR i.e. the capability of examining the same sample over a range of frequencies say from 0·5 to 1 and from 4 to 8 GHz (Hyde and Froncisz 1989). For pulsed EPR investigation at X-band frequencies a bridged LGR (BLGR) has been designed (Pfenninger *et al* 1988). With its high rf transparency BLGR is suitable for a variety of multifrequency experiments including pulsed and hyperfine-selective ENDOR, and, Fourier transform EPR (Schweiger 1989).

13.2 *Millimeter wave EPR*

Synthesis and processing of signals in the far-infrared and millimeter wave regions for applications in radar, communications and radio astronomy, have stimulated the efforts towards high frequency and high field EPR spectroscopy. Specific advantages of this technique are increased spectral resolution, permitting very accurate determination of g-tensor principal values, and increased sensitivity to molecular motions besides increased absolute sensitivity for detection (number of electron spins/unit field). Freed and coworkers (1989) have built an 1 mm wave EPR spectrometer that operates at 249·9 GHz generated by a solid state (an InP Gunn Oscillator) and 8·9 T (generated by a superconducting magnet) for $g \sim 2$, with a sensitivity comparable to that of a 9 GHz EPR spectrometer. Their design is based on far-infrared technology that uses the principles of Gaussian optics to propagate the millimeter waves, 'feed-horns' being used for launching the beam and to convert it into a Gaussian beam, and couple it back to the Fabry–Perot cavity resonator housing the sample in a teflon holder. The detector is a Schottky diode coupled to a low-noise video amplifier, whose response is amplified by a lock-in-amplifier, to be digitized and fed to a personal computer.

An important application of this spectrometer is based on its ability to resolve g-anisotropy of nitroxide spin labels and organic free radicals such as DPPH.

13.3 *Reaction yield detected magnetic resonance (RYDMR)*

Many photophysical processes, such as the rate of recombinations of excess carriers in semiconductors, involve the formation of very short-lived (≤ ten nanosec) paramagnetic states, which are not detectable either by continuous wave EPR (~ microsecond time scale) or pulsed EPR/spin echo techniques (tens of nanosecond resolution). The RYDMR experiment on the other hand, monitors the product that is usually much longer lived than the paramagnetic precursor state but detects it through an easily measured property e.g. its optical absorption. The experiment (Lersch and Michel-Beyerle 1989), as in time-resolved EPR, consists in irradiating resonant microwaves on to the sample during the lifetime of the paramagnetic state of interest. The effect of microwave irradiation is detected as a change of the product yield of some spin-selective reaction of the spin-correlated pairs. The virtue of the RYDMR technique is the effective decoupling of the stages of inducing microwave transitions and detecting the effect of microwaves.

This technique has been applied to: (i) semiconductors (Cavenett 1981), where it was found that the recombination rate of excess carriers can be influenced by changing their spin orientation (or that of paramagnetic recombination centre in a resonant microwave field) and (ii) polymers, to investigate the conductivity mechanism of weakly doped polyacetylene (Frankevich *et al* 1985).

14. Concluding remarks

It is hoped that this article has given a 'working knowledge' of the technique of electron paramagnetic resonance as applicable to advanced materials in their solid state. It is apparent that EPR is the 'method of choice' for the range of materials discussed — semiconductors to insulating and conducting polymers to ferroelectric and superconducting ceramics, and structural and optical glasses to optoelectronic and superionic materials — and more, to obtain information about an unpaired electron and its neighbourhood, and to relate it to the macroscopic behaviour. In the future the use of EPR technique for newer materials like multilayer, Langmuir–Blodgett films, ferrofluids to name a few, is being investigated, pushing the 'frontier' of technical parameters — frequency and magnetic field — to unbelievable limits in the quest for accuracy and detail in characterization.

Acknowledgements

I thank all my colleagues and students whose work has figured in this article. I particularly recall the Late Dr

S Subrahmanyam for many years of collaborative alytic activity.

st of Symbols

Isotropic hyperfine constant;

hyperfine structure tensor;

anisotropic hyperfine constant, sometimes dc magnetic field intensity;

Fine structure constant tensor;

energy, energy level;

; line shape function, function in general;

g-factor, g-tensor;

Gauss, g^2-tensor;

component of g-tensor;

nuclear g-factor;

, spin Hamiltonian;

dc magnetic field expressed as milli Tesla (mT) or Oersted or Gauss (10 Gauss = 1 mT);

microwave magnetic field;

, anisotropy field of ferromagnet;

n, demagnetization field of non-spherical ferromagnetic sample;

magnetic field at resonance, centre of ESR line;

nuclear spin operator, nuclear spin, intensity of ESR spectrum, current;

uniaxial anisotropic constant for amorphous ferromagnet;

components of direction cosine matrix;

magnetization vector;

magnetization along Z-axis;

electron spin quantum number, m_I nuclear spin quantum number;

N^-, Boltzmann population of levels;

transition probability, microwave power;

nuclear quadrupole moment, quality factor of cavity;

position vector;

alkyl radical;

saturation factor;

electron spin, electron spin operator;

spin-lattice relaxation;

T_2', spin-spin relaxation time;

11, transverse-electric mode of rectangular cavity, numbers refer to components along cavity dimensions (a, b c);

, W, coefficients of $g^2(\theta)$ function;

coordinate axis;

test sample, principal direction;

coordinate axis;

principal direction;

coordinate axis;

Z, circuit impedance, principal direction;

α, β, label for protons in a polymer;

γ, magnetogyric ratio;

δ, skin depth;

ΔH_{pp}, peak-to-peak width of the first derivative ESR signal;

ε, dielectric constant;

η, filling factor of cavity;

θ, angle between two vectors;

λ, spin-orbit coupling constant, microwave penetration depth, Gilbert damping factor in ferromagnetic resonance;

μ_B, Bohr magneton;

μ_e, electronic magnetic moment;

μ_N, nuclear magneton;

ν, microwave frequency, ENDOR transition frequency;

χ, magnetic susceptibility.

References

Abragam A and Bleaney B 1989 in *Electron paramagnetic resonance of transition ions* (New York: Dover)

Alger R S 1968 in *Electron paramagnetic resonance techniques and applications* (New York: Interscience)

Atherton N M 1973 in *Electron spin resonance* (Chichester: Ellis Horwood) Ch. 1

Badalyan A G and Zhitnikov R A 1985 *Sov. Phys. Solid State* **27** 1774

Bagguley D M S and Griffiths J H E 1950 *Proc. Phys. Soc.* **A201** 366

Balagopala Krishna C and Rajasekharan M V 1990 *Phys. Rev.* **B42** 7794

Balaya P and Sunandana C S 1990 *Solid State Ionics* **40/41** 770

Balaya P and Sunandana C S 1990 *Recent advances in fast ion conducting materials and devices* (eds) B V R Chowdari *et al* (Singapore: World Scientific) p. 535; 1994 *J. Phys. Chem. Solids* **55** 39

Bartl A, Frohner J, Znzok R and Roth S 1992 *Synth. Metals* **51** 197

Bartl A, Frohner J and Roth S 1993 *Synth. Metals* **55–57** 613

Bensimon Y *et al* 1992 *J. Non-Cryst. Solids* **149** 218

Beranov P G and Badalyan A G 1993 *Solid State Commun.* **85** 987

Berger R and Haddad M 1991 *Phys. Status Solidi* **b163** 463

Bhagat S M 1973 *Resonance methods of magnetic materials, Part II* (ed.) R F Bunshah (New York: Wiley) Vol. II

Bhagat S M, Manheimer M A and Moorjani K 1987 *Key Engg. Mater.* **13–15** 641

Bhat S V, Ganguly P, Ramakrishnan T V and Rao C N R 1987 *J. Phys. C: Solid State* **20** L559

Bishop S G, Strom U and Taylor P C 1977 *Phys. Rev.* **B15** 2278

Bowman R C Jr., Venturini E L and Witt S N 1987 *J. Vac. Sci. Tech.* **A5** 3171 and references therein

Bravo D, Martin A and Lopez F J 1993 *Solid State Commun.* **86** 281 and references therein

Bruker Almanac 1993 *Bruker spectrospin, Zurich*
Byszewski P, Jablonski R and Kolesnik S 1992 *Solid State Commun.* **84** 1111
Campbell D and Peterlin A 1968 *Polym. Letts* **6** 481
Canham L T 1990 *Appl. Phys. Lett.* **57** 1046
Caplan P I, Poindexter E H, Deal B E and Razouk R R 1977 *J. Appl. Phys.* **50** 5847
Carter F L (ed.) 1982/1987 *Molecular electronic devices I, II* (New York: Dekker)
Caurant D, Gourier D, Vivien D and Prasson M 1993 *J. Appl. Phys.* **73** 1657
Cavenett B C 1981 *Adv. Phys.* **30** 475
Chary K V R, Mahipal Reddy B, Nag N K, Subramanyam V S and Sunandana C S 1984 *J. Phys. Chem.* **88** 2622
Chen J, Chung T C, Moras F and Heeger A J 1985 *Solid State Commun.* **53** 757
Commoner B, Townsend J and Pake G E 1954 *Nature* **174** 689
Das R *et al* 1986 *Pramana–J. Phys.* **27** 661
Deville A *et al* 1993 *Phys. Rev.* **B47** 2840
Duke C B and Fabysh T T 1978 *J. Appl. Phys.* **49** 315
Dikanev S A and Ashtashkin A V 1978 in *Principles of magnetic resonance* (ed.) A J Hoff (Amsterdam: Elsevier) Ch. 2, p. 59
Doyle W T 1962 *Rev. Sci. Instrum.* **33** 118
Durny R 1980 *J. Non-Cryst. Solids* **41** 273
Einstein A and Ehrenfest P 1922 *Z. Phys.* **11** 31
Evora C and Jaccorino V 1977 *Phys. Rev. Lett.* **39** 1554
Feher G 1959a *Phys. Rev.* **114** 1219
Feher G 1959b *Bell. Syst. Tech. J.* **36** 449
Frankevich E L *et al* 1985 *Phys. Status Solidi* **B132** 283
Freed J H, Budil D K, Earle K A and Lynch W B 1989 *Advanced EPR* (ed.) A J Hott (Amsterdam: Elsevier) Ch. 8, p. 307
Furusawa M and Ikeya M 1990 *J. Phys. Soc. Jap.* **59** 2340
Fletcher R C, Yager W A, Pearson G L and Merrit F R 1954 *Phys. Rev.* **95** 844
Frait Z and Fraitova D 1988 *Spin waves and magnetic excitations* (eds) A S Borovik-Romonov and S K Sinha (Amsterdam: Elsevier) Ch. 1, p. 1
Furusawa M and Ikeya M 1991 *Jpn J. Appl. Phys.* **60** L1687
Gerlach W and Stern O 1924 *Ann. Phys. Leipzig* **74** 673
Gordon J P and Bowers K D 1958 *Phys. Rev. Lett.* **1** 301
Gorelkinskii Yu V and Nevinnyi N N 1987a *Pisma Zh. Tekh. Fiz.* **13** 105
Gorelkinskii Yu V and Nevinnyi N N 1987b *Sov. Tech. Phys. Lett.* **13** 45
Graham R A, Morosin B, Venturini E L and Carr M J 1986 *Ann. Rev. Mater. Sci.* **16** 315
Green R E Jr 1990 *Ann. Rev. Mater. Sci.* **20** 197
Griffiths J H E 1946 *Nature* **158** 67
Griscom D L 1973/74 *J. Non-Cryst. Solids* **13** 251
Griscom D L 1980 *J. Non-Cryst. Solids* **40** 211
Griscom D L, Stapelbroek M and Webb M J 1986 *J. Non-Cryst. Solids* **41** 329
Gunter P and Heiguard J P 1988/1989 *Photorefractive materials and their applications*, in *Topics 61 and 62 in applied physics* (Berlin: Springer Verlag) Vols I and II
Hagen W R 1992 *Adv. Inorg. Chem.* **38** 165
Hahn E L 1950 *Phys. Rev.* **80** 580
Haller E E and Falicov L M 1978 *Phys. Rev. Lett.* **41** 192
Hamanone K *et al* 1974 *J. Polymer Sci.* **A12** 1189
Harper W R 1964 *Contact and frictional electrification* (Oxford: Clarendon)
Hebard A *et al* 1991 *Nature* **350** 600
Henderson B and Gorrison A K 1973 *Adv. Phys.* **22** 423
Heniker J 1962 *Nature* **196** 474
Holczer K, Boucher J P, Devreux F and Nechtschien M 1981 *Phys. Rev.* **B23** 1051
Holton W C and Blum M 1962 *Phys. Rev.* **125** 89
Humphries G M K and McConnell H M 1982 *Methods of experimental physics* (eds) G Ehrenstein and H O Lecar (New York: Academic) Vol. 20, Ch. 2, p. 53
Hyde J S and Froncisz W 1989 *Advanced EPR, applications in biology and biochemistry* (ed.) A J Hott (Elsend) Ch. 7, p. 227
Ikeya M 1991 *Annu. Rev. Mater. Sci.* **21** 45
Ikeya M 1993 in *New applications of electron spin resonance, dating, dosimetry and microscopy* (Singapore: World Scientific Pub.)
Ikeya M, Megvo K, Miyamaru H and Ishii H 1991 *Appl. Mag. Res.* **2** 663
Isoya J *et al* 1990 *Phys. Rev.* **B41** 3905
Iwasaki M *et al* 1971 *J. Chem. Phys.* **54** 1839
Izumi T *et al* 1993 *Thin Solid Films* **228** 285
Janes R, Liu R-S, Edwards P P, Stevens A D and Symons M C R 1991 *J. Chem. Soc. Faraday Trans.* **87** 1209
Jones R, Janes R, Armstromy R, Pyper N C, Edward P P, Keeble D J and Harrison M R 1990 *J. Chem. Soc. Faraday Trans.* **86** 675
Kaul S N and Babu P D 1992 *Phys. Rev.* **B45** 295
Kaul S N and Siriguri V 1992 *J. Phys. Condens. Matter* **4** 505
Kausch H H 1978 *Polymer fracture* (Berlin: Springer Verlag) p. 119
Kawazo H, Watanabe Y and Yamane M 1987 *Diffusion Defect Data* **53–54** 189
Kazanskii V B 1976 *Proc. 6th int. congress on catalysis* (London: Chemical Society) Vol. 1, p. 50
Kindo K, Honda M, Kohashi T and Date M 1990 *J. Phys. Soc. Jap.* **59** 2332
Kip A F, Kittel C, Levy D H and Portis A M 1953 *Phys. Rev.* **91** 1066
Kiss E and Szorenyi T 1977 *Amorphous semiconductors* (ed.) I K Somogyi (Budapest: Akademiai Kiado) p. 25
Kittel C 1947 *Phys. Rev.* **71** 270
Kivelson S and Heeger A J 1985 *Phys. Rev. Lett.* **55** 3118
Kosaka M *et al* 1993 *Chem. Phys. Lett.* **203** 429
Koschnick F K, Rai M, Spaeth J M and Eachus R S 1993 *J. Phys. Condens. Matter* **5** 733
Koshta A A, Shvachko Yu N, Romanyukha A A and Ustinov V V 1993 *Zh. Eksp. Teor. Fiz.* **6** 629
Kubo N O *et al* 1992 *Appl. Phys. Lett.* **61** 940
Kwan C L and Yen T F 1979 *Anal. Chem.* **51** 1225
Lauterbur P C 1973 *Nature* **242** 190
Lebedev Ya S 1963 *J. Struct. Chem. (USSR)* **4** 22
Lersch W and Michel-Beyerle M E 1989 *Advanced EPR* (ed.) A J Hoff (Amsterdam: Elsevier) Ch. 19, p. 685
Loubser J H N and Van Ryneweld W P 1966 *Nature* **211** 517
Ludwig G W and Woodbury H H 1962 *Solid state physics* (eds) F Seitz and D Turnbull (New York: Academic) Vol. 13, p. 223
Mabbs F A and Collison D 1992 *Electron paramagnetic resonance*

of d transition metal compounds, in *Studies in inorganic chemistry* (New York: Elsevier) Vol. 16
rquardt C I 1976 *Appl. Phys. Lett.* **28** 209
suda K 1977 *Inst. Phys. Conf. Ser.* No. 31, (Bristol: Inst. Phys.) Ch. 2, p. 174
Millan J A 1974 in *Systematic materials analysis* (ed.) N L Peterson (New York: Academic Press) Ch. 7, Vol. 1, p. 193
Millan J A and Halpern T 1971 Argonne Natl. Lab. Rep. Phys.) ANL-7784
nran F and Anderson P W 1988 *Solid State Commun.* **67** 187
nring M *et al* 1993 *Proc. workshop on phase separation in cuprate superconductors, Erice, Italy* (eds) K A Muller and C Benedek (Singapore: World Scientific) p. 67
ns W B 1989 in *Advanced EPR* (ed.) A J Hoff (Amsterdam: Elsevier) Ch. 1, p. 1 and references therein
ns W B, Nassau K and McGee J D 1961 *Phys. Rev.* **123** 059
ami T, Ikeda Y and Tanaka M 1982 *J. Non-Cryst. Solids* **2** 15
amura H and Ikeya M 1993 *Appl. Radiat. & Isotopes* **44** 79
igaki K 1988 *Amorphous silicon and related materials* (ed.) Fritzsche (Singapore: World Scientific)
t N F 1968 *J. Non-Cryst. Solids* **1** 1
t N F 1971 *Adv. Phys.* **21** 785
dsky M H and Title R S 1961 *Phys. Rev. Lett.* **23** 581
ler K A *et al* 1980 *Phys. Rev. Lett.* **45** 832
ata T and Miki T 1993 *J. Appl. Phys.* **73** 1110
thy N R K and Sunandana C S 1992 *Solid state ionics: Materials and applications* (eds) B V R Chowdari *et al* Singapore: World Scientific) p. 357
rs S M *et al* 1992 *Rev. Mod. Phys.* **64** 559
ntschien M, Devreux F, Genoud F, Gugleelumi M and olezer K 1983 *Phys. Rev.* **B27** 61
o K 1982 *J. Magn. Reson.* **50** 145
n H *et al* 1992 *J. Phys. Soc. Jap.* **61** 2921
llis E J and Jeffries C D 1981 *Phys. Rev. Lett.* **45** 1859
elides S T 1988 *Amorphous silicon and related materials* d.) H Fritzsche (Singapore: World Scientific) p. 541
ninger S, Forrer J, Schweiger A and Weiland Th 1988 *Rev. Sci. Instrum.* **59** 752
row J R 1990 *Transition ion electron paramagnetic resonance* Oxford, London, New York: Clarendon Press)
e C P 1983 in *Electron spin resonance, A comprehensive treatise on experimental techniques* (New York: Interscience) nd ed.
enriede E 1989 *J. Phys. Condens. Matter* **1** 7267
I I *et al* 1939a *Phys. Rev.* **55** 526
I I *et al* 1939b *Phys. Rev.* **56** 728
vin B *et al* 1990 *Phys. Rev.* **B41** 769
asastry C and Sunandana C S 1976 *J. Magn. Res.* **23** 87
by B and Rabek J F 1977 *ESR spectroscopy in polymer research* (Berlin: Springer Verlag)
by B and Rabek J F 1977 *ESR spectroscopy in polymer research* (Berlin: Springer Verlag) Ch. VIII
K J and Rao B G 1985 *Proc. Indian Acad. Sci. (Chem. Sci.)* **95** 169
hart J F and Pereli J 1966 *Rev. Sci. Instrum.* **37** 426
M J 1979 *Phys. Lett.* **A71** 152
Rodriguez S 1987 *Physica* **B146** 212
Roitsin A B and Maevskii V M 1989 *Sov. Phys. Usp.* **32** 891
Roth L M, Lax B and Zwerdling S 1959 *Phys. Rev.* **114** 90
Rytz D *et al* 1990 *J. Opt. Soc. Am.* **B7** 2245
Sahyun M R V 1992 *Chemtech* 418
Sakaguchi M *et al* 1988 *J. Polym. Sci. Part B, Polym. Phys.* **26** 1307
Sakaguchi M *et al* 1989 *Macromolecules* **22** 1277 and references therein
Sakaguchi M, Shimada M and Kashiwabara H 1990 *Macromolecules* **23** 5038
Sakaguchi M, Yamakuchi T, Shimada S and Hon Y 1993 *Macromolecules* **26** 2612
Sakita S and Fujii I 1991 *Jpn J. Appl. Phys.* **30** L1489
Sands R H 1955 *Phys. Rev.* **99** 1222
Sariffici N S, Smilowitz L, Heeger A J and Wudl F 1992 *Science* **258** 1474
Schonland D S 1959 *Proc. Phys. Soc.* **73** 788
Scheffler M 1987 *Lattice relaxations at substitutional impurities in shallow impurity centre in semiconductors* (eds) A Boulder and R Resta (Amsterdam: North Holland) p. 171
Schweiger A 1989 *Advanced EPR* (ed.) A J Hoff (Amsterdam: Elsevier) Ch. 6, p. 243
Scripsick M P 1993 *J. Appl. Phys.* **73** 1114
Shimada H, Hon Y and Kashiwabara H 1988 *Macromolecules* **21** 2107
Shirakawa H and Ikeda S 1971 *Polym. J.* **2** 231
Sieverts E G and Ammerlaan C A J 1977 *Inst. Phys. Conf. Ser.* No. 31, Ch. 2, p. 213
Simon S and Al Nicula 1983 *J. Non-Cryst. Solids* **57** 23
Slichter C P 1955 *Phys. Rev.* **99** 479
Slichter C P 1978 in *Principles of magnetic resonance* (Berlin: Springer Verlag) 2nd ed., p. 38
Sozzani F, Di Silvestro G and Gervasini A 1986 *J. Polym. Sci. Part A: Polym. Chem.* **24** 815
Son N T, Kustov V E, Gregorkiewicz T and Ammerlaan C A J 1992 *Phys. Rev.* **B46** 4544
Spaeth J M and Koschnick F K 1991 *J. Phys. Chem. Solids* **52** 1
Spano M L and Bhagat S M 1981 *J. Magn. Magn. Mater.* **24** 143 and references therein
Stallinga P, Gregorkiewicz T, Ammerlaan C A J and Gorelkinskii Yu V 1993 *Phys. Rev. Lett.* **71** 117
Stern O 1921 *Z. Phys.* **7** 249
Stone T J, Buckman T, Nordio P L and McConnell H M 1965 *Proc. Natl. Acad. Sci. USA* **54** 1010
Stutzmann M and Street R A 1985 *Phys. Rev. Lett.* **54** 1836
Stutzmann M and Biegelson D K 1989 *Phys. Rev.* **B40** 9834
Stutzmann M, Biegelson D K and Street R A 1987 *Phys. Rev.* **B35** 5666
Sukei M, Eaton S S and Eaton G R 1993 *Appl. Radiat. & Isotopes* **44** 377
Sunandana C S 1975 in *ESR studies on some X-irradiated and doped sulphates*, Ph.D. Thesis, Indian Institute of Technology, Madras
Sunandana C S 1978 *Phys. Status Solidi* **A48** K19
Sunandana C S 1987 *Key Engg. Mater.* **13–15** 623
Sunandana C S and Bhatnagar A K 1984 *J. Phys. C: Solid State Phys.* **17** 467
Sunandana C S and Rao K S 1985 *Phys. Status Solidi* **A90** 681

Taylor P C, Baugher J F and Kriz H M 1975 *Chem. Rev.* **75** 203

Tinkham M 1996 *Introduction to superconductivity* (New York: McGraw Hill) 2nd ed.

Title R S and Chandrasekhar G V 1976 *Solid State Commun.* **20** 405

Vanheusden K and Stesmans A 1993 *Appl. Phys. Lett.* **22** 2405

Van Kemp R, Sieverts E G and Ammerlaan C A J 1987 *Phys. Rev.* **B36** 3528

Van Veen G 1978 *J. Magn. Reson.* **30** 91

Venugopal Rao G, Sunandana C S and Bhatnagar Anil K 1992 *J. Phys. Condens. Matter* **4** 1373

Von Bardeleben H J *et al* 1992 *Mater. Res. Symp. Proc.* (eds) G L Witt, R Calavu, U Mishra and U Weber (Philadelphia: Mater. Res. Soc.) Vol. 241, p. 69

Warren W L *et al* 1993 *Appl. Phys. Lett.* **62** 482 and references therein

Watanabe I, Inakagi Y and Shimizu T 1978 *J. Non-Cryst. Solids* **27** 295

Watkins G D, Kleverman M, Thilderkvist A and Grimmeiss H G 1991 *Phys. Rev. Lett.* **67** 1149

Webb E and Alexander H 1977 *Inst. Phys. Conf. Ser.* No. 31, Ch. 2, p. 266

Weeks R A 1956 *J. Appl. Phys.* **27** 1376

Wertz J E and Bolton J R 1972 in *Electron spin resonance, elementary theory and practical applications* (New York: McGraw Hill)

Whitmore M H 1993 *J. Chem. Phys.* **98** 3656

Wilmshurst T H 1967 in *Electron spin resonance spectrometer* (London: Hilger)

Winkler P F, Kleppner D, Myint T and Walther F G 1972 *Phys. Rev.* **A5** 83

Yasaitis E L and Smaller B 1953 *Phys. Rev.* **92** 1068

Yokomichi H and Morigaki K 1987 *Solid State Commun.* **63** 629

Yokomichi H and Morigaki K 1993 *Solid State Commun.* **85** 759

Yokomichi H, Takakuki H and Kondo M 1993 *Jap J. Appl. Phys.* **32** L365

Yordanov N D (ed.) 1991 in *Electron magnetic resonance of disordered systems* (*EMARDIS* 91) (Singapore: World Scientific)

Zakrevskii V A *et al* 1968 *Sov. Phys. Solid State* **10** 1341

Zavoiskii E K 1944 *Phys. Inst. Acad. Sci., Moscow*

Zhilinskaya E A, Valeev N K H and Oblasoe A K 1991 *J. Non-Cryst. Solids* **136** 76

Zhong Y C and Pilbrow J R 1991 *J. Magn. Res.* **93** 447

Zunger A 1986 *Solid state physics* (eds) F Seitz, D Turnbull and H Ehrenreich Vol. 39, p. 275

Note added in proof: The following developments have been most noteworthy — ever since this article was submitted. Among the techniques, electrical detection of EPR (B Stich *et al* 1995 *J. Appl. Phys.* **77** 1546), that measures the microwave/rf induced change of conductivity of semiconductors containing shallow and deep defects, offers new possibilities for the study of point defects. Such a study on a Si diode (Z Xiang and D J Miller 1995 *J. Appl. Phys.* **78** 4895) has identified broken bonds in a vacancy cluster acting as recombination centres. Bhat *et al* (S V Bhat, A Anand and Rajiv Bhat 1997 *Solid State Physics* (*India*) **40C** 62) have developed a spectrometer for unmodulated high-power rf absorption studies in high-temperature superconductors. Exciting applications include: study of spin-Peierls transitions in $Cu_{1-x}Zn_xGeO_3$ (P Fronzes *et al* 1997 *Phys. Rev.* **B56** 7827), low-temperature phase transitions in CuO by a DPPH probe (A M Suvarna and C S Sunandana 1997 *Physica* **C276** 65), defects in diamond films (A K Sikder *et al* 1997 *Solid State Physics* (*India*) **40C** 435), Ni^+ in $AgGaSe_2$ (L E Halliburton *et al* 1996 *J. Appl. Phys.* **79** 556), Cr-doped fluorochloro- and fluorobromozirconate glasses (J L Martinez *et al* 1997 *J. Phys. Cond. Matt.* **9** 9175) and studies of dangling bonds in porous silicon (Y Xiao *et al* 1994 *J. Appl. Phys.* **76** 1759; R Laiho and L S Vlasenko 1995 *J. Appl. Phys.* **78** 2857), besides a very interesting study of an oxygen defect centre associated with red photoluminescence from freshly etched and oxidized porous silicon (S M Prokos and W E Carlos 1995 *J. Appl. Phys.* **78** 2671). A comprehensive review of EPR in semiconductors has appeared (W Gehlhoff, M Hohne and J Schmidt 1992 in *Hyperfine interaction of defects in semiconductors* (ed.) G Langouche (Amsterdam: Elsevier) Chap. 5, p. 217).

. Mater. Sci., Vol. 21, No. 1, February 1998, pp. 71–75. © Printed in India.

possible crystallographic explanation for the five-fold diffraction mmetry in icosahedral phases

T R ANANTHARAMAN
Metals and Alloys Group, National Physical Laboratory, Dr K S Krishnan Road, New Delhi 110 012, India

MS received 16 December 1997

Abstract. X-ray and electron diffraction data from the Al–Cu–Fe icosahedral phase are compared and analysed on the basis of the microcrystalline and multi-domain model developed by the author. It is shown that a crystallographic explanation is now possible for both the enigmatic five-fold symmetry and non-periodicity of reflections observed in electron diffraction patterns of icosahedral phases.

Keywords. Crystallography; diffraction symmetry; icosahedral phases.

Introduction

discovery of quasicrystalline alloy phases (Schecht- *et al* 1984) displaying crystallographically disallowed -fold diffraction symmetry has generated a great deal xcitement, as also some confusion and controversy, ientific circles (Kelton 1993). One of the fundamental es raised by intensive researches on icosahedral and gonal quasicrystals relates to the limits of our ability listinguish through experiment between true quasi- tals and multi-twinned or multi-domain crystals with unit cells (Goldman and Kelton 1993). A further ortant recent development in this regard has been discovery of many so-called crystalline or rational oximants (see, for example, Liu 1993), which seem ave atomic arrangements in their rather large unit closely resembling the local atomic structure in icrystals.

arting with Field and Fraser (1985), many investi- rs (Carr 1986; Pauling 1985, 1987, 1988, 1990; chio and Williams 1988; Anantharaman 1989, 1990, , 1994a) have sought a conventional crystallographic anation for the quasicrystal phenomenon in terms of large unit cells or multi-twinned crystals. Interest ulti-twinned or multi-domain crystalline aggregates been revived in recent years by reports in their ur based on high-resolution single crystal synchrotron y studies of two thermodynamically stable and 'per- quasicrystals, e.g. Al–Cu–Fe icosahedral phase sch *et al* 1992) and Al–Cu–Co(–Si) decagonal phase weis *et al* 1993, 1994). As pointed out by Steurer 5) in his most recent review, practically all icrystals transform to crystalline phases at lower eratures or under high pressure, running through mediate phases with rather complicated and/or nano- in structures.

In this paper, X-ray and electron diffraction data from Al–Cu–Fe icosahedral phase is presented and analysed on the basis of the microcrystalline and multi-domain model developed by the author for both icosahedral and decagonal phases (Anantharaman 1993). A crystallographic explanation is thereby sought for the unusual five-fold symmetry and nonperiodicity of reflections observed in electron diffraction patterns of all icosahedral phases.

2. Experimental

Alloys with the nominal composition $Al_{65}Cu_{20}Fe_{15}$ were prepared by arc melting in purified argon atmosphere and then rapidly solidified by planar flow casting. The resulting ribbons (20–30 μm thick) were examined before and after annealing at 1073 K for 8 h in a Siemens Rotating Anode X-ray Diffractometer, using CuK_α or CoK_α monochromatic radiation. Transmission electron microscopic studies were also conducted in a JEOL JEM-200CX 200 kV Electron Microscope after thinning the ribbons by chemical means or by ion beam in a BAL-TEC RES 010 Rapid Etching System. As has been reported earlier (Ishimasa *et al* 1988; Liu 1993), the rapidly solidified ribbons were characterized by a homogenous icosahedral phase, while the annealed samples revealed also traces of the monoclinic $Al_{13}Fe_4$ phase. The two thinning techniques employed to produce specimens transparent to the electron beam did not make any difference to the electron diffraction data, as presented and analysed in this paper.

Table 1 presents results of an analysis of the first 32 Debye–Scherrer reflections with intensities of at least 1% of the strongest one from *i*–Al–Cu–Fe on the basis of the model proposed by the author (Anantharaman 1989, 1993, 1994b) for the multi-domain crystallization

of icosahedral and decagonal phases through nucleation from icosahedral atomic clusters in the concerned alloy melts. The orthorhombic unit cell built up of 96 orthorhombic basic cells with $a = 6a' = 1{\cdot}4868$ nm, $b = 4b' = 1{\cdot}6840$ nm and $c = 4c' = 1{\cdot}6024$ nm and belonging to the space group P_{mmm} (No. 47), as assigned here to *i*–Al–Cu–Fe, is quite similar to the ordered orthorhombic unit cells proposed earlier for *i*–Al–Mn, *i*–Al–Mn–Si, *i*–Al–Cu–Mg, *i*–Al–Cu–Li and *i*–Al–Cu–Ru phases. Depending on the actual composition, method of preparation and subsequent heat treatment, the parameters of the *i*–Al–Cu–Fe refined basic cell have been found to vary over a small range viz. $a' = 0{\cdot}248$–$0{\cdot}252$ nm; $b' = 0{\cdot}421$–$0{\cdot}429$ nm and $c' = 0{\cdot}400$–$0{\cdot}408$ nm. The agreement between calculated and observed interplanar distances (d_{hkl}) is extremely satisfactory in this case, the indices of all recorded reflections being significantly common to both face-centred cubic (fcc) and body-centred cubic (bcc) structures (table 1).

Table 1. Comparison of calculated and observed interplanar distances (d_{cal} and d_{obs} in nanometers) and observed relative intensities (I_{obs}) for Debye–Scherrer reflections from Al–Cu–Fe icosahedral phase.

No.	*hkl*	d_{cal}	d_{obs}	I_{obs}
1	020	0·842	0·833	2
2	220	0·557/		
3	202	0·545	0·551	3
4	040	0·421/		
5	004	0·401	0·415	3
6	042	0·373	0·374	13
7	420	0·340/		
8	402	0·337	0·339	15
9	224	0·325	0·324	12
10	440	0·279	0·280	3
11	600	0·248	0·245	7
12	602	0·237	0·238	3
13	444	0·229	0·229	2
14	604	0·211/		
15	080	0·211	0·211	94
16	642	0·206	0·206	2
17	624	0·204	0·204	2
18	008	0·200	0·200	100
19	644	0·189	0·188	1
20	428	0·173	0·173	3
21	448	0·163	0·162	2
22	088	0·145	0·145	13
23	0·10·6	0·143	0·142	4
24	10·44	0·132	0·133	1
25	22·12	0·130/		
26	848	0·130	0·130	1
27	12·00	0·124	0·124	36
28	12·42	0·118	0·117	2
29	12·80	0·107	0·107	20
30	12·08	0·105/		
31	0·16·0	0·105	0·105	15
32	00·16	0·100	0·100	1

Unit cell: Orthorhombic	$a = 1{\cdot}4868$ nm
Space group: P_{mmm} (No. 47)	$b = 1{\cdot}6840$ nm
I_{obs}: Rounded to integers	$c = 1{\cdot}6024$ nm

(Weak reflections with I_{obs} less than 1·0 are not included).

Table 2 contains an analysis of the selected area electron diffraction pattern of *i*–Al–Cu–Fe, displaying the well-publicized and much-discussed five-fold symmetry first observed in *i*–Al–Mn (Schechtman *et al* 1984) and subsequently in many other icosahedral phases. Among over 200 reflections or spots recorded in this pattern, it could be noted that 130 reflections are equally distributed in 10 rows, each row starting from the origin and displaying an angle of 36° to its neighbours on either side. Their interplanar distances (d_{hkl}) were calculated from several rows of reflections and from many diffraction patterns of *i*–Al–Cu–Fe with differing camera lengths. The reliable and reproducible averages of the observed d_{hkl} values for a row of reflections are recorded in column 2 of table 2, their relative intensities (I_R) being shown in column 3. The nonperiodicity of the diffraction spots in such patterns has generally been explained on the basis of the so-called Fibonacci sequence, viz. 2, 3, 5, 8, 13, 21, etc. Columns 4 and 5 of table 2 attempt an analysis of the concerned d_{hkl} values on this basis and show that there is considerable deviation between the estimated and observed values in case of the low-angle reflections.

The X-ray evidence in table 2 studied along with the proposal in the author's multi-domain model for the emergence of five-fold diffraction symmetry in icosahedral phases (see Anantharaman 1994b), as illustrated in figure 1, brings out some very significant and interesting features (see column 6 of table 2) of the five-fold electron diffraction patterns of *i*–Al–Cu–Fe. Based on the [110] zone for one orientation, the very strong 008 reflection along with its rather weak second order companion, i.e. 00·16 reflection, appears as expected in every one of the ten rows of reflections, but the only other reflection that can be identified from X-ray patterns is 224, along with its second order, i.e. 448. The latter pair actually comes from a crystal (or domain) with a different orientation, inclined 72° to the original crystal, and appears on this line or row only because the angle between 001 and 112 crystallographic planes in this orthorhombic phase works out to almost exactly 36°. No other reflection on this row can be identified in the concerned Debye–Scherrer patterns. Of course the observed d_{hkl} values of two electron reflections, viz. 0·144 nm and 0·123 nm, have their counterparts in the X-ray pattern, viz. 0·145 nm for 088 and 0·124 nm for 12·00, but these two reflections cannot possibly appear in the [110] zone under consideration.

As regards the 9 electron reflections in each row, that are not accounted for in the Debye–Scherrer patterns, the last column of table 2 brings out the real reason for their appearance, viz. they are all caused by dynamic

able 2. Analysis of a representative set from the ten identical rows of reflections in the electron diffraction pattern of AlCuFe osahedral phase.

o.	d_{hkl} observed	I_R	hkl_F	d_{hkl} calculated	X-ray evidence	Double diffraction possibility
	0·850	w	002	0·801	not observed	0·527 + 0·324 = 0·851
	0·527	m	003	0·534	not observed	0·324 + 0·200 = 0·524
	0·324	s	005	0·320	observed, d_{224} = 0·324	not called for
	0·261	vw	006	0·267	not observed	0·162 + 0·100 = 0·262
	0·234	vw	007	0·229	not observed	0·145 + 0·090 = 0·235
	0·200	vs	008	0·200	observed, d_{008} = 0·200	not called for
	0·162	vw	00·10	0·160	observed, d_{448} = 0·162	not called for
	0·144	vw	00·11	0·146	not observed	0·234 − 0·090 = 0·144
	0·123	s	00·13	0·123	not observed	0·324 − 0·200 = 0·124
	0·100	m	00·16	0·100	observed, $d_{00\cdot16}$ = 0·100	not called for
	0·090	m	00·18	0·089	no data	0·234 − 0·145 = 0·089
	0·076	s	00·21	0·076	no data	0·200 − 0·123 = 0·077
	0·062	s	00·26	0·062	no data	0·162 − 0·100 = 0·062

= Relative observed intensity; vw = very weak; w = weak; m = medium; s = strong; vs = very strong, hkl_F = indices based on e Fibonacci sequence; d_{hkl} = values in nanometers).

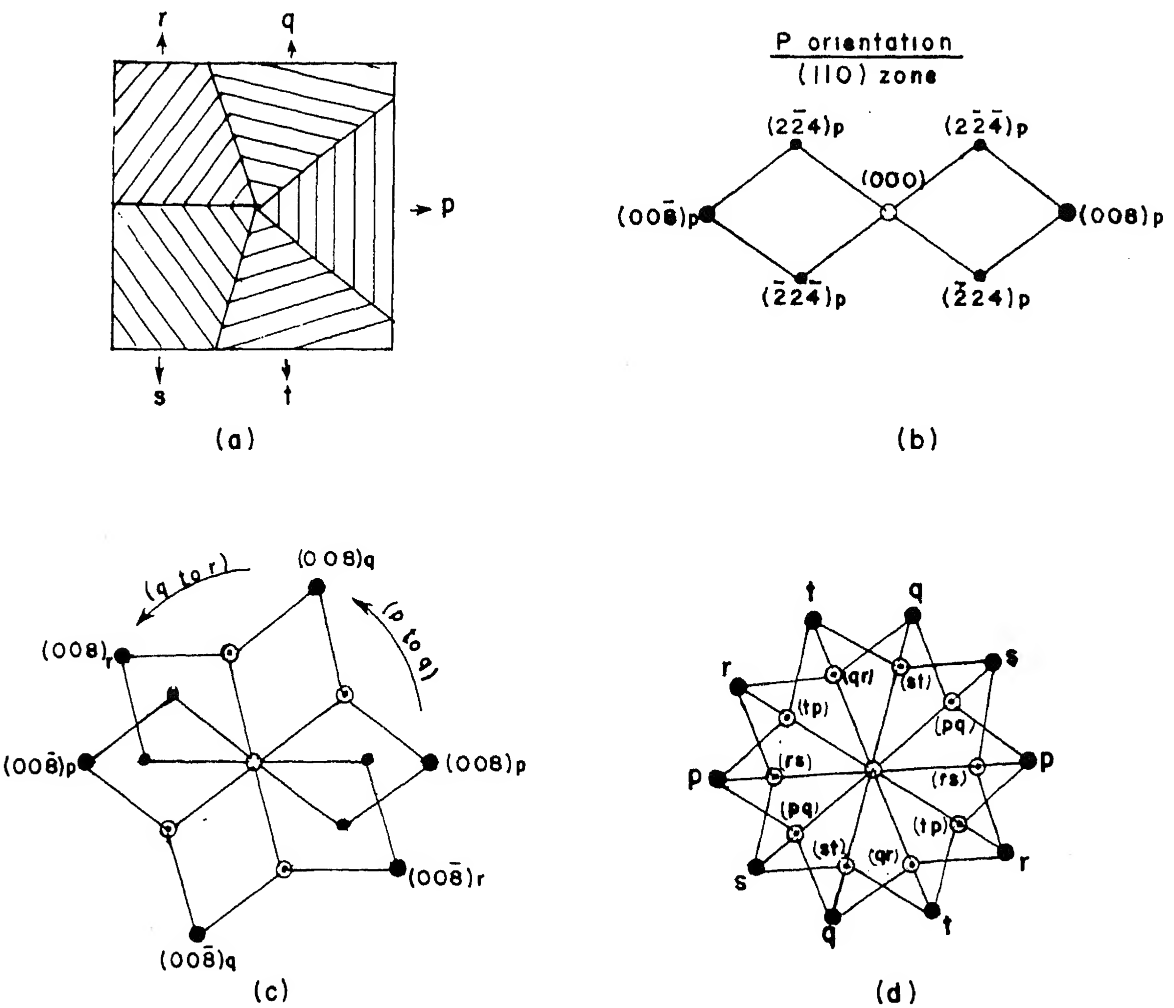

gure 1. Emergence of the five-fold electron diffraction pattern of an icosahedral phase prior to double diffraction. (a) Five entations of the same crystal (p, q, r, s and t) with 72° angular relationships between them, (b) single crystal diffraction ttern: [110] zone, "p" orientation, (c) impact of two other orientations (q and r) on (b), and (d) diffraction pattern generated all five (p, q, r, s and t) orientations before double diffraction.

double diffraction, a phenomenon known for long to cause extra spots in electron diffraction patterns. In fact, computer simulation has earlier been used to confirm the emergence of such extra reflections due to double diffraction in icosahedral phases (Field and Fraser 1985; Anantharaman 1989). It is relevant to add here that in this case actual experimental demonstration, through dark field characterization and tilting, of the occurrence of extra reflections due to double diffraction is extremely difficult, if not impossible, because of the complex multi-domain structure assigned to such phases.

3. Discussion of results

In the present work, perhaps for the first time, a careful and detailed analysis has been undertaken of both X-ray and electron diffraction patterns from the same icosahedral phase on the basis of a crystallographic model. The observed five-fold diffraction symmetry is shown to be caused by one very strong reflection (along with its second order) from a crystal of the icosahedral phase with a particular orientation and another not so strong reflection (along with its second order) from the same type of crystal, but with a 72° orientation relationship with the former. These four electron spots in each of the ten rows of spots radiating or spreading out from the origin at 36° intervals are shown to generate another nine spots by dynamic double diffraction. Thus 130 electron reflections get recorded in ten rows of the diffraction pattern through just two reflections, one each from two orientations, 72° to each other! In fact, many other reflections in the diffraction patterns can also be explained as only due to double diffraction from these four reflections.

The nonperiodicity and Fibonacci sequence, associated with the electron reflections in such patterns for nearly a decade, can thus be seen to arise out of some extraordinarily unusual circumstances related to the icosahedral phases, viz. the geometry of the unit cell leading to an angle of 36°, i.e. half of 72°, between the 001 and 112 planes, the emergence of five 72° orientations of the crystal due to random changes in direction during its growth and the fortuitous closeness between the 224 and 005 interplanar distances (0·324 nm and 0·320 nm, respectively). Further, such a five-fold pattern is not generated by the 800 and 080 reflections since the concerned crucial angular relationships viz. between 800 and 422 in the [011] zone and between 080 and 242 in the [101] zone, work out to 33° and 38°, respectively, and not 36°. Incidentally, the 800 reflection does not appear in the X-ray pattern, but 12·00 does (see table 1). It is relevant to report here that the extraordinary role of unit cell geometry in causing five-fold electron diffraction has recently been highlighted in case of a well-known crystalline phase viz. orthorhombic $Al_{13}Fe_4$ (Ellner 1995).

It is appropriate to record here that the lattice parameters of *i*–Al–Cu–Fe may well be higher than the values used in the present analysis, depending on the appearance and identification of further weak Debye–Scherrer reflections at very low Bragg angles. In fact, a much larger rhombohedral unit cell has already been proposed (Motsch *et al* 1992) for *i*–Al–Cu–Fe with $\gamma = 3{\cdot}208$ nm and $\alpha = 36°$ on the basis of high resolution synchrotron X-ray studies of this phase. This unit cell can be converted to the orthorhombic system with $a = 1{\cdot}983$ nm; $b = 3{\cdot}434$ nm and $c = 8{\cdot}978$ nm. On the basis of the author's model, these parameters work out to $8a'$, $8b'$ and $22c'$, respectively, allowing for the slight differences in chemical composition of the two alloys concerned. So long as the proposed unit cells constitute superstructures of the small basic orthorhombic cell identified in the author's model (Anantharaman 1994b), as shown in this case, the present analysis can be applied convincingly and with the same conclusions to all icosahedral phases, albeit with different and numerically higher indices for the crucial 008 and 224 reflections.

Acknowledgements

The experimental work described above was carried out during a six-week visit to the Institute for Solid State and Materials Research, Dresden, Germany. Author thanks Mr R Rennekamp of this Institute's Electron Microscopy Division, for his valuable assistance in thinning and mounting specimens, as also examining them in the electron microscope. He also thanks Prof. H Warlimount, Scientific Director, Dr H D Bauer, Head, Electron Microscopy Division, and Dr N Mattern, Head, X-ray Crystallography Division, of this Institute for their encouragement and support. He is indebted to the Director General, Council of Scientific and Industrial Research, New Delhi for nominating him on an Indo–German Exchange Programme for this Research Visit to Dresden.

References

Anantharaman T R 1989 *Curr. Sci.* **58** 1057

Anantharaman T R 1990 *Quasicrystals and incommensurate structures in condensed matter* (eds) M J Yacaman, D Romeu, V Castano and A Gomez (Singapore: World Scientific) p. 199

Anantharaman T R 1993 *Scr. Met. Mater.* **28** 1555

Anantharaman T R 1994a *Experimental methods of phase diagram determination* (eds) J E Morral, R S Schiffman and S M Merchant (USA: TMS) p. 173

Anantharaman T R 1994b *Bull. Mater. Sci.* **17** 717

Carr M J 1986 *J. Appl. Phys.* **59** 1063

Ellner M 1995 *Acta Cryst.* **B51** 31

Fettweis M, Launois P, Denoyer F, Reich R, Godard J M and Lambert M 1993 *J. Non-Cryst. Solids* **153/154** 24

Fettweis M, Launois P, Denoyer F, Reich R and Lambert M 1994 *Phys. Rev.* **B49** 15573

eld R D and Fraser H L 1985 *Mater. Sci. Eng.* **68** L17
ldman A I and Kelton K J 1993 *Rev. Mod. Phys.* **65** 213
imasa T, Fukano Y and Tsuchimori M 1988 *Philos. Mag. Lett.* **58** 157
lton K F 1993 *Int. Mater. Rev.* **38** 105
W 1993 *Fortschritt-Berichte VDI Reihe 5*, No. 300
tsch T, Denoyer F, Launois P and Lambert M 1992 *J. Phys. France* **2** 861
ling L 1985 *Nature* **317** 512
Pauling L 1987 *Phys. Rev. Lett.* **58** 365
Pauling L 1988 *Proc. Natl. Acad. Sci.* **85** 8276
Pauling L 1990 *Proc. Natl. Acad. Sci.* **87** 7849
Schechtman D, Blech I, Gratias D and Cahn J W 1984 *Phys. Rev. Lett.* **53** 1951
Steurer W 1996 *Physical metallurgy* (eds) R W Cahn and P Haasen (Elsevier Science BV) 4th ed., p. 372
Vecchio K S and Williams D B 1988 *Metall. Trans.* **A19** 2875

. Mater. Sci., Vol. 21, No. 1, February 1998, pp. 77–80. © Printed in India.

eparation of superconducting-grade copper from commercial ade copper salt

P PRAMANIK*, A K ADAK and A PATHAK

Department of Chemistry, Indian Institute of Technology, Kharagpur 721 302, India

MS received 31 May 1997; revised 28 October 1997

Abstract. Fine samples with nominal composition of $Bi_{1.6}Pb_{0.4}Sr_2Ca_2Cu_3O_x$ have been produced by solid state method using various purity grades of starting copper oxide powder. Studies on T_c and high-T_c volume fraction measurements of these samples revealed that the samples produced using CuO powders obtained in laboratory after double purification of the commercially available copper salts have higher T_c (104·46 K) and increased percentage of high T_c volume fraction (58%) compared to even the samples prepared from Aldrich grade (99·99%) CuO. A simple and cost-effective chemical route for the purification of CuO from commercially available copper salts has been outlined.

Keywords. Superconductor; high purity copper; chemical purification.

Introduction

since the discovery of superconductivity in vskite ceramics (Bednorz and Muller 1986) and later nsion of this discovery (Wu *et al* 1987), there have large-scale research efforts in this direction the d over. The voluminous research publications in this stand testimony to the global urge to understand realize the potentials of these ceramic super-uctors. Huge chunks of research funds worldwide continuously being directed towards the large-scale uction of ceramic superconductors having high critical nt density (J_c) and transition temperature (T_c) into uperconducting phase.

search into the basic chemistry of these materials continuing as improvements on the superconducting erties are being sought for. However, some ralizations can now be made for these materials g to the consistent replication of findings. One such ralized finding is that in all copper oxide based nics, the pairing of carriers in the Cu–O_2 planes responsible for their high (T_c) superconductivity scon *et al* 1987). Thus any substitution on the er site of these materials, which alters the electronic tures of the Cu–O_2 plane, would tend to strongly ss their (T_c) (the transition temperature into the conducting phase or the zero resistance temperature) he volume fraction of the high (T_c) superconducting : (Jones *et al* 1989). Therefore, impurities, particu- the transition metals (3*d*), which have the requisite cies and ionic radii would tend to replace copper e Cu–O_2 planes and detriment the superconducting properties (Ginsberg 1989; Maeda *et al* 1990). As a consequence, the purities of the starting materials, particularly the copper salts, used in the preparation of these ceramic superconductors, is expected to play a major role in obtaining a high T_c phase-pure product.

In this paper, we deal with the $Bi_{1.6}Pb_{0.4}Sr_2Ca_2Cu_3O_x$ ceramic superconductor system which is constituted of (2223) phase with T_c at 110 K, the (2212) phase with T_c at 80 K, and the (2201) phase with T_c at 20 K. To increase the critical current density (J_c) above liquid nitrogen temperature, it is important to increase the volume fraction of the high T_c phase (i.e. the (2223) phase with T_c at 110 K) and decrease that of the other phases. Here, we report results of the investigations on the effects of purity of the starting copper oxide on T_c and the volume fraction of the high T_c superconducting phase. We also report a cost-effective chemical route for the preparation of high purity grade (≥ 99·99%) copper oxide from commercially available copper salts.

2. Experimental

Five different grades of copper oxide powders were used for the preparation of $Bi_{1.6}Pb_{0.4}Sr_2Ca_2Cu_3O_x$ samples. The copper oxide powders used were: (i) Copper oxide (98%) supplied by LOBA Chemie, India, (ii) Copper oxide (98%) supplied by S.D. Fine Chemicals, India, (iii) Laboratory (single) purified copper oxide from commercially available copper chlorides/sulphates, (iv) Laboratory (double) purified copper oxide from single purified copper and (v) Aldrich grade (99·99%) copper oxide.

The $Bi_{1.6}Pb_{0.4}Sr_2Ca_2Cu_3O_x$ samples prepared using each of the five mentioned grades of copper oxide powders

:esponding author

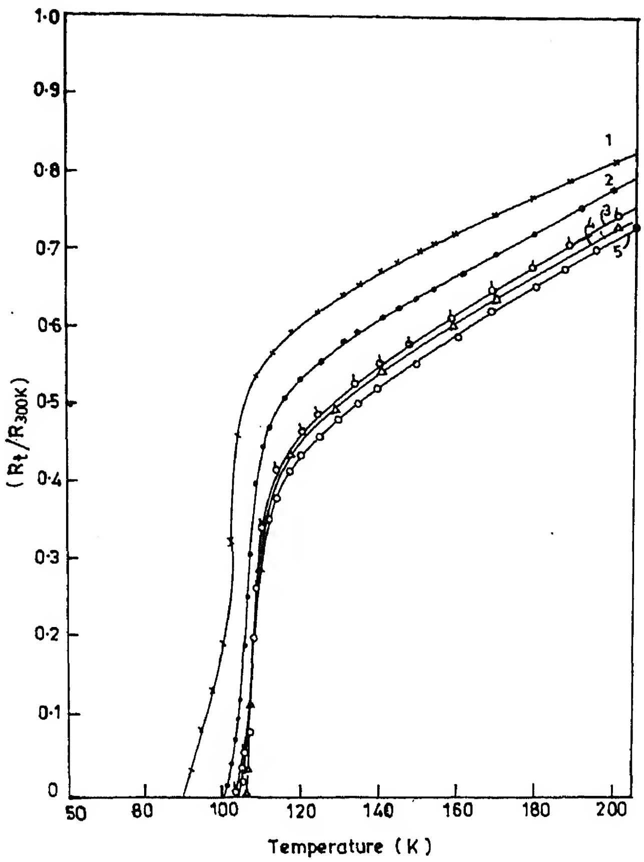

Figure 1. Resistance (Rt/R_{300}) vs temperature (K) plots for $Bi_{1.6}Pb_{0.4}Sr_2Ca_2Cu_3O_x$ samples prepared from CuO: (1) LOBA Chemie, (2) S.D. Fine Chemicals, (3) Laboratory single purification, (4) Laboratory double purification and (5) Aldrich.

are referred to in the text as samples 1, 2, 3, 4 and 5, respectively.

2.1 *Sample preparation*

Stoichiometric amounts of each of these copper oxides were separately taken and mixed with the required amounts of Bi_2O_3, PbO, $SrCO_3$ and $CaCO_3$. The mixed compositions were then calcined in air at 820°C for 24 h. On cooling, the powders were intimately mixed and again calcined in air at 820°C for 24 h. On cooling each of the powder compositions were pulverized and pressed into pellets. The pellets were finally sintered at 840°C for 100 h in an atmosphere of $O_2 : N_2 = 1 : 10$.

The resistance for each of the pellets were measured by a.c. method using a lock-in-amplifier by the standard four-probe contact method. The temperatures were recorded using a Cu-const thermocouple. The measurement of the (2223) phase volume fraction for each of the pellets were also carried out using a lock-in-amplifier.

2.2 *Purification of copper oxide powders*

To get single purified CuO, the commercially available copper sulphates (or, chlorides), with purity <98%, was dissolved in distilled water and complexed with sodium–potassium tartrate (Rochelle salt) in presence of optimum amounts of sodium hydroxide and sodium carbonate. The solution was filtered (to get rid of any turbidity or, suspended impurities) so as to get a clear blue coloured filtrate. The filtered solution then refluxed with 40%

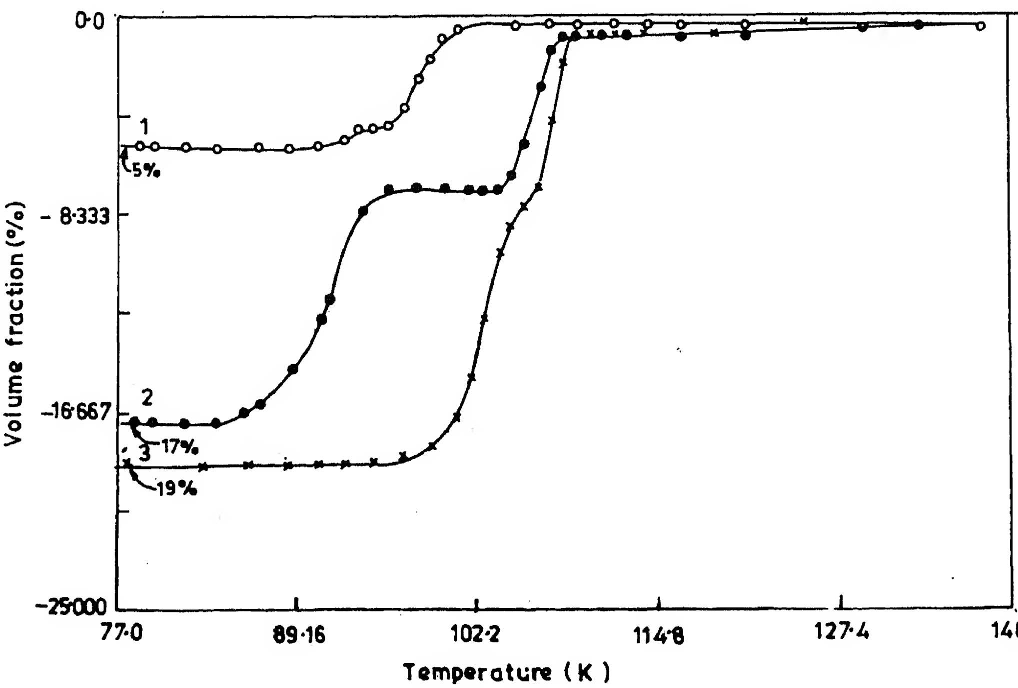

Figure 2. High T_c volume fraction (percentage) vs temperature (K) plots for $Bi_{1.6}Pb_{0.4}Sr_2Ca_2Cu_3O_x$ samples prepared from CuO: (1) LOBA Chemie, (2) S.D. Fine Chemicals and (3) Laboratory single purification.

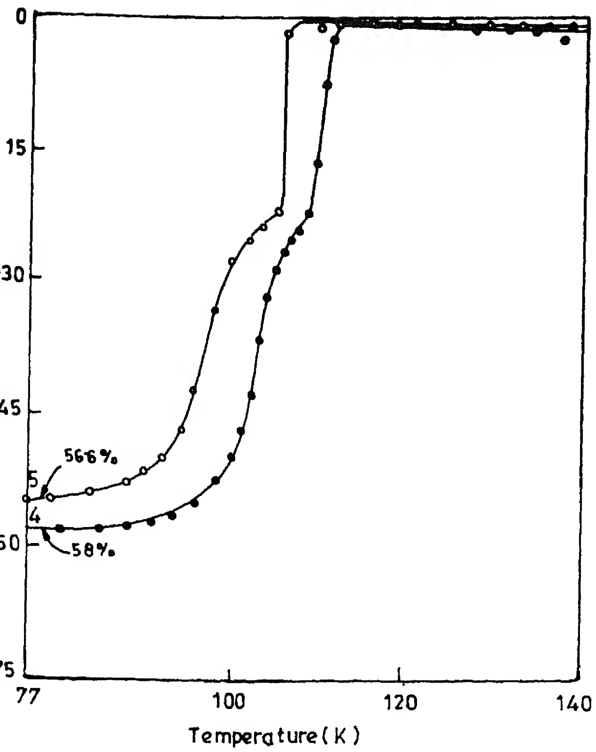

re 3. High T_c volume fraction (percentage) versus temure (K) plots for $Bi_{1.6}Pb_{0.4}Sr_2Ca_2Cu_3O_x$ samples prepared CuO: (4) Laboratory double purification and (5) Aldrich.

formaldehyde (with ratio 5 : 1) over a water bath. Reddish metallic copper precipitated within 10–15 min of refluxing. The metallic copper was then separated and dried with acetone. Calcination (in air) at 400°C for 3 h, of the metallic copper gave the single purified CuO powder.

To obtain double purified CuO, the precipitated copper mentioned above was dissolved in chlorine water and the entire process from separation of copper from the solution to calcination in air was repeated.

3. Results and discussion

The fall of resistance with temperature were recorded for each of the $Bi_{1.6}Pb_{0.4}Sr_2Ca_2Cu_3O_x$ compositions prepared from varied purity of CuO and are depicted in figure 1. From the measurements, it was observed that the sample prepared from LOBA Chemie grade CuO (i.e. sample 1) had the lowest T_c ($R = 0$) while the sample from double purified CuO (i.e. sample 4) and Aldrich CuO (i.e. sample 5) had higher and comparable T_c values. The fall in resistance with temperature (figure 1) in the case of samples 1 and 2 were not very sharp, reflecting the presence of phases other than the (2223) as the major phase. On the other hand, relatively sharper fall in resistance in samples 3, 4 and 5 were indicative of the realization of the (2223) as the major phase.

The details of the volume fraction of the (2223) phase for the various $Bi_{1.6}Pb_{0.4}Sr_2Ca_2Cu_3O_x$ samples are

Table 1. T_c ($R = 0$) and percentage volume-fraction of the (2223) phase for various samples of $Bi_{1.6}Pb_{0.4}Sr_2Ca_2Cu_3O_x$.

Sample	Source of CuO	T_c	Percentage volume fraction
1	LOBA Chemie, India (98%)	89·30 K	5·0%
2	S.D. Fine Chemicals (98%)	99·20 K	17·0%
3	Single purified	102·98 K	19·0%
4	Double purified	104·46 K	58·0%
5	Aldrich Grade (99·99%)	104·44 K	56·6%

Table 2. Analysis of the impurities present in the various grades of CuO powder.

Impurity	Percentage present: LOBA Chemie	S.D. Fine Chemicals	Single purified	Double purified	Aldrich
Fe	0·1321	0·0580	0·0120	0·0020	0·0030
Zn	1·4250	0·0355	0·0246	0·0052	0·0040
Ni	0·0525	0·0135	0·0221	0·0060	0·0060
Co	0·0932	0·0162	0·0047	0·0032	0·0030
Mn	0·0324	0·0021	Not detectable		
Cr	0·0201	0·0020	Not detectable		
Se	0·0943	0·0240	< 0·001		
Te	0·0762	< 0·001			

represented in figures 2 and 3. The formation of steps in the volume fraction versus temperature curves are manifestations of the presence of (2212) phase along with (2223) phase. From figure 2, it is conclusive that in sample 1 very little of the (2223) phase exists in the sample. The striking feature of figure 3 reveals that the sample 4, prepared from double purified CuO, has a higher percentage volume-fraction of the (2223) phase compared to that of sample 5, which was prepared from Aldrich-grade (99·99%) CuO.

The T_c ($R=0$) values and their respective percentage volume-fraction of the (2223) phase for the various samples of $Bi_{1\cdot6}Pb_{0\cdot4}Sr_2Ca_2Cu_3O_x$, prepared from various grades of CuO are summarized in table 1.

The atomic absorption data for the various grades of CuO powders revealed the presence of Zn, Ni, Fe and trace amounts of Co, Se and Te as trace impurities. The impurities present were the maximum for the CuO powders supplied from the LOBA Chemie, India while it was the minimum for the double purified CuO. The analysis of impurities present in double purified CuO determined by automic absorption spectroscopy (AAS) is given in table 2. The order of increase of purity in CuO powders were as follows:

LOBA Chemie < S.D. Fine Chemicals < Single purified ≪ Aldrich–Grade ≤ Double purified.

Presence of impurities, such as Zn, Ni and Fe, in the starting CuO powders provided scope for their substitution for the Cu sites. With increased levels of impurities their chances of replacing Cu in the Cu sites were increased and the electronic structure of the Cu–O_2 plane was expected to get altered. Consequently, the T_c values and the percentage volume fraction of the (2223) phase got depressed.

Supplementing with the atomic absorption data, it can be concluded that higher purity of the starting CuO leads to higher values of T_c and increased volume fractions of high T_c phase. It can also be concluded that double purification of copper oxide by simple chemical route indeed leads to a better superconducting final material. The chemical route used for single and double purification requires commonly available and less costly chemical reagents such as formaldehyde, sodium–potassium tartrate, NaOH and Na_2CO_3 thus making the route cost-effective for large scale production of high-purity copper oxide.

References

Bednorz J G and Muller K A 1986 *Phys. B: Condens. Matter* **64** 189

Ginsberg D M 1989 *Physical properties of high temperature superconductors 1* (Singapore: World Scientific)

Jones T E, Thibado P M, McGinnes W C, Boss R D, Schindler J W and Oseroffs S 1989 *Physica* **C162** 25

Maeda A, Yabe T, Tukebayashi S, Hase M and Uchinokura K 1990 *Phys. Rev.* **B41** 4112

Tarascon J M *et al* 1987 *Phys. Rev.* **B36** 8393

Wu M K *et al* 1987 *Phys. Rev. Lett.* **58** 908

. Mater. Sci., Vol. 21, No. 1, February 1998, pp. 81–86. © Printed in India.

eparation of tetragonal zirconia powders by a solid state reaction: netics, phases and morphology

V V MISHRA, A K GARG and D C AGRAWAL*
Materials Science Programme, Indian Institute of Technology, Kanpur 208 016, India

MS received 18 February 1997; revised 7 November 1997

Abstract. Powders of tetragonal (t)ZrO_2 have been prepared by a solid state reaction between sodium metazirconate and sodium metaphosphate. The reaction temperatures and times have been varied between 450 and 550°C and 5 and 75 h, respectively. Zirconia powder, mostly in the t and t' phases, is obtained. The yield of ZrO_2 powder increases monotonically with time at all reaction temperatures according to a phase boundary controlled kinetics. The fraction of t phase also increases with time at 450°C and 500°C but goes through a maximum at 550°C, the highest temperature employed. A maximum of 55% of the precursor monoclinic zirconia (used to prepare sodium meta zirconate) is converted to t phase at 500°C/75 h. The ZrO_2 powder consists of crystallites of size 9–25 nm agglomerated into particles having average size between 2 and 4 μm. The agglomerates have a breaking strength of 100 MPa. A hydrothermal treatment is found to break the agglomerates into smaller sizes. Grinding the powder in a mortar and pestle converts only 12% of the t phase into monoclinic, indicating that substantial fraction of the tetragonal phase is the non transformable variety t'. Heating experiments also confirm this.

Keywords. Tetragonal zirconia; powder preparation; solid state reaction.

ntroduction

etragonal (t) to monoclinic (m) phase transformation irconia (ZrO_2), accompanied by 3–5% volume ision and 8% shear strain, is utilized in toughening amics. The stable phase of ZrO_2 at room temperature noclinic but the tetragonal phase can be stabilized particle size is very small or if ZrO_2 is alloyed Y_2O_3, CeO_2 etc. Ultrafine t-ZrO_2 powders have successfully prepared by a variety of methods diyasni *et al* 1967; Haberko *et al* 1975; Brook Rhodes 1981; Kagawa *et al* 1983; Jean 1991; t *et al* 1992; Suzuki *et al* 1992; Maher *et al* 1993). son *et al* (1987) briefly reported some years ago er simple method for preparation of t-ZrO_2 powders g a crystallite size of ≃ 13 nm by a solid state on between sodium metazirconate (Na_2ZrO_3) and n hexa metaphosphate $(NaPO_3)_6$ at relatively low rature (500°C). The method converts coarse m-ZrO_2 e t-ZrO_2 in a two-step process: first the precursor O_3 is prepared from coarse m-ZrO_2 and subsequently solid state reaction between Na_2ZrO_3 and $(NaPO_3)_6$, -ZrO_2 powder is obtained. The t-ZrO_2 particles are ved to be agglomerated but are expected to break er particles during compaction. No further study is preparation route has been reported.

s appeared to be an attractive process for preparation of t-ZrO_2. We have therefore explored it further in this work, by conducting experiments under varying preparation conditions to optimize the yield of t-ZrO_2 powders. Objectives of this work were to study the kinetics of the solid state reaction and to ascertain the phases and preparation of the powder. Possibility of breaking the agglomerates by hydrothermal treatment and under compaction has also been studied. A key property of t-ZrO_2 is its ability to undergo $t \rightarrow m$ transformation in a stress field and the extent to which it is effective in enhancing toughness. An attempt has been made to evaluate these parameters also.

or for correspondence

2. Experimental

The preparation method used here is essentially the same as described by Harrison *et al* (1987). A solid state reaction between Na_2ZrO_3 and $(NaPO_3)_6$ proceeds as follows

$$Na_2ZrO_3 + 1/6(NaPO_3)_6 \xrightarrow{500^\circ C} ZrO_2 + Na_3PO_4. \quad (1)$$

The precursor Na_2ZrO_3 for the above reaction was prepared by calcining a pellet of an equimolar mixture of m-ZrO_2 (1–2 μm size, Indian Rare Earths, Kerala) and Na_2CO_3 (Laboratory grade, Glaxo Laboratories, Bombay) at 1250°C for 90 min. The equimolar quantities of Na_2ZrO_3 and $(NaPO_3)_6$, (predried at 150°C) were

mixed and ground in an agate mortar and pestle for 30 min and held in a Pt crucible at temperatures of 450°C, 500°C and 550°C for times ranging from 5 h to 75 h. Na_3PO_4 was removed from the reaction product by leaching with dilute HNO_3 (5 N) four times. The residue was washed with triple distilled water (4 to 5 times). Some unknown intermediate phase, besides zirconia, insoluble in HNO_3 was noticed, particularly in powders prepared at lower reaction times. This phase was removed by a further leaching with 1·5% HF solution for 10 min. The residual powders were again washed by triple distilled water followed by ethyl alcohol, dried at 60°C and weighed for determining yield of reaction. The phases present in the resulting ZrO_2 powder and their respective amounts were determined by X-ray diffraction (XRD) using a diffractometer (Reich Siefert 150 Debyeflex 2002) with CuKα radiation. The monoclinic volume fraction (V_m) was determined by the polymorph method as modified by Toraya *et al* (1984)

$$V_m = \frac{PX_m}{1+(P-1)X_m}. \tag{2}$$

where $P = 1{\cdot}31$, a constant factor to account for non-linearity and X_m the integrated intensity ratio,

$$X_m = \frac{I_m(11\bar{1}) + I_m(111)}{I_m(11\bar{1}) + I_m(111) + I_t(111)}, \tag{3}$$

$I(hkl)$ is the intensity of the (hkl) peak, given by the area under the respective (hkl) peak. The crystallite size (D_{111}) was determined by X-ray line broadening and the surface area of powders by single point BET method from which equivalent spherical diameter (esd $- D_{BET}$) was calculated. The morphology of powders was observed in a scanning electron microscope (JEOL, JSM 840A, Japan). It was noticed that the particles were agglomerated. The particle size was determined by Coulter Counter (Quantachrome, USA). The median particle size (D_{50}) corresponding to 50 wt% on the cumulative plot was used to calculate agglomeration parameter (D_{50}/D_{BET}). The nature of agglomeration of particles was studied by compaction of powders filled in a die (3 mmϕ) under pressure up to ≃ 500 MPa, using a universal testing machine (Instron 1195). To study the possibility of breaking agglomerates to smaller aggregates by a hydrothermal treatment (HTT), the powder with calculated amount of water (to generate ≃ 2 MPa steam pressure) was sealed in a quartz tube (8 mm outer diameter, wall thickness 1·5 mm) and held at 220°C for times up to 40 h. The resulting powder was again characterized with respect to crystallite size, surface area and particle size. To obtain an indication of the $t \rightarrow m$ transformability, the powder was ground vigorously in a mortar and pestle for 45 min. High temperature stability was determined by heating the powder at 1200°C and 1400°C. The relative amounts of m and t phases were determined in each case.

3. Results and discussion

3.1 *Phases*

Figure 1 shows X-ray diffractogram from one of the powders. The predominant phase is tetragonal, though some monoclinic is also present. Sometimes it is hard to distinguish between the cubic and the tetragonal phases. However, in the present case the splitting of the (200)–(002) and (131)–(113) peaks, characteristic of the t phase and absence of the 100% cubic peak at $2\theta = 30{\cdot}48°$ shows that it is the t phase and not the cubic phase which is forming.

A t' phase is also found to be present in the powders prepared at 450°C and 500°C (figure 2) but not in the powders prepared at 550°C. In ZrO_2 stabilized by alloying oxides such as Y_2O_3 etc, the t' phase is considered to be a variant of the t phase having a higher solute content which makes it less prone to stress induced $t \rightarrow m$ transformation. As shown later, the transformation of the powder on grinding or on heating is found to be difficult which is consistent with the presence of a t' phase.

The stability of the tetragonal phase depends on the grain size, grain shape, stabilizer content and the constraint provided by the matrix. In the absence of a matrix constraint (e.g. for free powder) and with no stabilizer, the critical size for the t phase to be stable is very low, ≃ 30 nm. The average crystallite size of ZrO_2 prepared

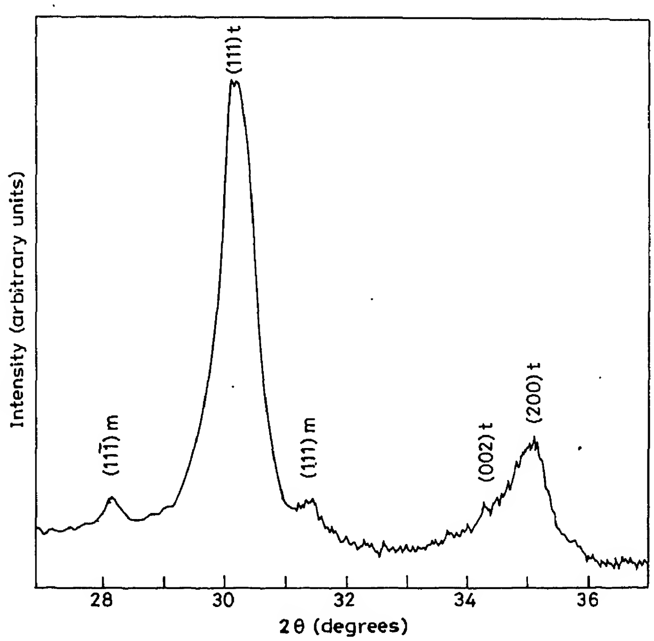

Figure 1. X-ray diffraction plot from ZrO_2 powder prepared at 500°C/75 h.

the present experiment is well within this size as wn later. Hence stability of the t-ZrO_2 appears to be narily due to the small crystallite size as also proposed Harrison *et al* (1987).

ıs Na is present during the solid state reaction, it is sible that the t phase may also be getting additionally bilized due to oxygen vacancies and lattice strains ated by dissolution of Na_2O in ZrO_2. Benedetti *et al* 89) have shown that 3 wt% Na stabilizes the cubic se in ZrO_2. Nishizawa and coworkers (Nishizawa *et* 1982, 1984) have also obtained similar results. In the vders prepared in the present work, the amount of in the ZrO_2 powders, as determined by atomic orption spectrophotometer, was found to be too small)·8 wt%) to stabilize the cubic phase. However, small ount of Na may contribute to the stability of the t se as reported by Sircar and Brett (1970) who found their study of phase equilibria in the system O – ZrO_2 – SiO_2, the formation of t-ZrO_2 and attributed o limited solution of Na_2O in ZrO_2. The role of Na_2O solved in ZrO_2 appears to be to increase the critical stallite size up to which the t phase is stable from 0 nm for unalloyed ZrO_2 to $\simeq$ up to 50 nm as shown r in the SEM results (§ 3.3).

Yield and reaction kinetics

yield (α) of the process defined as the quantity of $)_2$ obtained after the reaction as a fraction of the ount of ZrO_2 in the precursor (excluding unreacted noclinic ZrO_2) is shown in figure 3. The yield increases h the reaction temperature. However the fraction of t') ZrO_2 in the total powder is maximum at an rmediate temperature as shown in figure 4. The imum temperature appears to be 500°C where the d is 67% out of which 84% is $(t+t')$ phase.

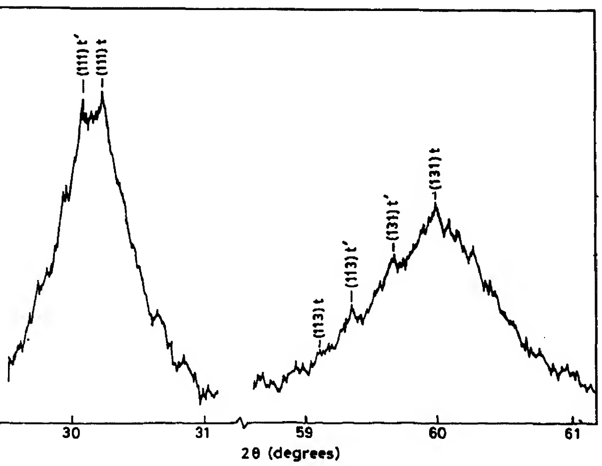

ıre 2. X-ray diffraction plots from sample prepared at °C/75 h showing the presence of t' phase.

The yield data was analyzed using the general method for the treatment of isothermal solid state reaction as proposed by Hancock and Sharp (1972). The data fitted the following equation

$$1-(1-\alpha)^{1/3}=kt \quad \text{(phase boundary controlled-sphere)}, \tag{4}$$

with a high correlation coefficient (> 0·999 for 550°C) signifying that the reaction is most probably phase boundary controlled.

3.3 *Powder morphology*

The average crystallite size determined by X-ray line

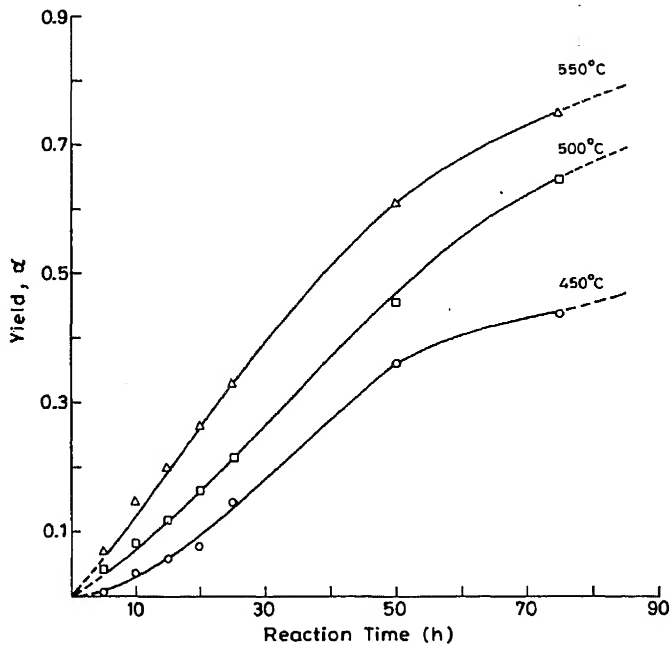

Figure 3. Yield (α) of ZrO_2 with reaction time at different temperatures.

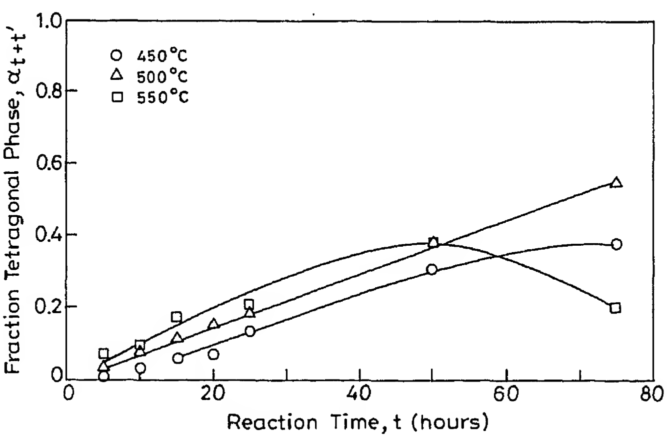

Figure 4. Yield of $(t+t')$ under different reaction conditions.

Table 1. Characteristics of the ZrO_2 powder obtained in the present experiments: properties of three powders from references is also given.

Powder characteristics	This work Reaction time (75 h) 450°C	500°C	550°C	Roosen and Hausner Coprecipitated dried at 120°C	Coprecipitated freeze dried	Haberko and Pyda Coprecipitated gels
Phase composition	87% *t* + *m*	84% *t* + *m*	25% *t* + *m*	Cubic	Cubic	Cubic
Specific surface area (m^2/g)	77	53	27	68	68	101·6
BET particle size (D_{BET} (nm))	12·9	18·9	37	16	16	10·5
Crystallite size (D_{111} (nm))	9	13·1	25·4	12·2	12·2	10·5
Agglomerated particle median size (D_{50} (μm))	2·1	2·05	4·3	1·9	0·7	–
Agglomerate parameter (D_{50}/D_{BET})	162	108	116	127	44	–

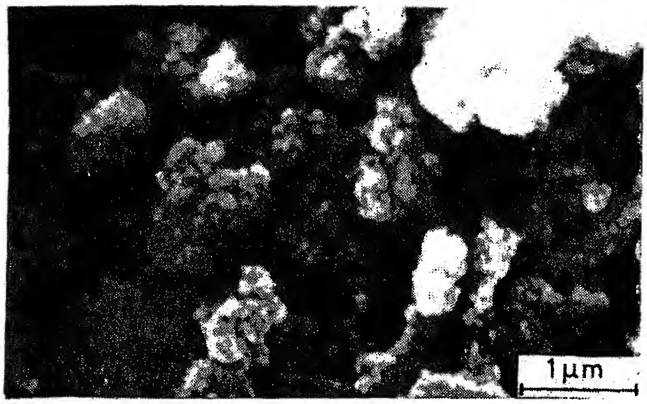

Figure 5. SEM photograph of powders of ZrO_2 (500°C/75 h) showing agglomeration of particles.

broadening as well as by BET surface area and the particle size determined by a Coulter Counter are given in table 1. Data on some other powders reported in literature is also included. An SEM picture is shown in figure 5. It is seen that the powders consist of 10–50 nm sized crystallites agglomerated into particles of a few microns. The discrepancy in the X-ray and BET data is due to the assumption of a spherical crystallite in the latter and also due to the presence of contacts between the crystallites. The rate of increase in crystallite size during the reaction is nearly zero at 450°C (after the initial crystallites are formed, figure 6). At 550°C, the crystallite size increases with time at a nearly constant rate up to 50 h and then levels off. At 550°C, the behaviour is similar as that for 500°C up to 50 h but then there is a rapid increase in the average crystallite size. This appears to be due to the exaggerated grain growth which is found to occur during sintering of ceramics and is characterized by the growth of a few large grains to very large sizes at the expense of the smaller grains.

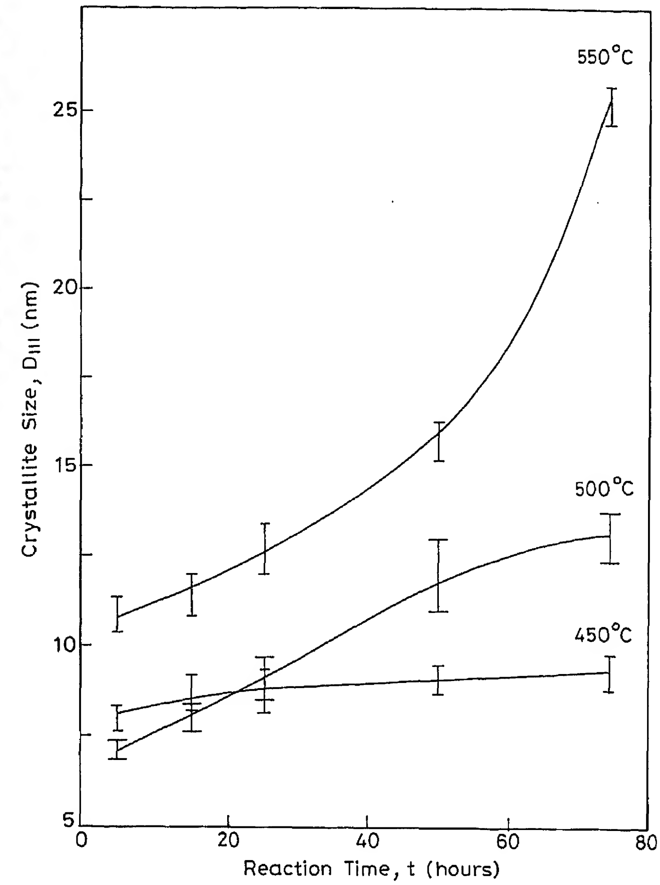

Figure 6. Crystallite size (D_{111}) of powders prepared at different times and temperatures.

3.4 *Agglomerate strength by compaction test*

When an agglomerated powder is subjected to a uniaxial pressure, the agglomerates break at a pressure indicated by a break in the plot of pressure vs packing density of the powder. Such a plot for 500°C/75 h powder is shown in figure 7. For comparison, data from literature (Graff *et al* 1980; Graff and Burggraff 1983; Haberko and Pyda 1983) for powders prepared by other methods is also included. It is seen that the powder prepared in

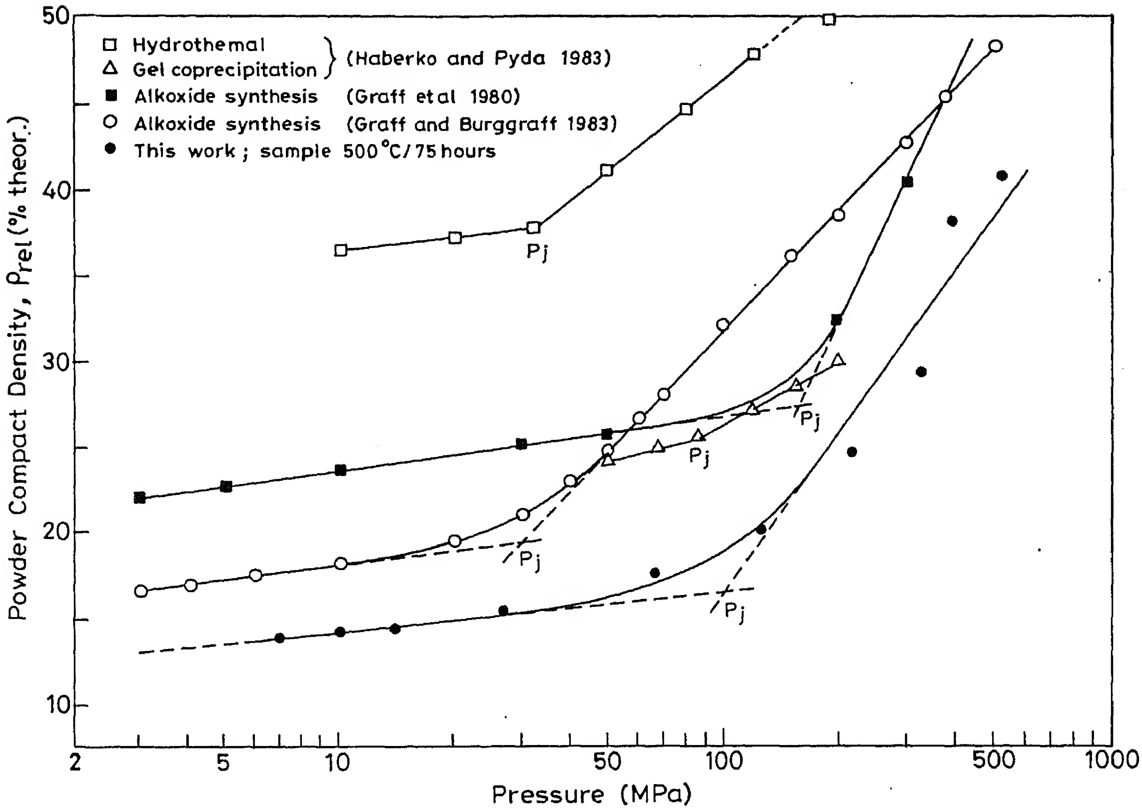

re 7. Powder compact density ρ_{rel} vs compaction pressure, P, of the powder prepared at 500°C/75 h, compared to data ted in literature for powders by alkoxide synthesis, hydrothermal synthesis and coprecipitation/calcination methods.

e 2. Effect of hydrothermal treatment on particle charac-ics (500°C/75 h)

	Surface area (m^2g^{-1})	D_{111} (nm)	D_{BET} (nm)	D_{50} coulter (μm)	$\frac{D_{50}}{D_{BET}}$
re HTT	53·2	13·1	18·9	2·1	108
HTT)h)	57·0	12·9	19·6	1·6	83

work has a high agglomerate breaking strength MPa) and a low packing density (Powder compact ity $\rho_{rel} = 13\%$) at low pressure ($\simeq 3$ MPa). The latter lt is due to the poor flow characteristics of the der and may also be due to a low agglomerate density. low agglomerate density implies that the crystallites tain their individuality in the agglomerates to a large nt. This is supported by the earlier results that they predominantly tetragonal and have high specific surface Thus these powders have strong solid bridges between allites and appear to be quite porous.

Effect of hydrothermal treatment

rothermal treatment has been found to be quite effective in breaking agglomerates in a TiO_2 powder by Heistand *et al* (1985). To study this effect the ZrO_2 powders obtained by reaction at 500°C/75 h were subjected to a hydrothermal treatment for 40 h in a quartz tube using 2 MPa steam at 220°C. The results are given in figure 8 and table 2. The hydrothermal treatment shifts the particle size distribution to lower sizes, with agglomerates larger than 6 μm totally eliminated. The average particle size comes down to 1·6 μm from 2 μm. There is no change in the crystallite size. However, the agglomerate parameter (agglomerate size/crystallite size) is reduced from 108 to 83 indicating that significant number of bonds between crystallites are broken under the conditions of hydrothermal treatment used. Further reduction in agglomerates may be produced by using higher pressures and temperatures during the hydrothermal treatment.

3.6 *Transformability under stress and on heating*

The powder (500°C/75 h) was crushed in mortar and pestle for 30 min. Only 12% of the t-ZrO_2 transformed to monoclinic indicating the presence of considerable amount of the t' phase. The powder was heated to different temperatures, held for 1 h and cooled to room temperature to determine the extent of $t \rightarrow m$ transfor-

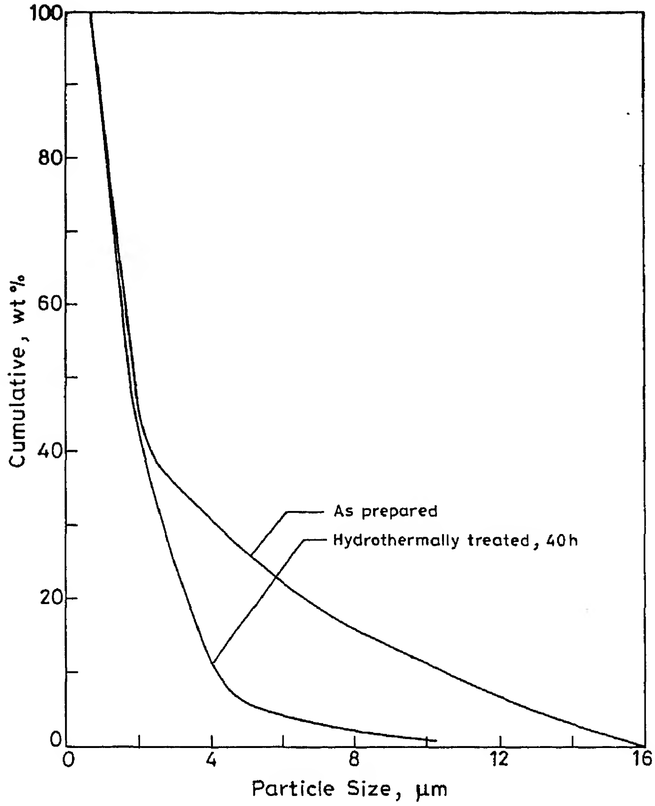

Figure 8. Particle size distribution of powder prepared at 500°C/75 h.

mation. Heating to 1200°C resulted in only slight increase in the monoclinic content while heating to 1400°C converted all the $(t+t')$ to monoclinic phase. Pellets sintered at 1550°C were also fully monoclinic. The t' phase is stable up to 1400°C. Above experiments thus show that most of powder prepared at 500°C exists as t'.

4. Summary

The solid state reaction used in the present work is successful in producing tetragonal zirconia. The kinetics of the reaction appears to be phase boundary controlled. The yield of tetragonal ZrO_2 is found to be maximum at 500°C where 84% of the powder is in the t phase. The zirconia crystallites, 9–25 nm in size, are agglomerated into particles of 2–4 μm. A substantial fraction of the powder is found to be in a nontransformable t' form. The factors which lead to this need to be understood in order to make these powders useful for toughening applications. The agglomerates have a breaking strength of 100 MPa which is well within the pressures used during dry pressing of ceramics. In order to exploit the property of the stress induced $t \rightarrow m$ transformation in t zirconia, it may be necessary to incorporate some stabilizer (e.g. Y_2O_3, CeO_2) in the powder and also to reduce the agglomerate size. A hydrothermal treatment is found to be useful in reducing the particle size substantially.

Acknowledgement

This work was partially supported by a grant from the Board of Research in Nuclear Sciences, Department of Atomic Energy, Government of India.

References

Benedetti A, Fagherazzi G and Pinna F 1989 *J. Am. Ceram. Soc.* **72** 467

Brook R J 1980 in *Advances in ceramics* (eds) A H Heuer and L W Hobbs (Columbus, Ohio: The American Ceramic Society) Vol. 3, p. 272

Graff M A C G Van de, Keizer K and Burggraaf A J 1980 in *Science of ceramics* (ed.) H Hausner (Berlin: Deutche Keramiche Gesellschabt) Vol. 10, p. 983

Graff M A C G Van de and Burggraaf A J 1983 in *Advances in ceramics* (eds) N Claussen, M Ruhle and A H Heuer (Columbus, Ohio: The American Ceramic Society) Vol. 12, p. 744

Haberko K, Ciesla A and Pron A 1975 *Ceram. Int.* **1** 111

Haberko K and Pyda W 1983 in *Advances in ceramics* (eds) N Claussen, M Ruhle and A H Heuer (Columbus, Ohio: The American Ceramic Society) Vol. 12, p. 774

Hancock J D and Sharp J H 1972 *J. Am. Ceram. Soc.* **55** 74

Harrison A, Stevens R and Miline S J 1987 *J. Mater. Sci. Lett.* **6** 673

Heistand II R H, Ogure Y, Okamura H, Moffalt W C, Novich R, Barringer E A and Bowen H K 1985 in *Science of ceramic processing* (eds) C L Hench and R Ulrich Donald (New York: John Wiley and Sons) pp. 482–497

Jean V S 1991 *Br. Ceram. Proc.* **47** 45

Kagawa M, Honda F, Onodera H and Nagawe 1983 *Mater. Res. Bull.* **18** 1081

Maher G H, Hutchins C E and Ross S D 1993 *Am. Ceram. Soc. Bull.* **72** 72

Mazdiyasni K S, Lynch C T and Smith J S III 1967 *J. Am. Ceram. Soc.* **50** 532

Mottet B, Pichvant M, Beny J M and Alary J A 1992 *J. Am. Ceram. Soc.* **75** 2515

Nishizawa H, Yamasaki N, Matsuoka K and Mitsushio H 1982 *J. Am. Ceram. Soc.* **65** 343

Nishizawa H, Tani T and Matsuoka K 1984 *J. Mater. Sci.* **19** 2921

Rhodes W H 1981 *J. Am. Ceram. Soc.* **64** 19

Roosen A and Hauser H, 1983 in *Advances in ceramics* (eds) N Claussen, M Ruhle and A H Heuer (Columbus, Ohio: The American Ceramic Society) Vol. 12, p. 714

Sirkar A and Brett N H 1970 *Trans. Br. Ceram. Soc.* **69** 131

Suzuki M, Kagawa M, Syono Y and Hirai T 1992 *J. Mater. Sci.* **27** 679

Toraya H, Yoshimara M and Somiya S 1984 *J. Am. Ceram. Soc.* **67** C-119

Mater. Sci., Vol. 21, No. 1, February 1998, pp. 87–92. © Printed in India.

ptical and structural characteristics of strontium doped calcium rtrate crystals

K SURYANARAYANA*, S M DHARMAPRAKASH and K SOORYANARAYANA[†]

Department of Physics, Mangalore University, Mangalagangotri 574 199, India
[†]Solid State and Structural Chemistry Unit, Indian Institute of Science, Bangalore 560 012, India

MS received 17 April 1997

Abstract. We report here on the optical and structural characteristics carried out on strontium doped calcium tartrate tetrahedral single crystalline materials obtained by diffusing calcium and strontium ions through silica gel impregnated with optically active tartaric acid. Linear optical properties of this material such as refractive index, birefringence and transmission characteristics were measured in the wavelength range 200 nm $<\lambda<$ 1500 nm. No dispersion of the birefringence was observed within the experimental accuracy. The packing of tartrate molecules remained unaltered with 12% of the strontium doping.

Keywords. Silica gel; refractive index; crystal structure; second harmonic generation.

Introduction

le crystals of calcium tartrate (CT) and strontium ate (ST) have attracted considerable attention in nt years on account of their ferroelectric, non linear al and spectral characteristics (Medrano *et al* 1987; at and Wyncke 1989; Nakatani 1991; Selvarajan 1993; Rethinam *et al* 1994). CT and ST crystallize ne orthorhombic system with space group $P2_12_12_1$ ng four molecules in the elementary unit cell (Ambady ; Bohandy and Murphy 1968). In the course of our stigations on the physical properties of CT and ST ttention was drawn to the growth and characterization trontium doped calcium tartrate (CST). This work undertaken to study the optical characteristics and t of doping on the structural role of tartrate ion in presence of two divalent metallic elements.

Experimental

Growth and crystal habit

strontium doped calcium tartrate single crystals oyed for optical and X-ray diffraction studies were n by the silica gel method. The growth process ves the controlled diffusion of calcium chloride– tium chloride solutions into gel made up of sodium silicate and tartaric acid (all AR grade) solutions at tant temperature and visible light conditions. The riment was performed in Corning glass tubes of h 200 mm and inner dia. 25 mm. The suitable con- ns for the growth of the best quality CST single crystals were: pH 3·5–4·0, gelling time 12 days, concentration of the reactants 1·0 M and growth temperature 30°C. Growth of CST crystals (about $10\times6\times4$ mm^3 in size) was observed down the gel column in the experimental vessels within a week. During the exchange reaction HCl yielded as a byproduct. The crystal size and time of formation of ST depend on the density of the gel and concentration of the supernatent solutions. The gel grown CST single crystals were colourless and optically transparent. Qualitative chemical analyses using an energy dispersive X-ray spectrometer (EDX) confirmed that the single crystals are those of CST in which two alkaline earths form solid solution in the ratio 0·88 : 0·12. The maximum uptake of strontium in the CST crystal depends on the molarity of the mixed calcium chloride and strontium chloride solutions with different ratios. The crystals grown were confirmed to have the composition $Ca_{0.88}Sr_{0.12}C_4H_4O_6\cdot4H_2O$ under the above mentioned growth conditions. The single crystalline habit of CST is deviated from the habit of CT and ST single crystals (figure 1). The crystals are elongated in the b-direction and the principal faces are (110), (010) and (011) with their symmetry equivalents.

2.2 *Structure*

The crystal thus grown was transparent and was mounted on the X-ray diffractometer after confirming the quality by examining under a polarizing microscope. The intensity data were collected on an Enraf–Nonius CAD4 diffractometer having graphite monochromated MoKα radiation ($\lambda=0.7107$ Å) in the $\omega/2\theta$ mode. The cell parameters were obtained from the least square refinement of 25 reflections ($-2\,3\,1$, $-1\,3\,0$, $0\,3-1$) after every 3600 s

hor for correspondence

of exposure time; the orientation was checked every 400 reflections and no significant fluctuations in their intensity were observed. The data was corrected for Lorenz and polarization effects but not for absorption effect since it is negligible. The structure of strontium doped calcium tartrate tetrahydrate was solved using SHELXS 86 (Sheldrick 1985). The heavy atoms were located using Patterson method and the rest of the structure was developed using partial structure expansion technique. The structure refinement was carried out using SHELX 93 (Sheldrick 1993). Hydrogen atoms were located from the difference map. All nonhydrogen atoms were refined anisotropically. The details of crystal data and refinement results are given in table 2.

3. Results and discussion

3.1 *UV-visible spectrum of CST single crystals*

Optical absorption measurements for CST single crystal with thickness 1·0 mm were performed with a Cary-14 spectrophotometer in the range 200–1400 nm at room temperature. No absorption decreasing film was coated on the surfaces of the crystal and the light loss caused by reflections on the surfaces was ignored. The absorption coefficient as a function of wavelength, was evaluated. Anisotropy was observed for different light directions. One can see from figure 2 that the single crystals of CST are transparent in the range 275–1325 nm and the transmittivity is greater than 85%. The optical transmission range as determined from the optical characteristics, makes the CST crystal interesting for second harmonic generation in the ultra violet region.

3.2 *Linear optical properties*

According to the crystal system three planes normal to the three orthorhombic unit cell axes with x, y, z parallel

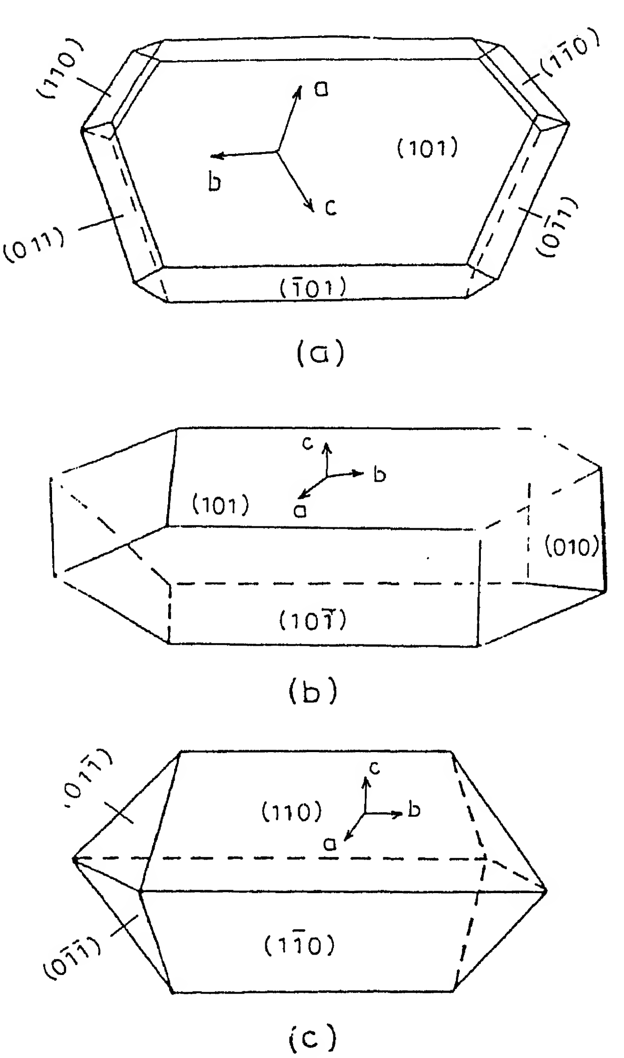

Figure 1. Habit of (a) calcium tartrate, (b) strontium tartrate and (c) strontium doped calcium tartrate single crystals.

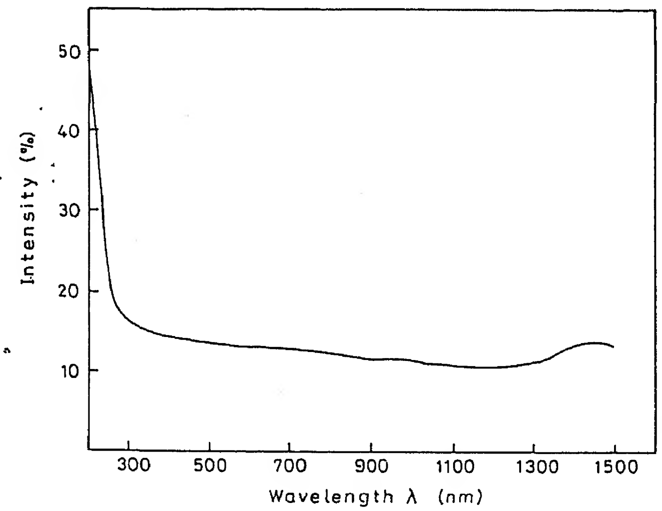

Figure 2. UV visible spectra of strontium doped calcium tartrate single crystal (thickness, 1·0 mm).

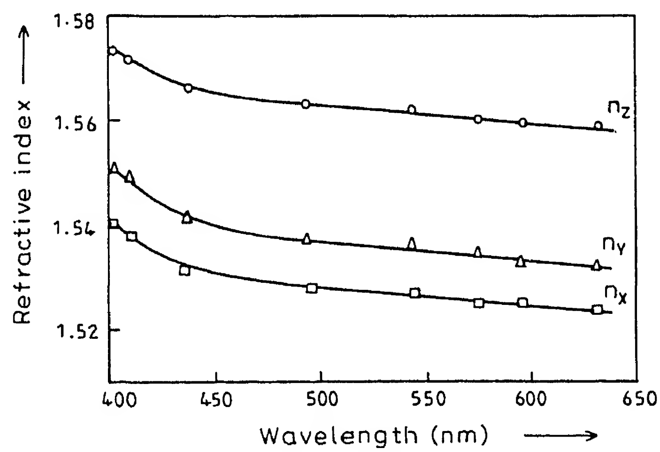

Figure 3. Dispersion of the principal refractive indices of strontium doped calcium tartrate single crystal at room temperature.

the crystallographic a, b and c axes, respectively, were epared to determine birefringence and refractive indices. e refractive index of the crystal within the visible ht range was measured by the Brewster's angle method

ble 1. Linear optical data of CST single crystals.

	Refractive indices			Birefringence	
nm)	n_x	n_y	n_z	Δn_x	Δn_z
5	1·5398	1·5514	1·5738	0·02	0·03
3	1·5383	1·5501	1·5726	0·02	0·03
5	1·5316	1·5431	1·5661	0·02	0·03
2	1·5292	1·5392	1·5639	0·02	0·03
5	1·5272	1·5378	1·5632	0·02	0·03
7	1·5255	1·5356	1·5611	0·02	0·03
0	1·5243	1·5344	1·5589	0·02	0·03
5	1·5229	1·5336	1·5567	0·02	0·03

ɔle 2. Crystal data and structural refinement.

pirical formula	$Ca_{0.876}Sr_{0.124}C_4H_{12}O_{10}$
mula weight	266·11
stal size (in mm)	0·41 × 0·12 × 0·18
stal system	Orthorhombic
ce group	$P2_12_12_1$
t cell dimensions	
	9·231(2) Å
	9·619(4) Å
	10·610(5) Å
ume	942·2(6) Å^3
number of molecules er unit cell)	4
000)	576·0
sity (calc)	1·875 g/cm^3
iation used	Mo Kα (λ = 0·7107 Å)
ractometer	Enraf–Nonius CAD4
raction measurement ethod	$\omega/2\theta$
lections collected	2284
que reflections	2027
range	2·86° to 26·97°
, l range	$-11 \leq h \leq 11$ $0 \leq k \leq 12$ $0 \leq l \leq 13$
inement method	Full matrix least squares on F^2
odness of fit on F^2	1·587
l R indices $> 2\sigma(I)$)	R = 0·087, wR = 0·233
ndices (all data)	R = 0·152, wR = 0·268
idual electron ensity	max = 0·83 e/Å^3, min = −0·58 e/Å^3

(figure 3). The data are listed in table 1. The quality of the crystal together with the low birefringence of this material led to a precise measurement with an accuracy of ±0·005. The wavelength dependence of the birefringence was determined by using a monochromator, mercury lamp, sodium lamp and He–Ne laser as light source for the polarizing microscope. The birefringence is independent of the wavelength in the wavelength range 400–650 nm.

CST belongs to one of the four acentric orthorhombic point groups, determined by the convention that the principal refractive indices are such that $n_z > n_y > n_x$, which implies that in CST crystal the optical plane is the x–z plane. Results on the dispersion of the indices of refraction show that CST is an optically positive biaxial crystal.

3.3 *Non linear optical properties*

The second harmonic generation experiments were performed with an unfocussed and linearly polarized, Nd : YAG laser (λ = 1·064 µm). CST crystal exhibits small optical nonlinearity. The second harmonic generation intensity of CST is 0·1 times that of quartz. Limited by the experimental condition, the nonlinear optical coefficients of CST single crystal have not been obtained.

3.4 *Structure*

There is no significant structural change in the CST

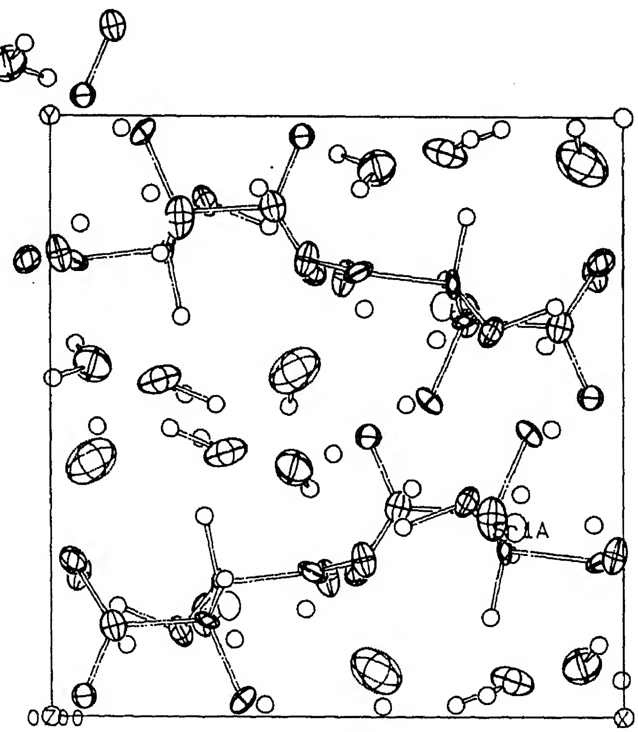

Figure 4. The structure of strontium doped calcium tartrate single crystal.

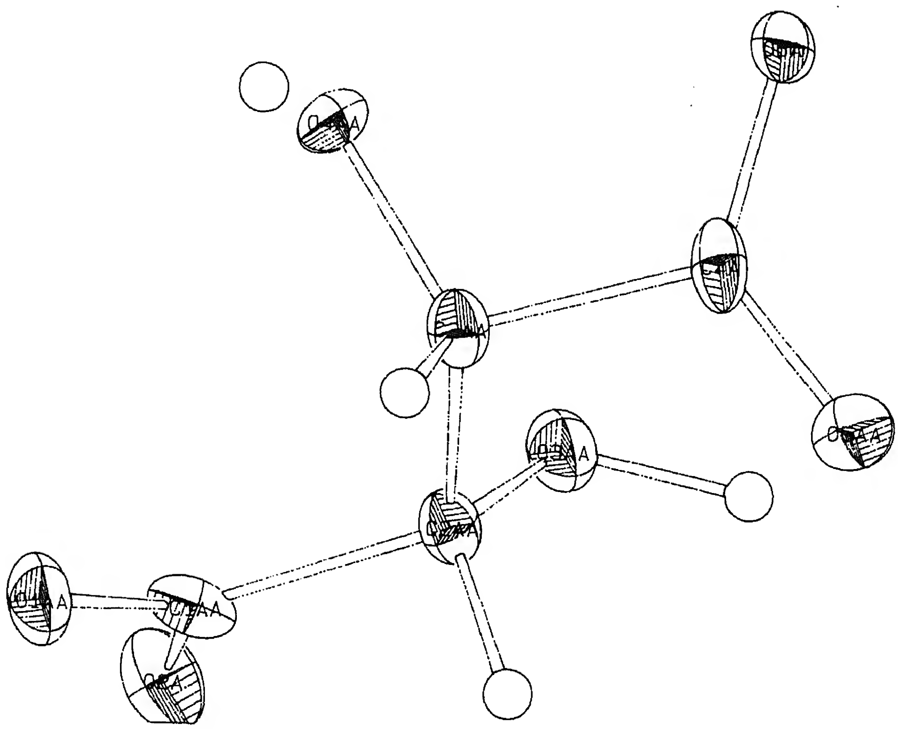

Figure 5. The details of the tartrate molecule.

Table 3. Atomic coordinates, occupancy and U_{eq}.

	x/a	y/b	z/c	Occupancy	U_{eq}
Sr	0·1864(2)	0·8160(2)	0·8218(2)	0·124	171(4)
Ca	0·1864(2)	0·8160(2)	0·8218(2)	0·876	171(4)
O1	0·4507(8)	0·7617(8)	0·8086(8)	1·000	209(1)
O2	0·0153(8)	0·7688(9)	0·9920(9)	1·000	273(6)
O3	0·7717(8)	0·6415(8)	0·9517(8)	1·000	198(6)
O4	0·6627(8)	0·5273(8)	0·7168(8)	1·000	219(0)
O5	−0·0389(8)	0·7583(9)	0·7143(8)	1·000	222(8)
O6	0·0573(8)	1·0334(7)	0·8275(9)	1·000	221(4)
O7	0·1928(12)	0·5604(9)	0·8296(13)	1·000	552(6)
O8	−0·0732(11)	1·0854(10)	1·0702(10)	1·000	404(0)
O9	0·2269(9)	0·8309(11)	0·5877(8)	1·000	329(8)
O10	0·4285(14)	0·5763(12)	0·5668(12)	1·000	624(6)
C1	0·5407(12)	0·7405(11)	0·8927(11)	1·000	200(0)
C2	0·7049(11)	0·7216(11)	0·8612(10)	1·000	172(4)
C3	0·7245(11)	0·6604(10)	0·7293(10)	1·000	119(9)
C4	0·1095(11)	1·1503(11)	0·7979(11)	1·000	177(8)
H1	0·88270	0·68360	0·95580	1·000	
H2	0·72970	0·83370	0·85550	1·000	
H3	0·69380	0·72880	0·65570	1·000	
H4	0·62410	0·52030	0·67590	1·000	
H5	0·29020	0·52030	0·86380	1·000	
H6	0·23640	0·53680	0·76380	1·000	
H7	−0·04380	1.12040	1·16000	1·000	
H8	−0·00440	1·06240	0·98000	1·000	
H9	0·17630	0·87130	0·60350	1·000	
H10	0·36640	0·88110	0·60310	1·000	
H11	0·41840	0·51760	0·48280	1·000	
H12	0·55200	0·67930	0·53880	1·000	

U_{eq} is defined as one-third of the trace of the orthogonalized U_{ij} tensor.

Table 4. Anisotropic thermal parameters ($Å^2 \times 10^4$).

Atom	U_{11}	U_{22}	U_{33}	U_{23}	U_{13}	U_{12}
Ca	126(8)	209(9)	178(9)	0(9)	3(9)	−7(9)
Sr	126(8)	209(9)	178(9)	0(9)	3(9)	−7(9)
O1	149(35)	313(40)	166(42)	−29(36)	−2(35)	46(35)
O2	165(38)	359(53)	297(50)	21(38)	−24(36)	−60(35)
O3	160(37)	228(43)	207(42)	−62(32)	−43(32)	70(29)
O4	163(42)	167(39)	328(48)	−78(32)	−76(34)	−84(31)
O5	178(39)	197(39)	294(51)	−93(35)	−11(35)	98(50)
O6	154(36)	148(35)	362(53)	6(38)	109(40)	−1(30)
O7	529(66)	198(46)	932(92)	−55(57)	−112(79)	98(50)
O8	373(53)	334(52)	506(69)	−162(45)	40(49)	46(42)
O9	244(44)	491(57)	254(46)	−165(46)	27(35)	3(45)
O10	680(78)	557(73)	637(88)	−153(59)	−311(68)	212(61)
C1	218(57)	108(49)	274(69)	51(46)	56(52)	76(48)
C2	59(49)	218(58)	240(56)	65(40)	72(42)	−15(39)
C3	154(50)	63(50)	142(50)	61(37)	−8(38)	58(37)
C4	156(52)	257(66)	120(57)	−99(42)	−17(44)	−27(43)

The anisotropic displacement factor exponent takes the form $-2\pi^2[(ha^*)^2U_{11}+\ldots+2hka^*b^*U_{12}]$.

Table 5. Interatomic distances (Å) in strontium doped calcium tartrate tetra hydrate.

Ca(Sr)–O6	2·407(7)
Ca(Sr)–O5	2·436(8)
Ca(Sr)–O2	2·441(9)
Ca(Sr)–O7	2·461(8)
Ca(Sr)–O4	2·498(8)
Ca(Sr)–O1	2·499(7)
Ca(Sr)–O9	2·516(9)
Ca(Sr)–O3	2·561(8)
O1–C1	1·236(14)
O2–C1	1·249(14)
O3–C2	1·377(13)
O3–Ca(Sr)	2·561(8)
O3–H1	1·103(8)
O4–C3	1·408(12)
O4–Ca(Sr)	2·498(8)
O4–H4	0·565(8)
O5–C4	1·233(13)
O6–C4	1·263(13)
O7–H5	1·044(11)
O7–H6	0·837(13)
O8–H7	1·046(10)
O8–H8	1·170(10)
O9–H9	0·630(9)
O9–H10	1·385(8)
O10–H11	1·059(11)
C1–O2	1·249(12)
C1–C2	1·563(15)
C2–C3	1·530(15)
C2–H2	1·104(10)
C3–C4	1·562(14)
C3–H3	1·060(10)
C4–O5	1·233(13)
C4–C3	1·562(14)

Table 6. Selected bond angles (degrees).

C2–O3–H1	103·8(7)
C3–O4–H4	115·8(10)
H5–O7–H6	77·0(9)
H7–O8–H8	131·7(10)
H9–O9–H10	116·2(11)
H11–O10–H12	104·2(9)
O1–C1–C2	121·1(10)
O3–C2–C1	110·5(9)
C1–C2–H2	95·7(9)
C1–C2–C3	110·8(8)
O3–C2–H2	119·5(9)
O3–C2–C3	111·7(8)
C3–C2–H2	107·5(9)
O4–C3–C2	112·9(8)
C2–C3–H3	113·8(9)
O4–C3–H3	112·8(9)
O7–H5–H6	43·6(7)
O7–H6–H5	59·4(8)

en compared with calcium tartrate (Hawthorne *et al* 32). The crystal structure is shown in figure 4. Atomic ordinates and anisotropic thermal displacement para-ters are given in tables 3 and 4, respectively. Inter-atomic distances, selected bond angles and hydrogen bond lengths are given in tables 5–7. The metal ion is coordinated by eight oxygens forming a distorted Siamese dedicahydron (Johnson 1966). The water molecule connects tartrate motifs by hydrogen bonding hence forming an infinite chain which runs along the a-axis. The adjacent chains are linked along b-axis by the metal and tartrate oxygen bonds. We conclude from this study that the packing of tartrate molecules remains unaltered with 12% of the strontium doping. Details of the tartrate molecule are shown in figure 5.

4. Conclusion

The silica gel growth system involves the use of calcium chloride and strontium chloride as the top reactants and sodium meta silicate impregnated with tartaric acid as

Table 7. Hydrogen bonds.

A–H ... B	A–H	A ... B	H ... B	A–H ... B
O4–H4 ... O10	0·565(8)	2·725(15)	2·211(13)	152·5(8)
O7–H5 ... O1	1·044(11)	3·077(13)	2·816(8)	94·4(5)
O8–H8 ... O2	1·170(10)	3·261(13)	2·833(9)	100·8(5)
O8–H8 ... O6	1·170(10)	2·887(14)	1·738(9)	166·0(6)
O9–H9 ... O5	0·630(9)	2·882(11)	2·551(8)	115·8(9)
O9–H10 ... O1	1·385(8)	3·194(11)	2·584(8)	103·0(4)
O3–H1 ... O2	1·103(7)	2·596(11)	1·522(8)	162·8(5)
O3–H1 ... O5	1·103(7)	3·266(11)	2·758(8)	107·6(5)

lower reactant results in the crystallization of calcium strontium tartrate with the molecular formula $Ca_{0.88}Sr_{0.12}C_4H_4O_6 \cdot 4H_2O$. The optical transition range has been determined from the UV-visible spectra for CST which extends from 275 nm to 1400 nm. This makes the CST material interesting for second harmonic generation in the UV region. The optical characteristics of CST crystal is found to be positive. CST exhibits optical nonlinearity. From the structural study, it is found that the packing of tartrate molecules remains unaltered with 12% of strontium doping in CST.

Acknowledgement

We thank Prof. T N Guru Row, Solid State and Structural Chemistry Unit, Indian Institute of Science, Bangalore, for providing facilities to carry out the structural work of material.

References

Ambady G K 1968 *Acta Crystallogr.* **B24** 1548
Bohandy J and Murphy J C 1968 *Acta Crystallogr.* **B24** 286
Brehat F and Wyncke B 1989 *J. Phys. B: At. Mol. Opt. Phys.* **22** 1981
Hawthorne F C, Borys I and Ferguson R B 1982 *Acta Cryst.* **B38** 2461
Johnson N W 1966 *Canadian J. Math.* **18** 169
Medrano C, Gunter P and Arend H 1987 *Phys. Status Solidi* **(b)14B** 749
Nakatani N 1991 *Jap. J. Appl. Phys.* **30** 1961
Rethinam F J, Arivuoli D, Ramasamy S and Ramasamy P 1994 *Mater. Res. Bull.* **29** 309
Selvarajan P, Has, B N Gon and Rao K V 1993 *J. Mater. Sci. Letts* **12** 1210
Sheldrick G M 1985 *SHELXS 86, program for the solution of crystal structures* (Germany: Univ. of Gottingen)
Sheldrick G M 1993 *SHELXL 93, program for the refinement of crystal structures* (Germany: Univ. of Gottingen)

ll. Mater. Sci., Vol. 21, No. 1, February 1998, pp. 93–97. © Printed in India.

ffect of fillers on acousto ultrasonic response in GRP composites

PRAVESH KUMAR

MTC Division, National Metallurgical Laboratory, Jamshedpur 831 007, India

MS received 20 January 1996; revised 24 December 1996

Abstract. **In recent years, there has been a wide interest in fillers which improve the quality and performance of fibre composites when mixed in a small quantity in the matrix. In the present work the effect of addition of mica and graphite powders in cross ply glass fibre reinforced plastic (GRP) composites has been studied by using acousto ultrasonic (AU) technique. The mechanical strengths of these composites were correlated with fibre volume fraction (V_f). The stress wave factor (SWF) was evaluated and correlated with tensile/flexural strengths of these composite specimens. The observations show a linear relationship between the SWF values and strength of unfilled and filled GRP composites.**

Keywords. **Stress wave factor; filled and unfilled GRP; acousto ultrasonic; fibre volume fraction.**

Introduction

ss fibre reinforced plastic (GRP) composites have le acceptance by many industries because of their h strength to weight ratio, good corrosion resistance availability of design criteria. It has been seen that ers are used in many applications. The filled composites ibit moderately improved mechanical properties, nping, attenuation as well as thermal stability cha- eristic depending on the kind of filler employed.

Iany cases have been discussed and illustrated where highest concentration of filler and therefore maximum t reduction is highly advantageous. Conversely, the itations of filler use are also described. The filler ection is primarily determined by the particle size ribution. Average particle size is useful for evaluating cific properties of fillers. Quality control of these ers is usually exercised by controlling the coarseness average particle size control of coarseness is essential. wever, instead of particle size, particle packing is st significant.

errigno (1978) described and illustrated the advanta- us use of fillers in fibre-reinforced composite material. vastava *et al* (1988) used fly ash as a filler in glass e-reinforced plastic composites and determined the cture toughness and fracture surface energy. Ramsteiner Theysohn (1984) studied the tensile behaviour of ed composites. Lorne (1992) studied filled glass e-reinforced polyester composites in aqueous envi- ments and reported that GRP are used extensively in rication of underground piping and storage vessels water and sewage applications for reasons of economy. compromise between the cost and mechanical per- nance, mica and graphite powder have been used in study. Nondestructive testing of GRP composites is of great significance if the GRP composites are to be used with greater reliability. Therefore, the mechanical and nondestructive AU testing of fabricated GRP composites with and without fillers was extensively studied in the present paper.

2. Experimental

2.1 *Preparation of samples*

Cross ply composite laminates were fabricated in laboratory by hand lay-up technique. This is a conventional technique being used from the ages for its ease and low cost. In this technique E glass fibre (0/90°) was used as a reinforcing medium; resin (Cy205) and hardener (Hy951) were used as matrix. The resin and hardener were mixed in the ratio of 10 : 1 for about five min at room temperature. Thereafter, the mixture was kept at 60°C for about 30 min to avoid air bubbles, voids and to get proper mixing. The mixture of resin and hardener was poured in a mould which was coated with the releasing agent. In this mould a layer of woven glass fibre mat was laid. After evenly spreading the resin in mould another layer of woven glass fibre mat was laid and this process was repeated until the required thickness was obtained. Thereafter, a suitable dead weight was placed on the top plate of the mould for removal of excess resin and air bubbles. After curing, GRP plates were removed from the mould. Curing time at room temperature was observed to be about 24 h.

The filler chosen in the present study is graphite. It is a crystalline carbon formed by mineralogical process and is uniform and provides good acid and alkali resistance. GRP plates with muscovite mica and graphite powders as fillers were fabricated in laboratory in the same manner as described above.

The particle sizes were measured by sieving; mica powder, particle size 100μ and 5% by weight, was used and was mixed in matrix (resin : hardener :: 10 : 1). Similarly, graphite powder, particle size 100μ and 5% by weight, was mixed in matrix. The mechanical properties of these fillers are given in table 1. The composite plates were fabricated with least possible variation in fibre volume fraction (V_f) achieving a constant V_f of 50%. Also, composite sheets were fabricated with varying V_f. Variation in V_f was achieved by controlling the amount of fibre being used while making the composites. Fibre volume fraction of the sample was measured by acid digestation high temperature heating process as per BIS specification HIVID 4 (001S) P1.

The mica-powder-filled GRP composite plates and graphite-powder-filled GRP composite plates were used for comparative study of their mechanical properties vis-à-vis GRP composites.

2.2 *Evaluation of tensile and flexural strengths*

Thirty tensile specimens were made from the fabricated composite sheets in dog bone shape for tensile strength. The SWF values at different locations were obtained and tensile strength was evaluated using Hounsfield tensometer.

Flexural strength of unfilled and filled composites, was obtained under three-point bending test using an universal testing machine. In three-point bending, when a force is applied at the centre of the upper surface of an end supported beam as in ASTM D-790, the upper surface is under compression and the lower surface is in tension. Maximum stress is applied only to the surface in tension. The decreasing strain through the cross section (from lower to upper surface) had the effect of providing somewhat higher flexural than tensile yield strength. This is especially pronounced for matrices having elongation greater than about 5%. Inherently tough polymers may obtain higher flexural strength with high aspect ratio fillers or solid fillers treated with coupling agents. The flexural strength (σ_m) is evaluated using the following expression:

$$\sigma_m = 3PL/2bh^2,$$

where, P is the maximum load in Kgf, b the specimen width, h the thickness of the specimen and L the distance between two spans.

Table 1. Properties of mica and graphite particles used in study.

Materials	Size	Tensile modulus (GN/m^2)	Density (g/cc)	Compressive strength (MN/m^2)	Response
Mica powder	100μ	172	2·13	72·15	Very soft/mild
Graphite powder	100μ	1250	3·20	80·60	Tough/brittle

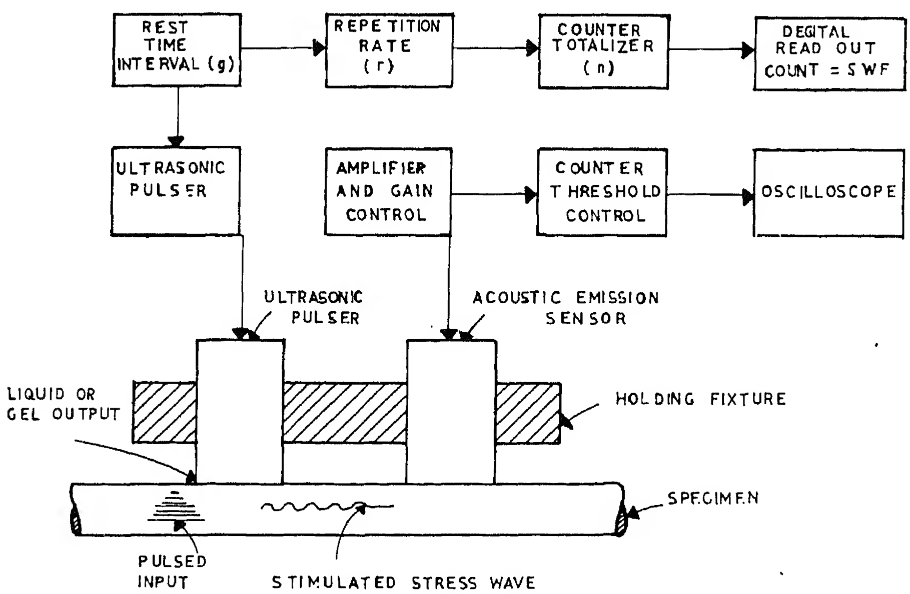

Figure 1. Block diagram for measurement of stress wave factor.

Acousto ultrasonic testing

e fabricated composites were characterized by AU hnique according to ASTM standard E 1495. This is atively a new non-destructive testing technique and is entially an amalgamation of the two techniques: acous- emission and ultrasonic technique, in which ultrasonic ses are induced in the material by a pulser. The uced pulses interact with voids and cracks present de the material and the pulse thus gets modulated. e modulated signals are picked up by another piezo- ctric acoustic emission sensor called receiver. These pulses pass through a preamplifier and to an amplifier and finally to the analysing circuit. For characterization of material quality, one has to calculate stress wave factor (SWF). It was defined by Vary (1980) as:

$$\mathrm{SWF} = grn,$$

where, g is the pulse rate (ultrasonic pulse), r the repetition rate (time) and n the number of pulses which cross a fixed threshold voltage.

In other words, multiplication of these parameters would give stress wave factor of a particular material. Therefore SWF was evaluated in the present investigation by using AET-206 AU instrument. The SWF values thus obtained at different locations on unfilled and filled GRP-composites when the noise interference was minimum. Transducers were firmly placed at a distance of 4 cm against the specimen to avoid changes in the pressure during the time when pulser was activated. The block diagram of the apparatus for measurement of SWF is shown in figure 1.

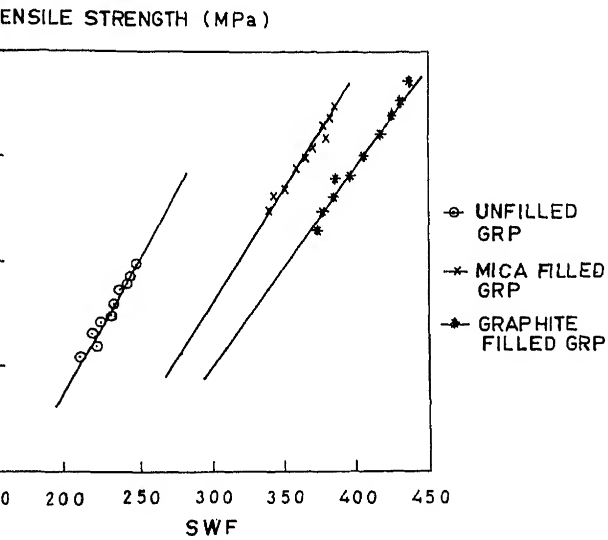

ıre 2. Variation of tensile strength with SWF of GRP posites.

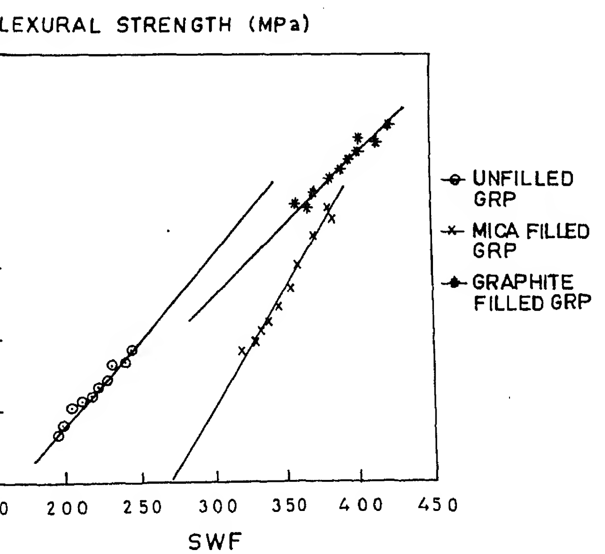

ıre 3. Variation of flexural strength with SWF of GRP posites.

3. Results and discussion

Figures 2 and 3 show the relationship between the SWF and tensile strength, and SWF and flexural strength of unfilled GRP, mica- and graphite-filled GRP composites. As far as unfilled and mica-filled composites are concerned, the SWF values were found to be lower whereas graphite filled composites showed significantly higher values. The correlation coefficient r and student t values were evaluated from the plots of SWF and tensile/flexural strengths and are listed in table 2. The results show that a good correlation exists between SWF values and the mechanical strengths in the unfilled as well as filled composites.

Figures 4–6 show and describe tensile and flexural strength with respect to fibre volume fraction. Fillers affect tensile properties according to their packing characteristics, size and interfacial bonding. The spaces between particles are assumed to be filled with matrix and no voids or air bubbles are present. Under these conditions, for a given system, the matrix volume is at a minimum and acts as individual segment or pocket to support tensile load.

Table 2. Correlation coefficient (r) values of GRP composites.

Materials	Tensile strength correlation coefficient (r)	Flexural strength correlation coefficient (r)
Unfilled GRP	0·945	0·895
Mica filled GRP	0·964	0·927
Graphite filled GRP	0·986	0·976

Flexural testing can be used for grading specimens in materials evaluation, process development and improvement and quality control. However, a true correlation between flexural properties and other mechanical properties has never been established. There are many subtle variables affecting bending test strength so that the problem of correlating flexural data with the more basic properties can outweigh all advantages of meaningful design data.

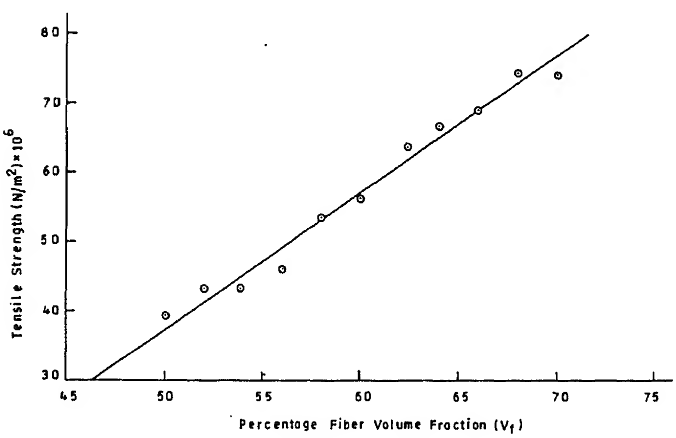

Figure 4. Variation of tensile strength with percentage V_f of unfilled GRP composite.

In the present investigation, it was observed that the quality of virgin GRP composite is improved by adding graphite powder, but this is not so when mica powder was added which has been frequently used in composite development programmes. The reason being that the carbon atoms of the graphite powder easily reacted with the epoxide of epoxy resin which in turn contributed for the improved cohesive strength. In the mica powder $K_2Al_4\,(Al_2Si_6O_{20})\,(OH)_4$ having chemical composition as: SiO_2–47·9%, Al_2O_3–33·13%, MgO–0·69%, Fe_2O_3–2·04%, K_2O–9·8%, Na_2O–0·8%, CaO–0·5%, TiO_2–0·65%, Cr_2O_3–0·65%. These do not easily dissolve in the epoxy resin and, therefore, will not help to increase strength of the composite. The higher SWF values obtained would generally provide a means of rating the efficiency of dynamic

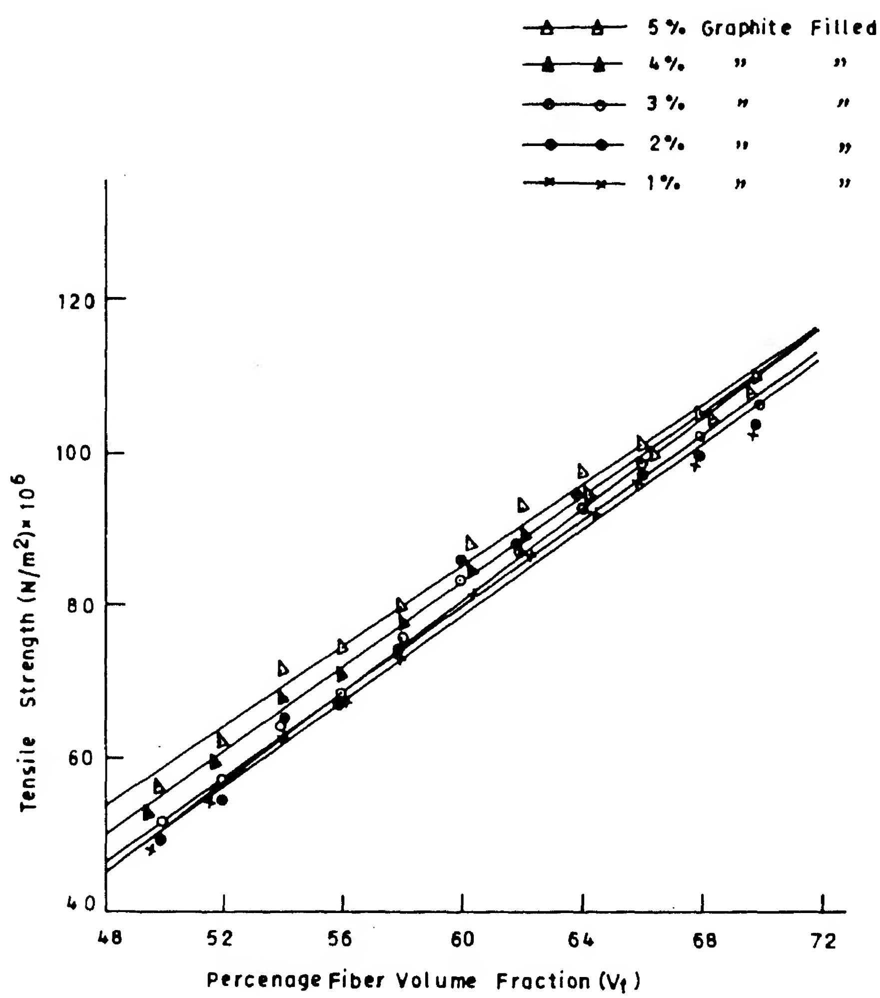

Figure 5. Variation of tensile strength with percentage V_f of graphite filled GRP composite.

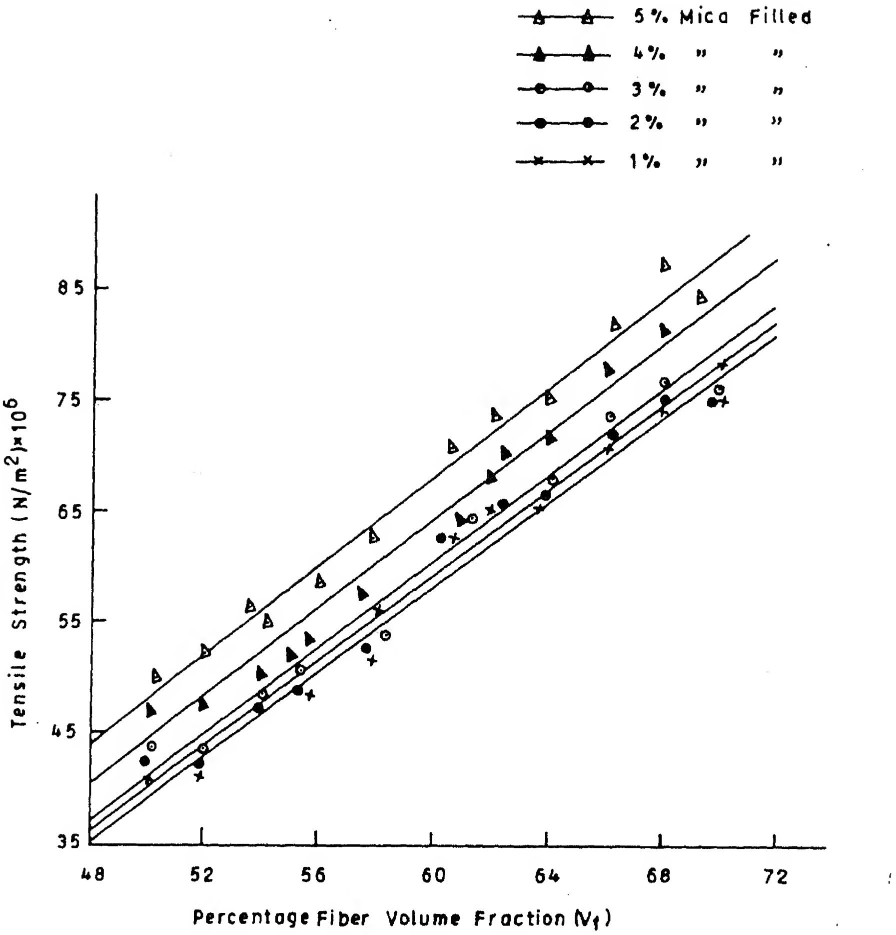

Figure 6. Variation of tensile strength with percentage V_f of mica filled GRP composite.

n energy transfer in a GRP composite specimen. in turn would provide information about the quality ie material. The ultimate purpose of AU approach relate efficiency of stress wave energy propagation material.

r fibre-reinforced composite, better stress wave gy transfer means better transmission of dynamic i, better load distribution, greater strength and er fracture resistance. However, the lower values he SWF would suggest that the material has a n of higher attenuation which may be due to local tion in microstructural features, porosity, bond ty, cure state and microcrack population of the oosites.

was found in the present investigation that the SWF ery much reproducible when background noise at gain was deleted. This was achieved by fixing up eshold voltage. The factors that affect the experi-al results could be coupling, contact pressure, pulse gain, frequency and threshold. If all these are kept tant, then the SWF should reflect the variation in composition of the specimen under test.

4. Conclusions

Based on the present study the following conclusions can be drawn:

(I) The mechanical strengths i.e. tensile and flexural, were found to vary with SWF as well as with fibre volume fraction in the GRP composite with and without fillers.

(II) Fillers were found to be extremely useful in improving the strength SWF of the GRP composites.

(III) Out of the two fillers used in the present investigation graphite was found to improve the strength of unfilled GRP composites significantly.

References

Ferrigno T H 1978 *Principle of filler selection and use*, in *Handbook of fillers and reinforcement for plastic* (eds) H S Katz and J V Mikwski (New York: Van Nostrand Reinhold Co.) p. 11

Lorne W D 1992 *Diss. Abstr. Int.* **52** 8

Ramesteiner F and Theysohn R 1984 *Composites* **15** 121

Srivastava V K, Shembekar P S and Prakash R 1988 *Comp. Struct.* **10** 271

Vary A 1980 *J. Mater. Eval.* **40** 650

ull. Mater. Sci., Vol. 21, No. 1, February 1998, pp. 99–103. © Printed in India.

RAPID COMMUNICATION

lloy–oxide equilibria in the system Pt–Rh–O

K T JACOB*, SHASHANK PRIYA and YOSHIO WASEDA[†]

Department of Metallurgy, Indian Institute of Science, Bangalore 560 012, India
[†]Research Centre for Metallurgical Process Engineering, Institute for Advanced Materials Processing, Tohoku University, Sendai 980-77, Japan

MS received 12 January 1998

Abstract. The composition of Pt–Rh alloys that co-exist with Rh_2O_3 in air have been identified by experiment at 1273 K. The isothermal sections of the phase diagram for the ternary system Pt–Rh–O at 973 K and 1273 K have been computed based on experimentally determined phase relations and recent thermodynamic measurements on $Pt_{1-x}Rh_x$ alloys and Rh_2O_3. The composition dependence of the oxygen partial pressure for the oxidation of $Pt_{1-x}Rh_x$ alloys at different temperatures, and temperature for the oxidation of the alloys in air are computed. The diagrams provide quantitative information for optimization of the composition of $Pt_{1-x}Rh_x$ alloys for high temperature application in oxidizing atmospheres.

Keywords. System Pt–Rh–O; phase diagram; thermodynamic properties; Pt–Rh alloys; oxidation; stability field.

Introduction

lloys of platinum and rhodium are extensively used in ermocouples for high temperature measurement, and clean and inert heating elements in experimental high mperature furnaces. Phase diagram of the binary system, splayed in figure 1, shows continuous solid solubility tween the end members. An important limiting factor the use of Pt–Rh alloys is the temperature below hich Rh in the alloy can be oxidized to form Rh_2O_3. air, pure Rh_2O_3 is stable below 1315 K (Jacob and iram 1994). The thermodynamic stability window for –Rh alloys as function of temperature and oxygen rtial pressure has not been quantitatively evaluated rlier. Recently, the standard Gibbs energy of formation Rh_2O_3 (Jacob and Sriram 1994) and mixing properties Pt–Rh alloys (Jacob *et al* 1998) have been determined curately. Using these data, equilibrium conditions for e oxidation of Pt–Rh alloys can be computed. This mmunication presents the computed thermodynamic ability domain for Pt–Rh alloys against oxidation.

Alloy–oxide equilibrium

atinum does not form a stable oxide at high temperature. check if ternary oxides are stable in the system –Rh–O, mixtures containing Pt–Rh alloy and Rh_2O_3 ere equilibrated at 1273 K for 85 h in air. Alloys ntaining 10·2, 20·7, 30·5, 39·6, 48·8, 59·3, 69·5, 80·6 d 90·0 at.% Rh were used in the equilibration studies. The alloys were made by arc melting Pt and Rh sponge of 99·9% purity on a water-cooled copper hearth. Each alloy button was remelted four times to ensure homogeneity. Alloy powders were prepared by filing. Iron particles in the powder were removed by a strong magnet. Residual iron was removed by chemical dissolution in acid. Fine powder of Rh_2O_3 used in equilibrium studies was of purity >99·99%. Equimolar mixtures of alloy and Rh_2O_3 were pelletized using a steel die before equilibration in air. After heat treatment, the pellets were examined by X-ray diffraction analysis (XRD) and optical microscopy. In pellets containing alloys with 10·2 and 20·7 at.% Rh, the oxide phase (Rh_2O_3) was found to decompose. No change was detected in the phase composition of the other pellets. There was no evidence of formation of ternary condensed phases in the system Pt–Rh–O.

uthor for correspondence

3. Thermodynamic data

3.1 *Pt–Rh alloys*

The relative excess chemical potential ($\Delta\mu^E_{Rh}$) or excess partial molar free energy of mixing (ΔG^E_{Rh}) of Rh in Pt–Rh alloys has been determined recently using an emf technique (Jacob *et al* 1998). The results at 1273 K can be expressed by the relation (Jacob *et al* 1998):

$$\Delta\mu^E_{Rh} = \Delta G^E_{Rh} = RT\ \ln\gamma_{Rh} = (1 - X_{Rh})^2\,[-6{,}130 + 50\,X_{Rh}]\ \text{J/mol.} \quad (1)$$

From the Gibbs–Duhem equation, the relative excess

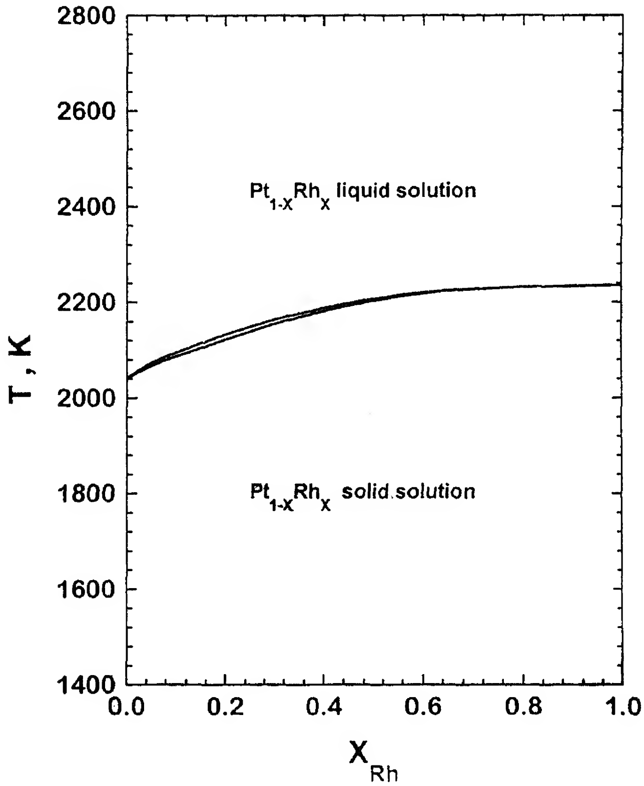

Figure 1. Phase diagram for the system Pt–Rh (Jacob *et al* 1998).

chemical potential of Pt ($\Delta\mu^E_{Pt}$) and integral excess free energy of mixing of solid Pt–Rh alloys (ΔG^E) at 1273 K were derived:

$$\Delta\mu^E_{Pt} = \Delta G^E_{Pt} = RT \ln \gamma_{Pt} = X^2_{Rh}\,[-6{,}155 + 50\,X_{Rh}] \quad \text{J/mol}, \tag{2}$$

$$\Delta G^E = X_{Rh}\,(1 - X_{Rh})\,[-6{,}130 + 25\,X_{Rh}] \quad \text{J/mol}. \tag{3}$$

The compositional dependence of excess partial entropy of mixing of Rh(ΔS^E_{Rh}) was evaluated from the variation of emf with temperature (Jacob *et al* 1998):

$$\Delta S^E_{Rh} = (1 - X_{Rh})^2\,[-3\cdot80 + 0\cdot031\,X_{Rh}] \quad \text{J/mol·K}. \tag{4}$$

By combining the partial excess free energy at 1273 K with partial excess entropy, the partial enthalpy of mixing of Rh was obtained:

$$\Delta H_{Rh} = \Delta G^E_{Rh} + 1273 \cdot \Delta S^E_{Rh}$$
$$= (1 - X_{Rh})^2\,[-10{,}970 + 90\,X_{Rh}] \quad \text{J/mol}. \tag{5}$$

From the Gibbs–Duhem equation, partial excess properties of Pt and integral excess mixing properties were obtained:

$$\Delta S^E_{Pt} = X^2_{Rh}\,[-3\cdot8155 + 0\cdot031\,X_{Rh}] \quad \text{J/mol·K}, \tag{6}$$

$$\Delta S^E = X_{Rh}(1 - X_{Rh})\,[-3\cdot80 + 1\cdot55 \times 10^{-2}\,X_{Rh}] \quad \text{J/mol·K}, \tag{7}$$

$$\Delta H_{Pt} = X^2_{Rh}\,[-11{,}015 + 90\,X_{Rh}] \quad \text{J/mol}, \tag{8}$$

$$\Delta H = X_{Rh}\,(1 - X_{Rh})\,[-10{,}970 + 45\,X_{Rh}] \quad \text{J/mol}. \tag{9}$$

Activities of component elements exhibit negative deviation from Raoult's law. Recent thermodynamic measurements (Jacob *et al* 1998) disprove the existence of solid state immiscibility below ~ 1033 K shown in current phase diagram compilations (Moffatt 1976; Massalski *et al* 1990).

3.2 Rh_2O_3

The standard Gibbs free energy of formation of $Rh_2O_3(\Delta G^\circ_f)$ with orthorhombic structure has been measured recently using an advanced design of the solid state cell with three electrodes (Jacob and Sriram 1994). This arrangement minimizes polarization of the electrodes and gives more accurate values. The data in temperature range 850–1300 K can be represented by the relation:

$$\Delta G^\circ_f(Rh_2O_3) = -3{,}96{,}365 + 282\cdot0\,T\,(\pm 120) \quad \text{J/mol}. \tag{10}$$

4. Oxygen potentials for alloy–oxide equilibria

The oxygen chemical potential corresponding to the equilibrium between the alloy and Rh_2O_3 can be computed as a function of composition of the alloy at different temperatures using the thermodynamic data. At a temperature T,

$$\Delta G^\circ_f(Rh_2O_3) = -RT \ln K = -RT \ln \frac{1}{a^2_{Rh} \cdot P^{3/2}_{O_2}}$$

$$RT \ln P_{O_2} = \Delta\mu_{O_2}(Pt_{1-X}Rh_X + Rh_2O_3)$$
$$= \tfrac{2}{3}\,\Delta G^\circ_f(Rh_2O_3) - \tfrac{4}{3}\,(RT \ln a_{Rh})$$
$$= \tfrac{2}{3}\,\Delta G^\circ_f(Rh_2O_3) - \tfrac{4}{3}\,[\Delta H_{Rh} + RT \ln X_{Rh} - T\Delta S^E_{Rh}], \tag{11}$$

where $\Delta\mu_{O_2}$ is the oxygen chemical potential, $\Delta G^\circ_f(Rh_2O_3)$ the standard Gibbs free energy of formation of Rh_2O_3, P_{O_2} the oxygen partial pressure, a_{Rh} the activity of Rh, X_{Rh} the mole fraction of Rh in the alloy, and the other symbols have their usual meaning. The computed oxygen potentials are displayed in figure 2 as a function of

mposition at different temperatures. Conditions for idation of Pt–Rh alloys at equilibrium can be readily aluated from the diagram. At oxygen partial pressures ove the curve the alloy will not oxidize. Rapid oxidation ıy result in depletion of Rh from the alloy surface, ıs increasing the oxygen potential for further oxidation the alloy.

Often Pt–Rh alloys are used in air and it is useful to ow the temperature below which oxidation is feasible m a thermodynamic point of view for a given alloy mposition. The temperature for oxidation in air can computed from thermodynamic data for alloys and $_2O_3$. Setting $(P_{O_2}/P^\circ)=0{\cdot}21$ in (11) and rearranging:

$$T=\frac{\left(\frac{2}{3}\Delta H_f^\circ(Rh_2O_3)-\frac{4}{3}\Delta H_{Rh}\right)}{\left(\frac{2}{3}\Delta S_f^\circ(Rh_2O_3)-\frac{4}{3}\Delta S^E_{Rh}+\frac{4}{3}R\ \ln X_{Rh}+R\ \ln 0{\cdot}21\right)},\tag{12}$$

ere P° is the standard atmospheric pressure 01×10^5 Pa). The computed curve is shown in figure With increase in the concentration of Rh in the alloy, the temperature for the decomposition of Rh_2O_3 in air increases rapidly at low concentrations and more gradually at higher concentrations. The safe region for the use of Pt–Rh alloys lies above the computed curve. Oxidation will not occur in this domain. Oxidation of alloys containing less than 15 at.% Rh is limited by kinetic factors at temperatures below the curve. Oxidation will become significant with increasing concentration of Rh in the alloy, especially at $T>1200$ K.

5. Ternary phase diagram of the system Pt–Rh–O

Since the oxides of platinum are unstable in the experimental temperature range and ternary oxides do not exist in the system Pt–Rh–O, isothermal sections of the phase diagram for the ternary system Pt–Rh–O at high temperatures can be constructed from the thermodynamic data using a free energy minimization algorithm (Morris and Stephenson 1986). The computed isothermal sections at 973 and 1273 K are displayed in figures 4 and 5, respectively. Phase diagrams at other temperatures can be readily calculated from the thermodynamic data. All

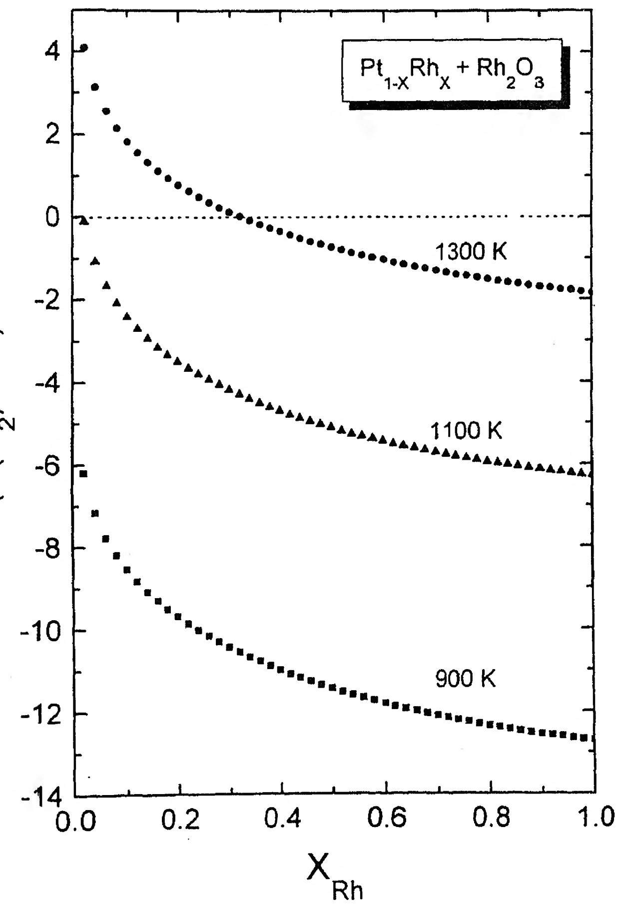

ıre 2. Variation of the equilibrium oxygen chemical ential for the formation of Rh_2O_3 as a function of composition Pt–Rh alloys at different temperatures.

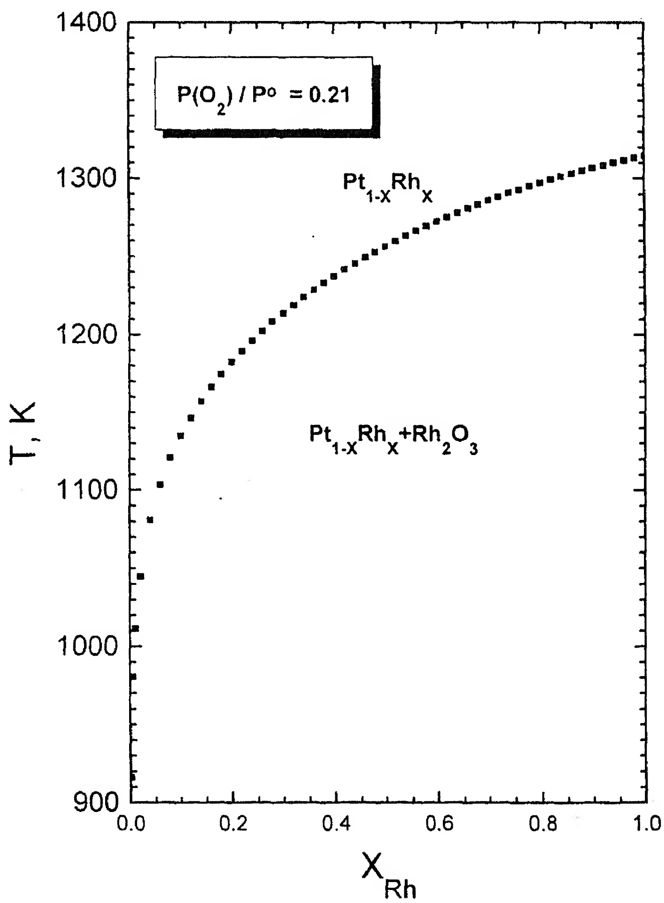

Figure 3. Variation of the equilibrium temperature for the oxidation of Pt–Rh alloys in air ($P_{O_2}=2{\cdot}12\times10^4$ Pa).

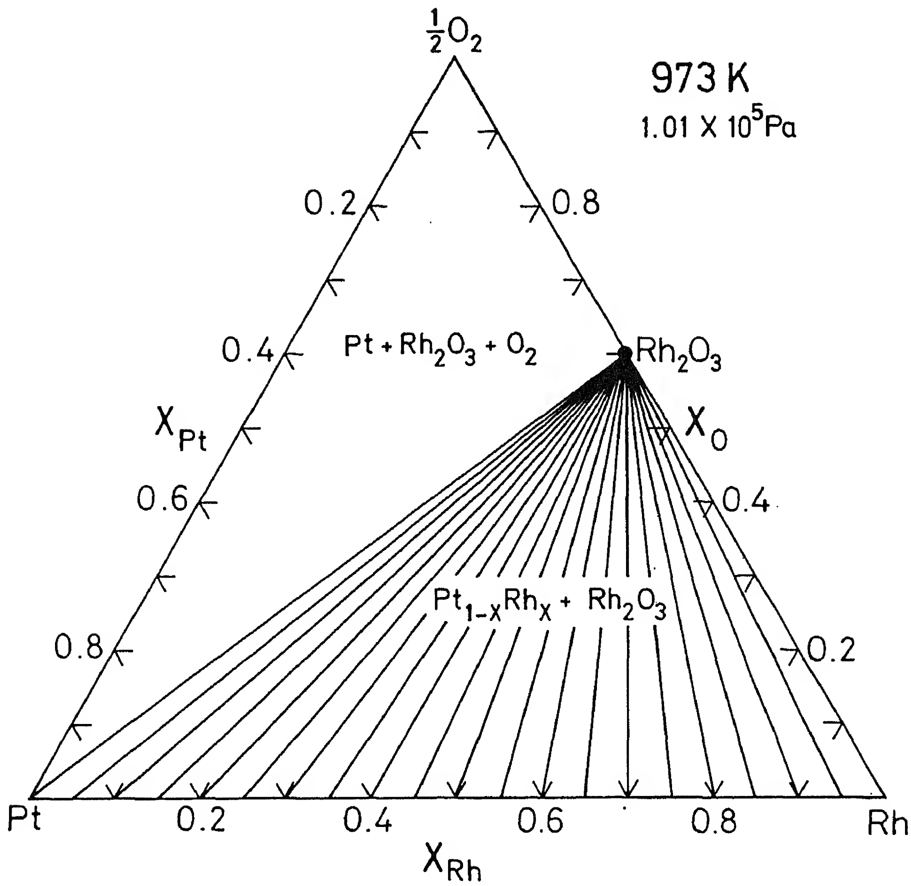

Figure 4. Isothermal section of the Pt–Rh–O system at 973 K computed from thermodynamic data.

Table 1. Temperature above which commercial $Pt_{1-x}Rh_x$ alloys will not be oxidized in air.

X_{Rh}	T, K
0·06	1104
0·13	1153
0·30	1214
0·40	1237
0·60	1272

the alloy compositions are in equilibrium with Rh_2O_3 at the lower temperature (973 K). There is a three-phase equilibrium involving Pt, Rh_2O_3 and O_2 gas at $P_{O_2} = 1{\cdot}01 \times 10^5$ Pa. At the higher temperature (1273 K), an alloy containing 24 mol% Rh is in equilibrium with Rh_2O_3 and O_2. The computed diagram is in agreement with phase equilibrium data obtained in the study, after correcting for the difference in the partial pressure of oxygen. Pt-rich alloys coexist with O_2 gas at $1{\cdot}01 \times 10^5$ Pa at 1273 K. The alloy composition corresponding to three-phase equilibrium between the alloy, Rh_2O_3 and O_2 shifts to higher concentration of Rh with increasing temperature. Use of Rh-rich alloys should be limited to temperatures above the oxidation limit. Although at low temperatures where oxidation is limited by kinetic factors, alloys can degrade at moderately elevated temperatures where oxidation is thermodynamically feasible and kinetics are favourable. The computed results provide valuable information for the intelligent use of Pt–Rh alloys in various high temperature environments containing oxygen. The lower thermodynamic limits for safe use of common alloy compositions in air are listed in table 1.

6. Optimization of alloy composition

Pt–Rh alloys are used as heating elements for furnaces that operate at temperatures higher than can be reached with pure Pt. An alloy containing ~ 80 at.% Rh is the most suitable from the point of view of melting and recrystallization temperature. However, this composition is relatively more expensive and difficult to work mechanically. Significant improvement in melting and recrystallization temperatures can be achieved by alloying up to 40 at.% Rh. Wires of $Pt_{0.6}Rh_{0.4}$ alloy are more easy to fabricate. This composition is also characterized

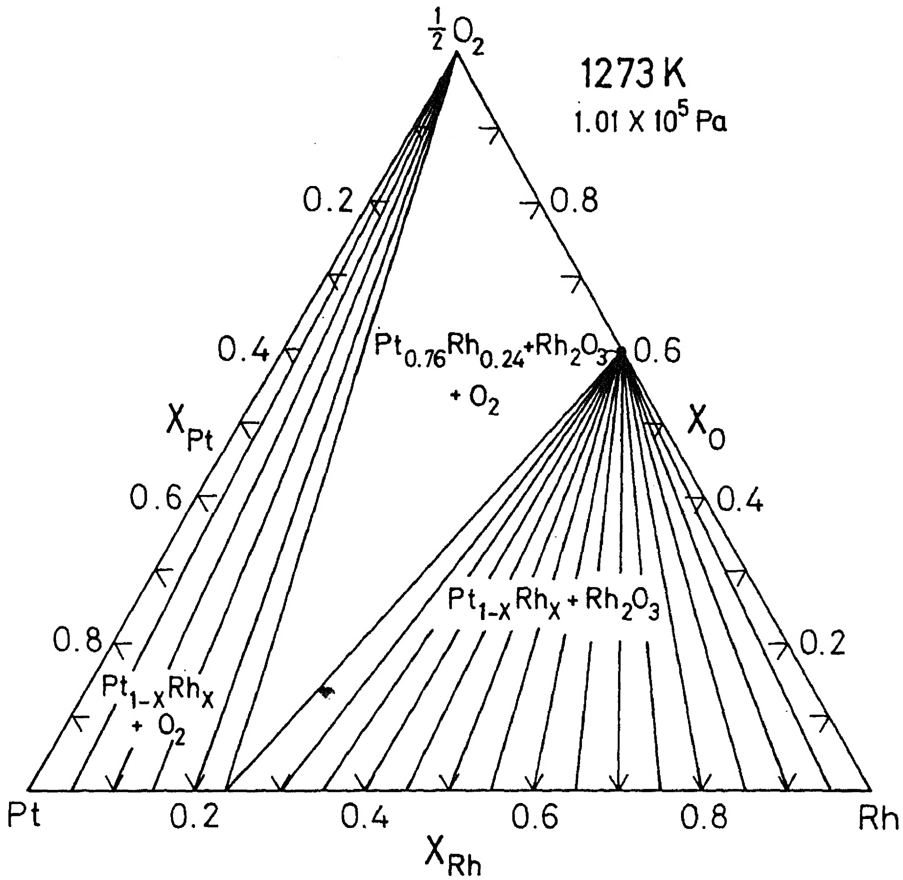

Figure 5. Isothermal section of the Pt–Rh–O system at 1273 K computed from thermodynamic data.

high value for electrical resistivity and a relatively value for temperature-coefficient of resistance en 1934). However, prolonged use in air at > T/K > 1000 is not recommended because of its nsity for oxidation. At temperatures below 1000 K, lloys may remain untarnished for significant periods ise of kinetic factors.

Conclusion

hermodynamic stability domain of Pt–Rh alloys at temperatures and in atmospheres containing oxygen een computed using recent thermodynamic data on s and oxides (Jacob and Sriram 1994; Jacob *et al* . The diagrams provide a quantitative guide for se of Pt–Rh thermocouples and heating elements in oxidizing atmospheres. The prolonged use of Pt–40% Rh alloys in air is not recommended below 1237 K.

References

Jacob K T and Sriram M V 1994 *Metall. Mater. Trans.* **A25** 1247

Jacob K T, Priya S and Waseda Y 1998 *Metall. Mater. Trans.* **A29** (in press)

Massalski T B, Subramanian P R, Okamoto H and Kaeprzak L (eds) 1990 *Binary alloy phase diagrams* (Materials Park, OH, USA: ASM International) Vol. 3

Moffatt W G 1976 and updates *Handbook of binary phase diagrams* (New York: General Electric Co.)

Morris A E and Stephenson J 1986 *J. Metals* **38** 41

Acken J S 1934 *J. Res. Bur. Stand.* **12** 249

Bull. Mater. Sci., Vol. 21, No. 1, February 1998, p. 105. © Printed in India.

BOOK REVIEW

The Metals Data Book by Alok Nayar, Tata McGraw Hill Pub. Co. Ltd., New Delhi 110 008, pp. 876 and Price: Rs 650.

The Metals Data Book contains extensive information on aspects such as classification of alloys, their composition, mechanical properties, transformation temperatures, heat treatment temperatures and typical applications of several grades of alloys including cast irons, steels, aluminium alloys, copper alloys and zinc alloys. Also provided is information on the physical properties of metals. The effect of each alloying element is described for many alloys. A chapter is exclusively devoted to powder metallurgy of some commercial alloys. This is indeed a one-stop source for all metallurgical data which are expressed in SI units. The data are compiled in the form of tables which makes reference and comparison of different alloys easy. The compilation provides Indian, American, German, British, Japanese and ISO equivalents. The book also devotes a full chapter to Units and Measures wherein conversion factors and conversion tables are included which will be of immense help.

The author, a metallurgical engineer himself with vast experience, has painstakingly put together information from available standards, reference books and publications of technical societies. The book is really the result of a commendable effort. The author may consider extending the coverage to nickel alloys, titanium alloys, molybdenum alloys and tungsten alloys in the next edition to further enhance its usefulness.

This excellent handbook is extremely useful for engineering professionals like designers, manufacturing engineers, maintenance engineers, quality assurance engineers, purchase department staff as well as teachers and researchers in the area of metals and alloys. With 876 pages and priced modestly at Rs 650, this reference book should find a place in all technical libraries.

D H Sastry
Indian Institute of Science
Bangalore 560 012, India

Bulletin of Materials Science

Notes on the preparation of papers

ıors may communicate their research work as papers and ɪ communications to the Bulletin of Materials Science. They also submit topical reviews. The papers may be sent to Editor or to one of the International Advisory Board ıbers.

ll communications should be submitted in triplicate (origi- - two copies).

ıthors are encouraged to send electronic files prepared g plain latex or MS Word (RTF), of final accepted ion of their articles. This will help hasten the process ypesetting. Line drawings also may be submitted in ronic format in some standard graphic format—TIFF, example, and saved in EPS format. However, a hard with figures must also be submitted along with floppy ') of electronic files.

bmission of a script will be held to imply that it has not previously published and is not under consideration for ication elsewhere; and further that, if accepted, it will not ublished elsewhere.

ɪscript

rs must be typed double spaced with ample margin on all on one side of white bond paper of quarto size ×215 mm). This also applies to the abstract, tables, figure ons and the list of references which are to be typed on ate sheets.

page

ıe title of the paper must be brief but informative. Serial les are to be avoided.

ıe names with initials of authors and the name and address the institution where the work was done must be given.

ɪ abbreviated running title of not more than 50 letters and aces must also be given.

ıthors are requested to provide e-mail and fax addresses hile submitting the script.

ract

rs must have a brief abstract of the significant results ted in the paper.

vords

een 3 and 6 keywords must be provided for indexing and mation retrieval.

Text

paper must be divided into sections starting preferably 'Introduction' and ending with 'Conclusions'. The main ons should be numbered 1,2 etc., the sub-sections 1.1, 1.2, and further sub-sections (if necessary) 1.1a, 1.1b, etc.

Tables

All tables must be numbered consecutively in arabic numerals in the order of occurrence in the text; they should be self-contained and have a descriptive title.

Figures

All figures including photographs should be numbered consecutively in arabic numerals in the order of appearance in the text. Line drawings must be in Indian ink on good quality tracing paper or Bristol board of the same size as the text paper. Lines should be sufficiently thick (axes about 0.3 mm, curves about 0.6 mm).

Units

Units and associated symbols must invariably follow SI practice.

References

References should be cited in the text by author and year, not by number. If there are more than two authors, reference should be to the first author followed by et al in the text. References at the end of the paper should be listed alphabetically by author's names, followed by initials, year of publication, name of the journal (abbreviated according to the World List of Scientific Periodicals, Butterworths, London), volume number, and number of the first page. Reference to books should include: name(s) of author(s), initials, year of publication, title of the book, edition if not the first, initials and name(s) of editor(s) if any, preceded by ed(s), place of publication, publisher and chapter or pages referred to. References to thesis must include the year, the title of the thesis, the degree for which submitted and the University.

Footnotes

Footnotes must be avoided if possible but when necessary should be numbered consecutively, and typed on a separate sheet.

Proofs

Authors are requested to prepare the manuscript carefully before submitting it for publication to minimize corrections and alterations in the proof which increase publication costs. Page-proofs sent to author together with the reprint order form must be returned to the editorial office within two days of their receipt by SPEED POST/COURIER.

Reprints

50 reprints of each article will be supplied free of charge.